

Molecular Dynamics Simulations of Polyelectrolyte Brushes

Dissertation

zur Erlangung des akademischen Grades
Doktor der Naturwissenschaften (Dr. rer. nat.)
in der Wissenschaftsdisziplin Theoretische Physik

eingereicht an der
Mathematisch-Naturwissenschaftlichen Fakultät der Universität Potsdam

angefertigt am
Max-Planck-Institut für Kolloid- und Grenzflächenforschung in Golm

von

Arun Kumar N.

geboren am 7. Juni 1979 in Kottayam, Indien

Potsdam, im Januar 2006

Abstract

This thesis studies strong, completely charged polyelectrolyte brushes. Extensive molecular dynamics simulations are performed on different polyelectrolyte brush systems using local compute servers and massively parallel supercomputers. The full Coulomb interaction of charged monomers, counterions, and salt ions is treated explicitly. The polymer chains are anchored by one of their ends to a uncharged planar surface. The chains are treated under good solvent conditions. Monovalent salt ions (1:1 type) are modelled same as counterions. The studies concentrate on three different brush systems at constant temperature and moderate Coulomb interaction strength (Bjerrum length equal to bond length):

The first system consists of a single polyelectrolyte brush anchored with varying grafting density to a plane. Results show that chains are extended up to about 2/3 of their contour length. The brush thickness slightly grows with increasing anchoring density. This slight dependence of the brush height on grafting density is in contrast to the well known scaling result for the osmotic brush regime. That is why the result obtained by simulations has stimulated further development of theory as well as new experimental investigations on polyelectrolyte brushes. This observation can be understood on a semi-quantitative level using a simple scaling model that incorporates excluded volume effects in a free-volume formulation where an effective cross section is assigned to the polymer chain from where counterions are excluded. The resulting regime is called nonlinear osmotic brush regime. Recently this regime was also obtained in experiments.

The second system studied consists of polyelectrolyte brushes with added salt in the nonlinear osmotic regime. Varying salt is an important parameter to tune the structure and properties of polyelectrolytes. Further motivation is due to a theoretical scaling prediction by Pincus for the salt dependence of brush thickness. In the high salt limit (salt concentration much larger than counterion concentration) the brush height is predicted to decrease with increasing external salt, but with a relatively weak power law showing an exponent $-1/3$. There is some experimental and theoretical work that confirms this prediction, but there are other results that are in contradiction. In such a situation simulations are performed to validate the theoretical prediction. The simulation result shows that brush thickness decreases with added salt, and indeed is in quite good agreement with the scaling prediction by Pincus.

The relation between buffer concentration and the effective ion strength inside the brush at varying salt concentration is of interest both from theoretical as well as experimental point of view. The simulation result shows that mobile ions (counterions as well as salt) distribute nonhomogeneously inside and outside of the brush. To explain the relation between the internal ion concentration with the buffer concentration a Donnan equilibrium approach is employed. Modifying the Donnan approach by taking into account the self-volume of polyelectrolyte chains as indicated above, the simulation result can be explained using the same effective cross section for the polymer chains. The extended Donnan equilibrium relation represents a interesting theoretical prediction that should be checked by experimental data.

The third system consist of two interacting polyelectrolyte brushes that are grafted to two parallel surfaces. The interactions between brushes are important, for instance, in stabilization of dispersions against flocculation. In the simulations pressure is evaluated as a function of separation D between the two grafting planes. The pressure behavior shows different regimes for decreasing separation. This behavior is in qualitative agreement with experimental data. At relatively weak compression the pressure behavior obtained in the simulation agrees with a $1/D$ power law predicted by scaling theory. Beyond that the present study could supply new insight for understanding the interaction between polyelectrolyte brushes.

Contents

1	Introduction	1
2	Theory	5
2.1	Free polymer chains in solution	5
2.1.1	Neutral polymer chains	5
2.1.1.1	Ideal flexible chains	5
2.1.1.2	Semiflexible chains	12
2.1.1.3	Excluded volume and solvent quality	12
2.1.2	Polyelectrolytes	16
2.1.2.1	Electrostatic interaction	16
2.1.2.2	Conformation of PEL chains	19
2.2	Tethered chains	21
2.2.1	Uncharged polymer brushes	25
2.2.1.1	Scaling behavior of polymer brushes	26
2.2.1.2	Interacting polymer brushes	27
2.2.2	Polyelectrolyte brushes	28
2.2.2.1	Scaling behavior of PEL brushes	29
2.2.2.2	PEL brushes with added salt	34
2.2.2.3	Donnan equilibrium for PEL brushes	35
2.2.2.4	Interacting PEL brushes	37
3	Simulation model and method	39
3.1	Simulation model	40
3.2	Simulation method	43
3.2.1	Parameters and integration scheme	43
3.2.2	Coulomb forces in 2D+1 slab geometry	47
3.2.3	Equilibration and error estimates	50
3.2.4	Parallel computing	53
4	Behavior of PEL brushes in the nonlinear osmotic regime	55
4.1	Height of the brush	55
4.2	Chain Structure	64
4.3	Local net charge and counterion distribution	66

5	PEL brushes with added salt	69
5.1	Height of the brush	70
5.2	Chain Structure	77
5.3	Local net charge and ion distribution close to PEL chains	79
5.4	Transverse ion distribution and Donnan equilibrium	82
6	Interactions between two PEL brushes	87
6.1	Profile and interpenetration of two interacting brushes	87
6.2	Chain Structure	95
6.3	Local net charge and ion distribution close to PEL chains	97
6.4	Pressure of two interacting brush systems	98
7	Conclusions	103
A	The MMM2D method	107
	List of symbols	113
	Bibliography	117
	Acknowledgments	125

Chapter 1

Introduction

Polymers are substances typically of high molar mass consisting of many small repeating subunits (called monomers), thus they are known as macromolecules. For example, polyethylene ($CH_3-(CH_2)_N-CH_3$) is a long chain molecule composed of ethylene molecules ($CH_2 = CH_2$), and DNA is an extremely long molecule made of up to about 10^7 nucleotides. Polyelectrolytes (PELs) are polymers that contain subunits having the ability to dissociate charges (forming charged chains and counterions) in polar solvents such as, e.g., water. This particular feature makes them environmentally friendly and of high practical relevance, e.g., PELs have completely replaced the harmful phosphates in detergents. Also biopolymers like proteins and DNA are PELs. Because of their importance in materials science, soft matter research, and molecular biology, PELs have received considerable interest in recent years [1].

A natural extension to PELs in solution is to anchor them by one of their end segments to an interface. Such systems found a lot of applications, e.g., end grafted PELs can help stabilizing colloid particles in solution against flocculation [52]. If the anchoring density is sufficiently high the chains are enforced to extend away from the anchoring surface forming a so-called brush. A schematic representation of a uncharged (or neutral) brush as well as a PEL brush is shown in Figure 1.1(a) and (b), respectively. The physics of chain extension can be different for these two systems. Modern scaling concepts introduced by de Gennes [2] can help the theoretical understanding of these systems. For a neutral brush, the equilibrium brush height results from a balance between the excluded-volume repulsion tending to swell the chains against Gaussian polymer elasticity which reduces the chain extension [8]. However, for a PEL brush in the so-called osmotic brush regime, the brush height is determined by balancing the counterion osmotic pressure which tries to swell the chains against the entropic polymer elasticity [9].

Computer simulations are an excellent tool to check theoretical predictions. For a neutral brush, simulation studies give good agreement with the scaling prediction for the brush extension [77]. However, simulations on charged systems are computationally rather expensive [141, 156] due to the long range nature of Coulomb interaction which is to be handled

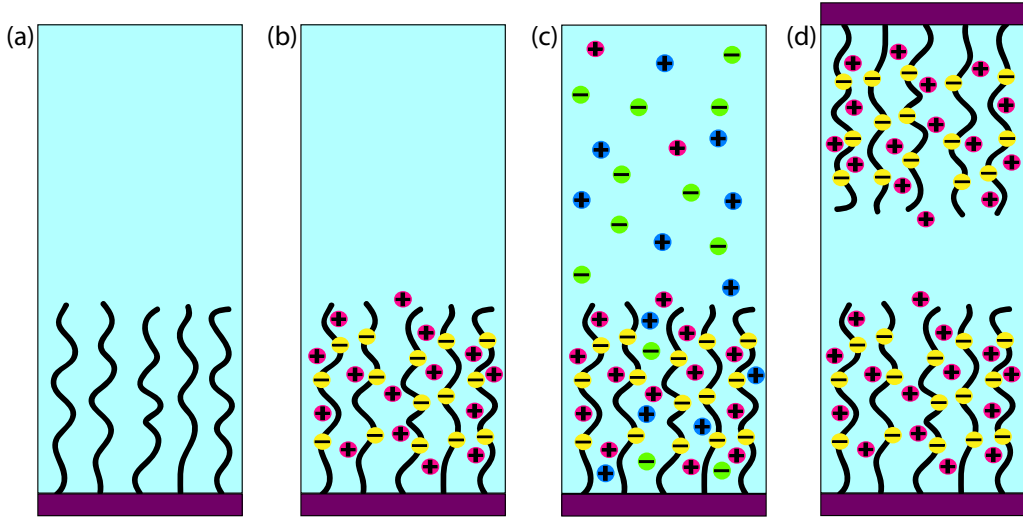


Figure 1.1: Schematic picture of polymer brushes: (a) neutral polymer brush; (b) PEL brush; (c) PEL brush with added salt; (d) two interacting PEL brushes.

by using special methods like the Ewald summation method [22]. Nevertheless, simulations can treat the direct Coulomb sum instead of using approximations as, e.g., the Debye-Hückel (DH) one, where all mobile ions (counterions as well as salt ions) are smeared out to a homogeneous background that causes a certain screening of the interaction. However, at least for strong PELs where the Coulomb energy is often larger than the thermal energy $k_B T$, the DH approximation is suspected to neglect important physical features like, e.g., counterion condensation [32, 33]. There are methods to treat the Coulomb summation in the particular geometry of a PEL brush based on Ewald summation or due to a summation technique proposed by Lekner [146] where the CPU time for evaluating the energy or all the pairwise force, respectively, grows quadratically with the total number of charges (N_{tot}) simulated. However using such $\mathcal{O}(N_{\text{tot}}^2)$ methods, within the current computational capabilities one is able to simulate only up to about 2000 charged particles [104]. For considering larger systems, one has to pass over to improved methods which give a better time scaling in treating long-ranged interactions. Here, a new method called MMM2D [145] is employed to calculate the Coulomb sums in the particular brush geometry and now we are able to simulate up to about 10000 particles. This makes it possible to study, e.g., additional salt (more charged particles) in the PEL brush system. We use a simulation technique which allows the investigation of an off-lattice coarse-grained model of polyelectrolyte chains. Extensive constant temperature molecular dynamics simulations on PEL brush systems have been performed using local compute servers as well as massively parallel supercomputers. We avoid any mean-field treatment or truncation. Counterions are included explicitly, and we treat the full Coulomb interaction.

Simulation results on PELs brushes show that in contrast to the well-accepted scaling prediction in the so-called osmotic brush regime a slight but detectable variation of brush height on grafting density is obtained. This regime is called the nonlinear osmotic brush regime. It can be understood within a simple free-volume approximation that takes into account the finite volume of the polymer chains. Recently it was obtained also in experiments. Simulation studies with additional salt ions in PEL brush systems (see Figure 1.1(c)) are important for two reasons: First, varying salt concentration is an important parameter to tune structure and properties of PELs and second, there are specific predictions found by the scaling theory that have to be verified [9]. For an osmotic brush in the salted regime where salt concentration c_s is supposed to be much greater than counterion concentration c_{ci} a weak power law dependence of brush height on salt concentration with an exponent $-1/3$ has been predicted [9]. There is some experimental and theoretical work that confirms this prediction, but there are other results that are in contradiction. In such a situation simulations are a promising tool to validate theoretical predictions. The prediction is based on the assumption that screening from the added salt reduces the counterion osmotic pressure which stretches the chains and indeed, for the first time in simulations, we observe the Pincus prediction [9] for the scaling behavior of brush height on salt concentration.

Another system studied using simulations consists of two PEL brushes grafted on two opposing walls (see Figure 1.1(d)). Interactions between brushes are important, e.g., in preventing colloids in polar media from flocculation [52] and are of high utility in biolubrication [124]. Experiments done with surface force apparatus (SFA) enable to determine the forces the PEL brushes exert on the walls as their distance is reduced below a certain value. Scaling theory [9] suggests that in the case of interacting PEL brushes between two walls, the disjoining pressure is the osmotic pressure of counterions and therefore the pressure is expected to scale as $1/D$, where D is the distance between the two anchoring surfaces. But neither SFA experiments observe this scaling prediction [119] nor refined theories exist that would be able to explain these experimental findings, at least at higher compressions. Simulation studies give new insight into that problem showing that there are indeed different regimes in the pressure behavior. We also obtain monomer profiles and counterion distributions of the system which are not easily accessible to SFA experiments.

Chapter 2

Theory

This chapter briefly reviews a few theoretical approaches in order to understand the behavior of polymers in general and polyelectrolytes in particular with the main attention focussed on the scaling theory for polyelectrolyte brushes.

2.1 Free polymer chains in solution

Theoretical models usually consider single chain modeling an ideal polymer with no inter-chain interactions. One among the beginners to study polymers by means of standard methods of statistical physics was Flory [11]. Followed that was a vast amount of interest in polymer physics [2, 12–16]. Due to that the statistical property of a single polymer chain in the equilibrium state is rather well understood.

2.1.1 Neutral polymer chains

2.1.1.1 Ideal flexible chains

The simplest model of an ideal polymer one can imagine is the freely jointed chain model and therefore it is often employed in the simulation model for polymer chains. This model consists of $N + 1$ dimensionless monomers represented by the set of position vectors $\{\mathbf{R}_i\} \equiv (\mathbf{R}_0, \dots, \mathbf{R}_N)$ (see Figure 2.1(a)). The bond vectors $\mathbf{r}_i = \mathbf{R}_i - \mathbf{R}_{i-1}$ connecting any two neighboring monomers along the polymer backbone is taken from the set $\{\mathbf{r}_i\} \equiv (\mathbf{r}_1, \dots, \mathbf{r}_N)$ where each bond vector is of fixed bond length b . Also, there is no correlations between the directions of different bond vectors i.e. they are able to point in any direction independently of each other.

The chain size is characterized by the end-to-end vector \mathbf{R} defined as

$$\mathbf{R} \equiv \mathbf{R}_N - \mathbf{R}_0 = \sum_{i=1}^N \mathbf{r}_i. \quad (2.1)$$

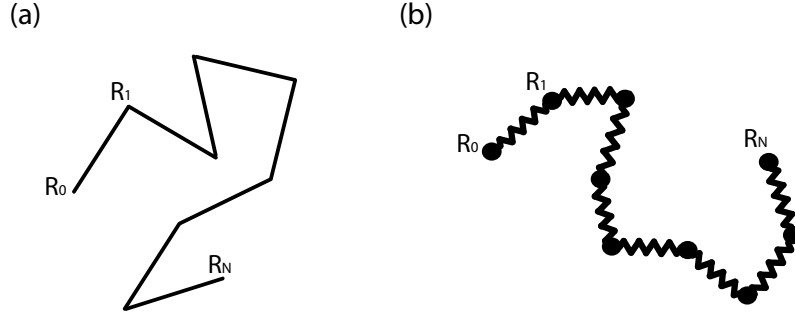


Figure 2.1: (a) Freely jointed chain model; (b) Gaussian chain model.

Since the average end-to-end vector $\langle \mathbf{R} \rangle = 0$, the simplest non-zero average¹ is the mean square end-to-end distance $\langle \mathbf{R}^2 \rangle$. Let R be defined by

$$R^2 \equiv \langle \mathbf{R}^2 \rangle. \quad (2.2)$$

Substituting for \mathbf{R} from eq. (2.1) in eq. (2.2) gives

$$R^2 = \sum_{i=1}^N \langle \mathbf{r}_i^2 \rangle + 2 \sum_{i>j} \langle \mathbf{r}_i \cdot \mathbf{r}_j \rangle = Nb^2, \quad (2.3)$$

because for $i \neq j$, $\langle \mathbf{r}_i \cdot \mathbf{r}_j \rangle = \langle \mathbf{r}_i \rangle \cdot \langle \mathbf{r}_j \rangle = 0$.

The result $R \sim N^{1/2}$ holds even for more general models (for example, the freely rotating chain model where all bond lengths and bond angles are fixed and therefore correlation between bond vectors \mathbf{r}_i and \mathbf{r}_j included in eq. (2.3) is non-zero).

In general if the distribution function of \mathbf{r}_i for the polymer conformation is written in the form

$$\Psi(\{\mathbf{r}_i\}) = \prod_i \psi(\mathbf{r}_i, \mathbf{r}_{i+1}, \dots, \mathbf{r}_{i+i_c}), \quad (2.4)$$

where $i + i_c \leq N$, R is written for large N as

$$R = b_{\text{eff}} \sqrt{N}. \quad (2.5)$$

where now b_{eff} is called the effective bond length and the ratio $C_\infty \equiv b_{\text{eff}}^2/b^2$ represents the stiffness of the polymer which can be calculated from the local structure of the chains². However,

¹ $\langle \dots \rangle$ will denote either time averages or averaging over all allowed conformations (ensemble averages). In other words, the ergodicity of the system is implicitly assumed.

²From now on, for simplicity we will write b for b_{eff} .

stiffness can also be represented by the Kuhn segment length b_K defined by

$$b_K \equiv R^2/R_{\max}, \quad (2.6)$$

where R_{\max} is the maximum length of the end-to-end vector (contour length).

The statistical distribution of the end-to-end vector for a freely jointed chain model can be calculated as follows. Since the direction for bond vectors are independent of each other, the distribution function for the polymer conformation becomes

$$\Psi(\{\mathbf{r}_i\}) = \prod_{i=1}^N \psi(\mathbf{r}_i), \quad (2.7)$$

where

$$\psi(\mathbf{r}) = \frac{\delta(|\mathbf{r}| - b)}{4\pi b^2} \quad (2.8)$$

is the random distribution on the sphere for a vector of constant length b . This distribution is normalized to

$$\int d\mathbf{r} \psi(\mathbf{r}) = 1. \quad (2.9)$$

Given the conformational distribution $\Psi(\{\mathbf{r}_i\})$, the probability distribution function that the end-to-end vector of the chain consisting of N links is \mathbf{R} is calculated by

$$\varphi(\mathbf{R}, N) = \int d\mathbf{r}_1 \int d\mathbf{r}_2 \cdots \int d\mathbf{r}_N \delta\left(\mathbf{R} - \sum_{i=1}^N \mathbf{r}_i\right) \Psi(\{\mathbf{r}_i\}). \quad (2.10)$$

Using the relation given in eq. (2.7) after some non-trivial steps, the probability distribution function $\varphi(\mathbf{R}, N)$ for a freely jointed chain reads

$$\varphi(\mathbf{R}, N) \simeq \left(\frac{3}{2\pi N b^2}\right)^{\frac{3}{2}} \exp\left(-\frac{3\mathbf{R}^2}{2N b^2}\right). \quad (2.11)$$

The distribution of the end-to-end vector \mathbf{R} is Gaussian. For $\mathbf{R}^2 \lesssim N b^2$, the corrections in eq. (2.11) are of order $1/N$ and can be neglected for $N \gg 1$. If $\mathbf{R}^2 \gg N b^2$, the corrections can be substantial. Note that for $\mathbf{R}^2 > N^2 b^2$, $\varphi(\mathbf{R}, N)$ is finite which is physically unreasonable for real chains. Nevertheless, owing to the exponential decrease, the function $\varphi(\mathbf{R}, N)$ itself is so small in this region that the deviations from the Gaussian are quite inessential for most practical problems. However, e.g., for PELs often $\mathbf{R}^2 \gg N b^2$, and hence the strong stretching limit should be considered properly (see below).

Although the above derivation is for the freely jointed chain, the result is actually valid for more general models³ like, e.g., freely rotating chain model. In general, provided the

³The term random flight is used in literature for these general models obeying eq. (2.4) because the evaluation of eq. (2.10) is formally identical to the calculation of the probability distribution of the end-to-end vector for

conformational distribution is described by eq. (2.4), the distribution of the end-to-end vector \mathbf{R} of a long chain ($N \gg 1$) is given by eq. (2.11). This is a result of the central limit theorem in statistics.

A more analytically easily tractable model is the Gaussian chain model. This model assumes a chain whose bond length is Gaussian distributed

$$\psi(\mathbf{r}) = \left(\frac{3}{2\pi b^2} \right)^{\frac{3}{2}} \exp\left(-\frac{3\mathbf{r}^2}{2b^2}\right), \quad (2.12)$$

so that

$$\langle \mathbf{r}^2 \rangle = b^2. \quad (2.13)$$

The conformational distribution function of such a chain is given by

$$\Psi(\{\mathbf{r}_i\}) = \prod_{i=1}^N \psi(\mathbf{r}_i) = \left(\frac{3}{2\pi b^2} \right)^{3N/2} \exp\left(-\sum_{i=1}^N \frac{3\mathbf{r}_i^2}{2b^2}\right). \quad (2.14)$$

This model does not describe correctly the local structure of the polymer, but does correctly describe the property on large length scales. However, the local structure of the polymer modifies only b_{eff} but does not otherwise appear in the problem.

The Gaussian chain is often represented by a mechanical model (see Fig. 2.1(b)) where $(N + 1)$ ‘beads’ are considered to be connected by harmonic springs the potential energy of which is given by

$$U(\{\mathbf{R}_i\}) = \frac{3k_{\text{B}}T}{2b^2} \sum_{i=1}^N \mathbf{r}_i^2. \quad (2.15)$$

At equilibrium, the Boltzmann distribution for such a model is exactly the same as eq. (2.14).

An important property of the Gaussian chain is that the distribution of the vector $\mathbf{R}_i - \mathbf{R}_j$ between any two units i and j is Gaussian, being given by

$$\varphi(\mathbf{R}_i - \mathbf{R}_j, i - j) = \left(\frac{3}{2\pi b^2 |i - j|} \right)^{3/2} \exp\left(-\frac{3(\mathbf{R}_i - \mathbf{R}_j)^2}{2|i - j|b^2}\right), \quad (2.16)$$

which follows from the properties of Gaussian integrals. For any i and j it holds that

$$\langle (\mathbf{R}_i - \mathbf{R}_j)^2 \rangle = |i - j| b^2. \quad (2.17)$$

The suffix i of the Gaussian chain is often regarded as a continuous variable s . In such cases

a random walk model of N steps, each of whose length is governed by the probability distribution $\psi(\mathbf{r})$. Therefore eq. (2.10) connects the study of chain statistics to that of random walks and hence to Brownian motion, diffusion, and heat transfer. Since the diffusion equation is similar to the Schrödinger equation, there exist analogies between the descriptions of polymer chains and quantum mechanical systems.

$\mathbf{r}_i = \mathbf{R}_i - \mathbf{R}_{i-1}$ is replaced by $\partial\mathbf{R}(s)/\partial s$ and eqn. 2.14 is written as

$$\Psi[\mathbf{R}(s)] = \text{const} \times \exp\left(-\frac{3}{2b^2} \int_0^N ds \left(\frac{\partial\mathbf{R}(s)}{\partial s}\right)^2\right). \quad (2.18)$$

This distribution is known as the Wiener distribution [15].

To calculate the free energy for a Gaussian chain, we write down the Boltzmann entropy

$$S(\mathbf{R}, N) \equiv k_B \ln W(\mathbf{R}, N), \quad (2.19)$$

where $W(\mathbf{R}, N)$ is the number of conformations of the Gaussian chain of N monomers with end-to-end vector \mathbf{R} which is related to the probability distribution function $\varphi(\mathbf{R}, N)$ as

$$\varphi(\mathbf{R}, N) = \frac{W(\mathbf{R}, N)}{\int W(\mathbf{R}, N) d\mathbf{R}}. \quad (2.20)$$

The Helmholtz free energy of the chain is

$$F(\mathbf{R}, N) = U(\mathbf{R}, N) - TS(\mathbf{R}, N). \quad (2.21)$$

Using eqns. 2.16, 2.19, 2.20, and the fact that for a Gaussian chain the interaction energy $U(\mathbf{R}, N)$ is independent of \mathbf{R} (see eqn. 2.15), the above free energy can be written as

$$F(\mathbf{R}, N) = \frac{3k_B T}{2Nb^2} \mathbf{R}^2 + \text{terms independent of } \mathbf{R}. \quad (2.22)$$

The entropic stretching force required to keep the chain at the end-to-end separation \mathbf{R} is calculated as

$$\mathbf{f}_{\text{st}} = -\frac{\partial F(\mathbf{R}, N)}{\partial \mathbf{R}} = -\frac{3k_B T}{Nb^2} \mathbf{R}, \quad (2.23)$$

which follows the Hooke's law with spring constant

$$k = \frac{3k_B T}{Nb^2}. \quad (2.24)$$

Since this force is of purely entropic origin the Gaussian chain is also called an entropic chain.

The free energy in eqn. 2.22 is valid for $x = R/Nb$ smaller than ≈ 0.5 . A second condition for eqn. 2.22 is $Nx^2 \gg 1$, which (for a given degree of stretching x) requires that N is sufficiently large. However, for PELs, x can be larger than 0.5, in which case for sufficiently large N , the free energy can be obtained from integration of the Langevin function

$$x = \coth(bf_{\text{st}}) - \frac{1}{bf_{\text{st}}}, \quad (2.25)$$

with f_{st} the force exerted on the chain (bf_{st} in units of $k_B T$). The above equation is expanded

as a Taylor series [12], however, due to the slow convergence this expansion is not very practical at higher relative extensions x , and always predict a finite free energy at $x = 1$ (where it should diverge). The correct limit of the free energy, eqn. 2.22, at high degrees of stretching is (in units of $k_B T$) [94]

$$F = -N(\ln(1 - x) + \text{const.}), \quad (2.26)$$

which can be derived as follows. The chain partition function reads

$$\Omega = \left[\int_0^{2\pi} \frac{d\phi}{2\pi} \int_0^\pi \frac{d\theta}{2} \sin\theta \exp(bf_{\text{st}} \cos\theta) \right]^N. \quad (2.27)$$

where the set of angles $\{\theta_i, \phi_i\}$ specify the monomer orientations in the freely jointed chain model. Integrating above eqn. 2.27

$$\Omega = \left[\frac{\exp(bf_{\text{st}}) - \exp(-bf_{\text{st}})}{2bf_{\text{st}}} \right]^N. \quad (2.28)$$

The end-to-end distance of the chain R is calculated as

$$R = \frac{\partial \ln \Omega}{\partial f_{\text{st}}} \quad (2.29)$$

which results in the above eqn. 2.25. Using Legendre transformation, the isochoric free energy of the system (in units of $k_B T$) is calculated as, $F = -\ln \Omega + Rf_{\text{st}}$, hence

$$\frac{F}{N} = -\ln \frac{\sinh(bf_{\text{st}})}{bf_{\text{st}}} + bf_{\text{st}} \coth(bf_{\text{st}}) - 1, \quad (2.30)$$

In the weak stretching or Gaussian chain limit $bf_{\text{st}} \ll 1$, a proper expansion in eqn. 2.25 leads to $x = R/Nb \simeq bf_{\text{st}}/3$ which is then substituted in eqn. 2.30 to get the relation eqn. 2.22. In the opposite limit, $bf_{\text{st}} \gg 1$ a nonlinear force extension relation is reached from eqn. 2.25, that is $x = R/Nb \simeq 1 - (1/bf_{\text{st}})$. Substituting this in eqn. 2.30 leads to eqn. 2.26 [94].

The quantity R_g is directly related to scattering experiments (see below), where the mean square radius of gyration R_g^2 is defined as

$$R_g^2 \equiv \frac{1}{N+1} \sum_{i=0}^N \langle (\mathbf{R}_i - \mathbf{R}_{\text{CM}})^2 \rangle, \quad (2.31)$$

with the position vector of the center of mass of the chain

$$\mathbf{R}_{\text{CM}} \equiv \frac{1}{N+1} \sum_{i=0}^N \mathbf{R}_i. \quad (2.32)$$

Substituting eq. (2.32) in eq. (2.31) R_g^2 can be rewritten as

$$R_g^2 = \frac{1}{2(N+1)^2} \sum_{i,j=0}^N \langle (\mathbf{R}_i - \mathbf{R}_j)^2 \rangle. \quad (2.33)$$

For a linear Gaussian chain R_g^2 is easily calculated [14]

$$R_g^2 = \frac{1}{6} N b^2. \quad (2.34)$$

Further, the overall shape of a polymer can be described by a unitless number called shape factor defined as the ratio

$$r_s = \frac{R^2}{R_g^2}. \quad (2.35)$$

r_s is 2 for a spherical globule, 6 for a Gaussian chain, and 12 for a rigid rod.

The size of polymers can be measured by various scattering experiments like, e.g., neutron scattering [17,18]. Since we model single chains, the quantity of interest is intrachain structure factor or form factor

$$S(\mathbf{q}) \equiv \frac{1}{N+1} \sum_{i,j=0}^N \langle e^{i\mathbf{q} \cdot (\mathbf{R}_i - \mathbf{R}_j)} \rangle \quad (2.36)$$

where $|\mathbf{q}| \equiv q \equiv |\mathbf{q}_f - \mathbf{q}_i|$ is the difference between the wave vectors of scattered and incident beam. At $N \gg 1$ the sums can be replaced by integrals, and, for the Gaussian chains

$$\begin{aligned} S(\mathbf{q}) &= 1 + \frac{1}{N+1} \sum_{i \neq j} \langle e^{i\mathbf{q} \cdot (\mathbf{R}_i - \mathbf{R}_j)} \rangle \\ &\simeq 1 + \frac{1}{N} \int_0^N d\tau \int_0^N d\tau' \exp\left(-\frac{b^2 q^2}{6} |\tau - \tau'|\right) \\ &\simeq 1 + ND(q^2 R_g^2), \end{aligned} \quad (2.37)$$

where $D(q^2 R_g^2)$ is the Debye function

$$D(x) \equiv \frac{2}{x^2} (e^{-x} + x - 1). \quad (2.38)$$

The asymptotic behavior of $S(\mathbf{q})$ is given by

$$S(\mathbf{q}) \simeq \begin{cases} N \left(1 - \frac{q^2 R_g^2}{3}\right) & \text{for } qR_g \ll 1 \quad (\text{Guinier region}), \\ 1 + \frac{2N}{q^2 R_g^2} & \text{for } qR_g \gg 1 \quad (\text{Porod region}). \end{cases} \quad (2.39)$$

2.1.1.2 Semiflexible chains

As already mentioned the Gaussian chain model is handicapped in detailing the local structure of the chain and therefore mostly applicable only to study flexible chains on large length scales where the local chain correlations are negligible. Therefore, sophisticated models have been exposed in literature which can more accurately describe the local structure of the chain, in particular these models offer a way for studying chain stiffness and its relation to the microscopic (chemical) parameters. The worm-like chain model [20] (sometimes called Kratky-Porod model) is a special case of the freely rotating chain model for very small values of the bond angle. This is a good model for stiff polymers, such as double-stranded DNA for which the flexibility is due to fluctuation of the contour of the chain from a straight line. The energy associated with the bending for this model is written as

$$U_{\text{bend}} = \frac{1}{2}Y \int_0^{R_{\text{max}}} ds \left(\frac{\partial \mathbf{t}(s)}{\partial s} \right)^2, \quad (2.40)$$

where Y is a constant (Young's modulus) and $\mathbf{t}(s)$ is the unit tangent vector at the position $\mathbf{R}(s)$ along the contour distance s of the chain

$$\mathbf{t}(s) = \frac{\partial \mathbf{R}(s)}{\partial s}. \quad (2.41)$$

In the limit $R_{\text{max}} \rightarrow \infty$, the orientational correlations obey an exponential decay

$$\langle \mathbf{t}(s) \cdot \mathbf{t}(s') \rangle \simeq \exp\left(-\frac{|s-s'|}{L_p}\right), \quad (2.42)$$

where L_p is the persistence length of the chain (length scale over which correlations between monomer directions are lost) which describes the chain stiffness,

$$L_p \equiv \frac{Y}{k_B T}. \quad (2.43)$$

In the limit of large length scales, where the chain contour length $R_{\text{max}} \gg L_p$, worm-like chains behave as flexible chains, however in the opposite limit the chain behavior crosses over to a rigid rod. The double-stranded DNA has a persistence length $L_p \approx 50\text{nm}$ (Kuhn length $= 2L_p \approx 100\text{nm}$) and is regarded as a semiflexible chain. Microtubules have persistence lengths typically in the μm range and therefore can be modeled as a rigid rod. However, a single-stranded DNA ($L_p \approx 3\text{nm}$) is a flexible chain.

2.1.1.3 Excluded volume and solvent quality

In the single chain models considered so far, the interaction among the polymer segments is limited to within a few neighbors along the chain. In reality, however, segments distant along

the chain do interact if they come close to each other in space. Since each chain segment possess its own finite volume, an obvious interaction is the steric effect. This is analogous to the so-called self avoiding walk (SAW) in a random walk model [2].

Earlier discussions from Kuhn and Flory followed by many sophisticated theoretical approaches pointed out that the excluded volume interaction changes the statistical property of the chain entirely. For example, $\langle \mathbf{R}^2 \rangle$ is no longer proportional to N but to a higher power of N ,

$$\langle \mathbf{R}^2 \rangle \sim N^{2\nu}. \quad (2.44)$$

According to Flory (see below), the exponent ν is about $3/5$, so that the excluded volume effect is very important for long chains.

In real polymer chains the contributions to the interaction potential $u(r)$ for bringing two monomers from ∞ to within a distance r of each other in a solvent, are quite complicated: the interaction will include steric effects, van der Waals attraction, and also may involve other specific interactions mediated by solvent molecules. A typical example of $u(r)$ is the Lennard-Jones (LJ) potential given as

$$u(r) = 4\epsilon \left[\left(\frac{\sigma}{r} \right)^{12} - \left(\frac{\sigma}{r} \right)^6 \right] \quad (2.45)$$

where σ and ϵ are the LJ length and energy, respectively. In this potential the attractive tail due to $-1/r^6$ is the van der Waals interaction potential. This attractive part can be obtained, for e.g., from the perturbation theory in quantum mechanics. However to choose the hard-core repulsive part (chosen to be $\sim 1/r^{12}$ in LJ potential) is arbitrary. Usually terms $\sim 1/r^n$, where n is a positive integer, or exponential functions are employed. Note, however, that here we assumed the interaction potential energy $u(r)$ between the two monomers to depend only on their separation r (pair potential), which is not always true. Therefore $u(r)$ has to be understood as an effective potential where, for e.g., the interactions of the monomers with the solvent molecules are implicitly involved.

The excluded volume v_2 is defined as the volume integral

$$v_2(T) \equiv \int d\mathbf{r} \left[1 - \exp \left(-\frac{u(r)}{k_B T} \right) \right]. \quad (2.46)$$

v_2 has a dimension of volume. The Boltzmann factor $\exp \left(-\frac{u(r)}{k_B T} \right)$ appears in the above equation because the relative probability of finding a second monomer at a distance r from a given monomer in a solvent at temperature T is proportional to this factor.

The excluded volume defined in eq. (2.46) can be understood as the second virial coefficient for an imperfect gas. For the LJ potential $u(r)$, therefore v_2 is given as

$$v_2(T) = A - \frac{B}{T} \quad (2.47)$$

where A and B are constants independent of temperature (these are the two parameters which appear in the famous Van der Waals equation of state for an imperfect gas). With LJ potential as $u(r)$, v_2 is positive due to hard core repulsion at low r , but changes its sign at higher distance due to an effective attraction between monomers.

For a given combination of polymer and solvent, v_2 varies with temperature. The temperature at which $v_2 = 0$ is defined as the θ or Flory temperature (for an imperfect gas, the temperature where the second virial vanishes is called Boyle temperature). Therefore, for the LJ system using eq. (2.47), $\theta = B/A$. At θ temperature the chains behave ideally, if one ignore higher order correction terms in the virial expansion of the total interaction energy ⁴. Near to θ temperature the following approximation is valid

$$v_2(T) \sim \left(\frac{T - \theta}{\theta} \right). \quad (2.48)$$

The virial expansion of the free energy with respect to the local concentration of the segments $c(\mathbf{r}) = \int_0^N di \delta(\mathbf{r} - \mathbf{R}_i)$ is given as (including many-body interaction terms)

$$\frac{F}{k_B T} = \int d\mathbf{r} \left(\frac{1}{2} v_2 c(\mathbf{r})^2 + \frac{w}{6} c(\mathbf{r})^3 + \dots \right) \simeq v_2 \frac{N^2}{R^3} + w \frac{N^3}{R^6} + \dots \quad (2.49)$$

The first term is two-body excluded volume term $v_2 c(\mathbf{r})^2$ and the three-body interactions $w c(\mathbf{r})^3$ is the next one in the virial series. Depending on which interaction terms dominate in eqn. 2.49, in general, three types of solvents can be distinguished: good, poor (also called bad), and θ , where using a simple prototype of the mean-field theory due to Flory [11] one can calculate the size of the polymer at different solvent quality.

- (i) θ solvent: $v_2 \equiv 0$, therefore the three-body interaction term in eqn. 2.49 is the leading term and for the flexible chain, the free energy is $F/k_B T \simeq R^2/Nb^2 + N^3w/R^6$, which is minimized with respect to R giving

$$R_\theta \simeq bN^{\nu_\theta} \quad (2.50)$$

with the Flory exponent for θ solvent as $\nu_\theta = 1/2$.

- (ii) Good solvent: In a good solvent, the leading term in eqn. 2.49 is due to the two-body interaction, but v_2 is positive (excluded volume repulsion) and the free energy for the entropic chain is $F/k_B T \simeq R^2/Nb^2 + N^2v_2/R^3$, which is minimized with respect to R to obtain

$$R_{\text{good}} \simeq bN^{\nu_{\text{good}}} \quad (2.51)$$

with the Flory exponent for good solvent as $\nu_{\text{good}} = 3/5$.

⁴The effect of three-body collision term is quite weak and gives only a logarithmic correction to $\langle R^2 \rangle$.

- (iii) Poor solvent: v_2 is negative now (excluded volume attraction) causing the polymer to collapse to a globule. Here the balance between attractive two-body and repulsive three-body interactions determines equilibrium. The free energy is $F/k_B T \simeq N^2 v_2 / R^3 + N^3 w / R^6$, which is minimized with respect to R giving

$$R_{\text{poor}} \simeq b N^{\nu_{\text{poor}}} \quad (2.52)$$

with the Flory exponent for poor solvent as $\nu_{\text{poor}} = 1/3$.

The prefactor in eqns. 2.50, 2.51, and 2.52 is nonuniversal, i.e., it depends on chemical details of the polymer, in particular, on the value of the excluded volume parameter v_2 and on the stiffness of the chain.

Various sophisticated theoretical approaches like perturbation calculations, uniform expansion model, mean-field theory, and renormalization group techniques were employed later to get an exact result for ν of an excluded volume chain. In particular renormalization group techniques has proved to be a very powerful tool in treating the excluded volume interactions and ν for an excluded volume chain is found to be 0.588 ± 0.001 [15]. One of the most important results first suggested by de Gennes [2] and theoretically established by renormalization group studies is the conclusion that the dependence of many physical quantities on the chain length N (as well as on several other parameters) can be represented as universal scaling laws. In general, under the transformation

$$N \longrightarrow N/\lambda, \quad b \longrightarrow b\lambda^\nu, \quad (2.53)$$

where ν is the exponent in $R \sim N^\nu$, the physical quantity A changes as

$$A \longrightarrow \lambda^x A. \quad (2.54)$$

The parameter x depends on the nature of A and can be inferred by physical argument. As an example consider the asymptotics of the structure factor for an excluded volume chain. From dimensional analysis $S(\mathbf{q}) = f(qb, N)$. Because $S(\mathbf{q})$ is proportional to the number of scattering particles N , under the transformation 2.53 it should scale as

$$f(qb\lambda^\nu, N/\lambda) = \frac{1}{\lambda} f(qb, N). \quad (2.55)$$

Since $R_g \sim N^\nu b$ and taking into account that eqn. 2.55 must hold for any λ , one obtains

$$S(\mathbf{q}) = N f(qbN^\nu) \sim N f(qR_g). \quad (2.56)$$

In the region of short wavelength ($qR_g \gg 1$), $S(\mathbf{q})$ has to be independent of N as it was in the

ideal case (see eqn. 2.39). This is only possible if

$$S(\mathbf{q}) \sim N(qN^\nu)^{-\frac{1}{\nu}} \sim q^{-\frac{1}{\nu}}. \quad (2.57)$$

Thus, the Flory exponent ν can be deduced from the structure factor of a polymer chain in the Porod region.

For a polymer solution in a good solvent, the whole concentration region can be divided into three parts: dilute, semidilute and concentrated. At low concentrations c (dilute region) polymer coils are well separated and the behavior of the chains is very similar to that of single chains. With increasing concentration coils come closer and begin to overlap in the semidilute region above $c^* \simeq N/R^3 \approx 1/(b^3 N^{4/5})$, where c^* is the order of the local concentration inside a single coil. The so-called blob representation suggested by the results of scaling arguments gives an intuitive physical picture. Inside a sphere of size ξ there are n_b segments of a given chain that do not interact with the segments of other chains. Inside a blob the chains behave like isolated chains. At very high concentrations above $c^{**} \simeq n_b/\xi^3 \simeq v_2/b^6$ (concentrated region), the monomer concentration in the solution reaches the local monomer concentration inside a blob, i.e., correlations are screened at monomer size.

2.1.2 Polyelectrolytes

2.1.2.1 Electrostatic interaction

Polyelectrolytes (PELs) are polymers containing ionizable subunits which when dissolved in a polar solvent dissociates to give charged macroions and counterions. Corresponding to the nature of the ionic subunits PELs are classified as polyanions (negatively charged subunit), and polycations (positively charged subunit). Polyampholytes have both negatively and positively charged subunits placed along the polymer chain.

A classification which is more useful for the purpose of theoretical study of PELs is with respect to their different dissociation behaviors. Strong or quenched PELs dissociate completely in the total pH range accessible to experiment. The total charge as well as its particular distribution along the chains is solely imposed by polymer synthesis. On the other hand, weak or annealed PELs dissociate in a limited pH range only. The total charge of the chain is not fixed but can be tuned by changing the solution pH. The number of charges as well as their distribution is a fluctuating thermodynamic variable. The control parameter is the solution pH which is, up to trivial additive constants, the chemical potential of the charges μ ⁵. Below we discuss the case of strong PELs. However, the specific behavior of weak PELs has attracted considerable interest in experiment [48], theory [21] and simulations [49].

Compared to their neutral counterpart, the present understanding of PELs is rather poor

⁵Strong and weak PELs, a classification used among chemists, are often referred as quenched and annealed PELs, respectively, in the physics community [21].

[1,4]. Treating counterions explicitly is analytically untractable so far. The fundamental model of a polyelectrolyte chain in solution includes a chain of N monomers with bond length b and distance between charges a (in case of annealed PELs, a is the distance between the ionizable subunits). Many analytic calculations for PELs in solution starts from the Poisson equation in electrostatics

$$\nabla^2 \phi(\mathbf{r}) = -\frac{\rho(\mathbf{r})}{\varepsilon_0 \varepsilon(\mathbf{r})}, \quad (2.58)$$

where $\phi(\mathbf{r})$ is the potential at point \mathbf{r} , $\rho(\mathbf{r})$ is the local charge density, ε_0 is the vacuum permittivity, and $\varepsilon(\mathbf{r})$ is the dielectric function of the medium. Provided that $\varepsilon(\mathbf{r}) = \varepsilon = \text{const.}$ eqn. 2.58 can be solved for various particular charge distributions which exhibits some relation to PELs. For a point charge having a charge density $\rho(\mathbf{r}) = Q_1 \delta(\mathbf{r} - \mathbf{r}_1)$, being located at $\mathbf{r} = \mathbf{r}_1$ and having a total charge $Q_1 = z_1 e$, where e is the elementary charge, the potential is given by

$$\phi(\mathbf{r}) = \frac{1}{4\pi\varepsilon_0\varepsilon} \frac{Q_1}{|\mathbf{r} - \mathbf{r}_1|}. \quad (2.59)$$

However, in a system containing M point charges, as soon as the system is finite or nonhomogeneous evaluation of the potential becomes more complex due to the existence of boundary conditions⁶. Considering the PEL to be homogeneously charged, infinitely long stiff rod (cylinder) solution to eqn. 2.58 is

$$\phi(r) = -\frac{q}{2\pi\varepsilon_0\varepsilon} \ln\left(\frac{r}{R_0}\right), \quad (2.60)$$

where distance r is measured perpendicular to the cylindrical axis, r_0 is the cylindrical radius, q is the linear charge density along the rod and R_0 is an arbitrary cut-off where $\phi(r) = 0$. Considering a system of several ionic species each of valence z_i and with local concentration c_i , the local charge density reads

$$\rho(\mathbf{r}) = e \sum_i z_i c_i(\mathbf{r}), \quad (2.61)$$

where e is the electronic charge. In mean-field description i.e. neglecting fluctuations, $c_i(\mathbf{r})$ obeys the Boltzmann distribution

$$c_i(\mathbf{r}) = c_i^{(0)} \exp\left(-\frac{z_i e \phi(\mathbf{r})}{k_B T}\right), \quad (2.62)$$

where now $\phi(\mathbf{r})$ is the time averaged value and $c_i^{(0)}$ is bulk concentration such that the requirement of electroneutrality gives $\sum_i z_i c_i^{(0)} = 0$. Using eqns. 2.61, 2.62 and 2.58, the

⁶This problem can be treated correctly using the Ewald summation techniques [22], but still make it rather computationally expensive in simulating charged systems (see section 3.2.2).

Poisson-Boltzmann (PB) equation is

$$\nabla^2 \phi(\mathbf{r}) = -\frac{e}{\varepsilon_0 \varepsilon} \sum_i z_i c_i^{(0)} \exp\left(-\frac{z_i e \phi(\mathbf{r})}{k_B T}\right). \quad (2.63)$$

Explicit general solutions of this equation are not available and hence approximations come into play. The most important contribution was made by Debye and Hückel [23] who suggested approximating the nonlinear PB equation by a linearized form. Expanding eqn. 2.63 up to the linear term in $\phi(\mathbf{r})$, the linearized PB equation reads

$$\nabla^2 \phi(\mathbf{r}) = \frac{1}{\lambda_D} \phi(\mathbf{r}), \quad (2.64)$$

where the Debye length is defined as

$$\lambda_D \equiv \kappa^{-1} = \sqrt{\frac{\varepsilon_0 \varepsilon k_B T}{e^2 \sum_i z_i^2 c_i^{(0)}}}. \quad (2.65)$$

The Debye-Hückel (DH) approximation used above is valid only at weak potentials

$$\phi(\mathbf{r}) \ll k_B T / z_i e. \quad (2.66)$$

Assuming the charge of all the other ions to be continuously smeared around a test charge, the spherically symmetric solution to eqn. 2.64 is

$$\phi_i(\mathbf{r}) = \frac{z_i e}{4\pi \varepsilon_0 \varepsilon} \frac{e^{-r/\lambda_D}}{r}, \quad (2.67)$$

and the corresponding pair interaction energy reads

$$U_{ij}(r) = z_i z_j k_B T \frac{\lambda_B}{r} e^{-r/\lambda_D}. \quad (2.68)$$

with the Bjerrum length defined as the distance at which the Coulomb interaction between two unscreened elementary charges is equal to the thermal energy

$$\lambda_B \equiv \frac{e^2}{4\pi \varepsilon_0 \varepsilon k_B T}. \quad (2.69)$$

Hence it is evident from eqn. 2.67 that the charge cloud around a test ion results in a screening of the Coulomb interaction. The Debye length λ_D gives the screening range of the resulting effective potential.

The DH assumptions are questionable for PELs due to many reasons. For a single pair interaction eqn. 2.66 is equivalent to $\lambda_B \ll r$, where r is the separation distance between the particle pair. Thus, this approximation is best valid at very dilute concentrations where the

mean particle separation is much greater than λ_B or when the Coulomb interaction energy is much less than $k_B T$. For short flexible chains, it was demonstrated by Monte Carlo (MC) simulation that the charge distribution about a chain is exceedingly different from that around a point charge [24]. On the other hand, counterion distributions about a charged cylinder obtained by MC simulation [25] agree surprisingly well with the exact solutions of the complete PB equation without added salt in the limit of point counterions [26].

Despite these serious problems, most of the theoretical studies as well as many simulations have been done within a jellium type model where all low-molecular ions (counterions as well as additional salt ions) are assumed to be homogeneously smeared throughout the solution. The resulting screened interaction can be described by a DH potential eqn. 2.68. Beside that many of theoretical works start from a rigid rod or at least from a locally rigid chain to model polyelectrolytes. Obviously the role of entropy is neglected or underestimated in such models.

2.1.2.2 Conformation of PEL chains

The Flory-like mean-field argument can be used to calculate the end-to-end distance R . Assuming all monomers are charged (monomer charge fraction $f = 1$, therefore, $a = b$), the free energy is written as

$$F/k_B T \simeq \frac{R^2}{Nb^2} + \lambda_B \frac{N^2}{R}, \quad (2.70)$$

where the first term is the elastic free energy of the Gaussian chain, eqn. 2.22, and the second term represents the electrostatic free energy of the charged monomers. Minimizing eqn. 2.70 with respect to R yields [31]

$$R \simeq \lambda_B^{1/3} b^{2/3} N. \quad (2.71)$$

The linear dependence of R on N make the PEL chain rod-like.

The deviation from completely rod-like structure is described in terms of the persistence length L_p , and the basis for many theories of PELs is the calculation of the chain persistence length. This has been done using the DH approximation, eqn. 2.68, when the chain is slightly perturbed from the rod state [27, 28]. This Odijk-Skolnick-Fixman (OSF) theory treat the polymer as a wormlike chain with a persistence length $L_p = L_i + L_e$, where L_i is the intrinsic persistence length of the uncharged polymer, and L_e is the electrostatic persistence length. Assuming a rigid rod, i.e. neglecting the entropy of the chain, asymptotically ($L_p \gg \lambda_D$),

$$L_{e, \text{OSF}} \simeq \lambda_D^2 \lambda_B / 4b^2. \quad (2.72)$$

That means L_e can be much larger than λ_D , a fact that is well known for intrinsically stiff polyelectrolytes ($L_i \gg b$) as, e.g., DNA. However, there exist different predictions on the relation between persistence length L_p and screening length λ_D [30, 31]. The above expressions can be modified to include excluded volume effects [29].

To extend beyond the OSF limit for flexible chains (where entropy cannot be neglected) Khokhlov and Khachaturian (KK) [44] consider electrostatic blobs as the monomers of a coarse-grained wormlike chain. Replacing the distance b between neighboring charges by the blob size ξ_e the electrostatic persistence length of a blob chain at θ -temperature becomes

$$L_{e, \text{KK}} \simeq \frac{\lambda_D^2}{\xi_e} = \frac{\lambda_D^2}{b} (\lambda_B/b)^{1/3}. \quad (2.73)$$

Recent theoretical [45] as well as simulation studies (see, e.g., reference [46]) strongly support the KK picture.

Another relevant theoretical work concerns the counterion distribution around the PEL chain [32–35, 42]. For a single rigid straight PEL chain (assumed to be infinitely long, and straight cylinder) with a linear charge density $\tau = f/b$ larger than a thresh hold

$$\lambda_B \tau = 1, \quad (2.74)$$

counterions condense on to the line polymer. This phenomenon called manning condensation occurs when $\lambda_B > b$ [34, 35]. This is an effect which is not captured by the linear DH theory. A simple heuristic way to incorporate the non-linear Manning condensation is to replace the bare linear charge density τ by the renormalized one $\tau_{\text{renorm}} = 1/\lambda_B$ for $\lambda_B \tau > 1$. However, this procedure is not totally satisfactory at high salt concentrations [36, 37]. Also, real polymers have a finite length, and are neither completely straight nor in the infinite dilution limit [38]. Still, Manning condensation has an experimental significance for polymer solutions [39] because thermodynamic quantities, such as counterion activities [40] and osmotic coefficients [41], show a pronounced signature of Manning condensation.

Adding salt to a dilute solution of PELs the electrostatic interaction between charged monomers become short-ranged, eqn. 2.68, with the Debye screening length for a added 1:1 salt reads

$$\lambda_D = \frac{1}{\sqrt{4\pi\lambda_B(2c_s + c_{ci})}}, \quad (2.75)$$

where c_s and c_{ci} are the salt and counterion concentrations, respectively. The so-called Debye-Hückel potential is used in many theoretical studies of PEL solutions. The introduction of such an effective pair potential requires, however, two conditions: (i) The ionic solution has to be dilute. (ii) The perturbation caused by the macroion has to be weak. For strongly charged PELs, the second condition can be rather critical and nonlinear phenomena like, e.g. counterion condensation cannot be described within this frame work, but have to be added by hand as mentioned above. At physiological conditions the salt concentration is $c_s \approx 0.1M$ and therefore $\lambda_D \approx 1\text{nm}$. Depending on the ionic strength, λ_D can vary typically from less than 1nm to more than 100nm. While at large λ_D screening can be neglected, and assuming for flexible chain the electrostatic repulsion to be the major contribution to second virial coefficient

one obtains [29]

$$v_e \simeq L_e^2 \lambda_D, \quad (2.76)$$

which is called the electrostatic excluded volume. Thus, due to the reduction of the (screened) long-range Coulomb interaction to an excluded volume interaction charged chains show the same behavior as an uncharged chain in a good solvent. The only effect is a shift of the θ -temperature due to the increased effective excluded volume. Upon further increase of salt, the electrostatic excluded volume is modified as [44]

$$v_e \simeq f^2 \lambda_B \lambda_D^2. \quad (2.77)$$

Thus, varying salt concentration is a simple tool to tune the conformation of PELs. For a simple but complete scaling picture of the dependence of PEL solutions on salt concentration see, e.g., reference [43].

2.2 Tethered chains

The study of tethered polymer chains is an area of increasing interest [5]. Tethered polymer chains refers to macromolecular chains that are attached into micro structures by their ends. Highly branched polymers, polymer micelles and end-grafted chains on surfaces are few examples (see Figure 2.2). Tethering can be reversible or irreversible and can be on various geometries (e.g. flat and curved surfaces) and is frequently sufficiently dense that the chains are crowded. All structures in Figure 2.2 have chains tethered to some grafting site. In star-branched polymers, the grafting site is the central point. In graft-polymers, it is the backbone line. End-functionalized polymers can be adsorbed or bound by those ends to a surface. In block copolymers, the tethering site is the interface between blocks of different, usually immiscible, chemical structure. The later two structures have amphiphilic character. Therefore they are able to form aggregates or microstructures such as micelles, microemulsions, and vesicles. Industrial application comes from the fact that tethered polymers can help stabilizing colloid particles in solution against flocculation [52]. For end-tethered polymer structures, the stabilization power is greatly enhanced compared to adsorbed polymer layers, where each monomer has a tendency to attract to the substrate. The main reason is that bridging of polymers between two approaching surfaces and creation of polymer loops on the same surface is very frequent in the case of polymer adsorption and eventually leads to attraction between two particle surfaces and thus destabilization. This does not happen if the polymer is grafted by one of its ends to the surface and the monomers are chosen such that they do not adsorb to the surface. Additional interest in tethered polymer chains is due to their technological applications in lubrication [53]. Experimentally two basic ways of preparing a grafted polymer layer can be distinguished (see Figure 2.3):

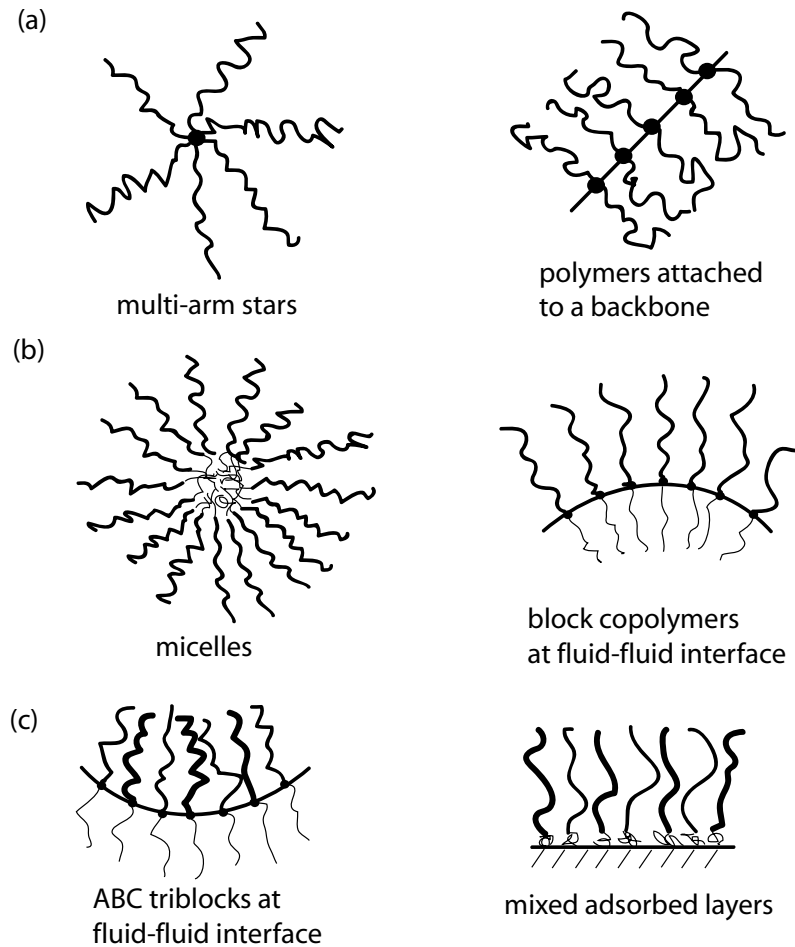


Figure 2.2: Tethered polymer chains: (a) bulk homopolymers; (b) block copolymers; (c) mixed layers.

- (i) grafting-from procedure: Polymerization is started from the surface with some suitably chosen surface-linked initiator. The reaction kinetics is comparatively fast here, because only monomers have to diffuse through the forming brush layer.
- (ii) grafting-to procedure: Here one attaches polymer with special end groups that act as anchors on the surface. Grafting-to procedure is subject to slow kinetics during the formation stage compared to grafting-from procedure since whole of the polymer molecules have to diffuse through the natant grafting layer, but benefits from a better control over the brush constitution and chemical composition.

One distinguishes physical adsorption of end-groups that favor the substrate (binding energy of order $10k_B T$), for example zwitter-ionic end-groups attached to polystyrene chains that lead to binding to mica in organic solvents such as toluene [68]. Covalently end-grafted chains

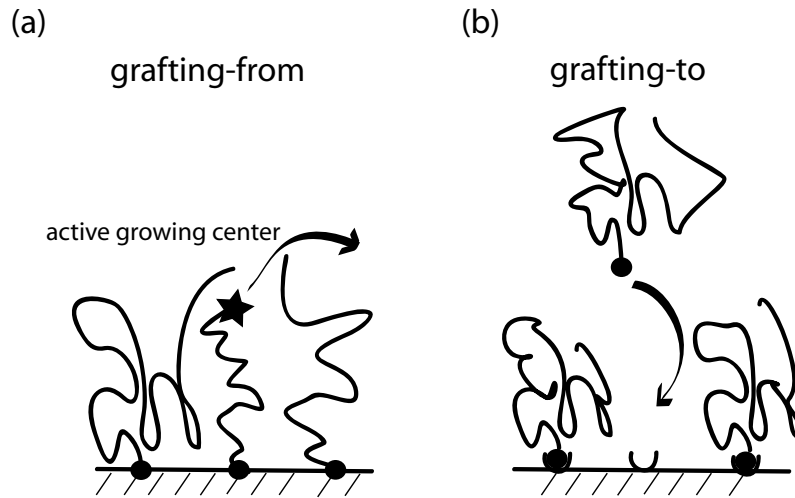


Figure 2.3: General schemes showing grafting processes leading to anchored polymer chains: (a) grafting-from process; (b) grafting-to process.

(binding energy of order several hundred $k_B T$) yield much stable and well defined system, for example, poly-dimethylsiloxane chains which carry hydroxyl end groups undergo condensation reactions with silanols of a silica surface [69]. Diblock copolymers can be employed to make tethered layers where, one block adsorbs on the surface and the other is repelled from it. An example is furnished by polystyrene-poly(vinylpyridine) (PS-PVP) diblocks in the selective solvent toluene, which is a bad solvent for the PVP block promoting its adsorption on to a quartz substrate, but acts as a good solvent for the PS block and disfavors its adsorption on the substrate [70]. This method using diblock copolymers can be extended to study systems at liquid-air or liquid-liquid interfaces. The main advantage of using diblock copolymers in such environments is that the grafting density can be varied (for densely anchored polymers) by lateral compression (like a Langmuir monolayer) and that the lateral surface pressure can be directly measured which allows comparison with theoretical predictions [71].

Depending on the grafting density ρ_a , which is the inverse of the area per end-tethered chains on a surface, two different regimes are distinguished (see Figure 2.4). In the low-density regime, $\rho_a < \rho_a^*$, the anchoring distance $\rho_a^{-1/2}$ is larger compared to the chain size so that the chains hardly interact each other at least if there are no long-ranged interactions. The polymers in this case form well separated mushrooms at the surface. The grafting density at which chains just start to overlap is determined by $\rho_a^* \sim R^{-2}$ where R is the typical radius or size of the chain. For a polymer in good solvent condition where $R \simeq bN^{3/5}$ (see eqn. 2.51), where N is the polymerization index or monomer number of the chain, and b is the monomer dimension.

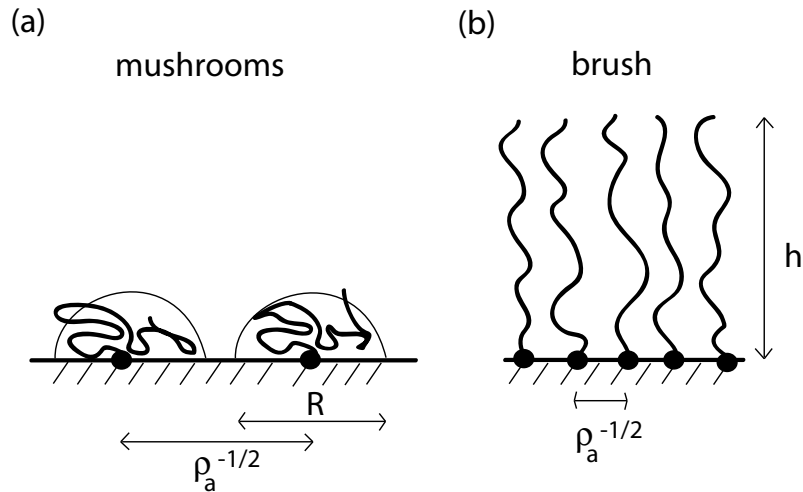


Figure 2.4: Schematic representations of grafted chains: (a) mushroom regime, where the distance between chains $\rho_a^{-1/2}$ is larger than the polymer size R ; (b) brush regime where $\rho_a^{-1/2}$ is smaller than R and chains are stretched away from the surface due to repulsive interactions between monomers.

Therefore the crossover grafting density for a polymer under good solvent condition becomes

$$\rho_a^* \sim b^{-2} N^{-6/5}. \quad (2.78)$$

For large grafting densities $\rho_a > \rho_a^*$ the chains are strongly overlapping. Since we assume the solvent to be good, monomers repel each other. The lateral separation between the polymer coils is fixed by the grafting density, so that the polymers extend away from the grafting surface in order to avoid each other. The resulting structure is called a polymer brush, with a vertical height h which can greatly exceed the unperturbed coil size R .

In the case of tethered PEL chains the polymer chains also carry ionizable groups. Tethered PEL chains share many of the features discussed above for tethered polymer chains, but qualitatively new properties emerge due to the presence of charged monomers and counterions. From the application point of view tethering PELs to colloid particles in polar media (such as aqueous solutions) prevents them from flocculating and precipitating out in solutions [52]. Further interest in these systems is due to the fact that tethered structures of PELs are found in various biological systems, e.g., the protecting envelope of cells (glycocalix).

The understanding of grafted polymer systems progressed substantially with the advent of experimental techniques such as surface forces apparatus (SFA) [82, 119], atomic force microscopy (AFM) [50], neutron reflectivity [111], infrared spectroscopy (IR) [111], X-ray reflectivity [113], small angle neutron scattering (SANS) [114], dynamic light scattering (DLS) [116, 117], ellipsometry [110], Fourier transform infrared (FTIR) [122], and isotherm [109]. In

particular, these methods are used to characterize tethered polymers and PEL chains. However, appropriate experimental methods have to be chosen, depending on the sample and, of course, on the kind of information one would like to obtain. For example, a SFA directly measures interaction forces between two surfaces (surfaces tethered with polymer chains, for instance, apposing each other), as a function of surface separation [82]. In contrast to surface force experiments [119], neutron reflectivity [111] and small angle neutron scattering [114] give informations on the inner structure of the tethered chains.

In the next sections following, we will focus mainly on densely end grafted polymer systems. However, a more detailed review on the behavior of adsorbed or tethered neutral and charged chains at interfaces can be found in reference [51], with a special attention to the case of charged polymers.

2.2.1 Uncharged polymer brushes

Polymer brushes consist of an assembly of polymer chains which are densely tethered by one end to a surface or interface [5]. Due to various forces, tethered chains are enforced to take an elongated brush like conformation (see Figure 2.4 (b)). Polymer brushes have attracted considerable attention, with many theoretical efforts in studies on the structure and phase behavior of such polymer chains in contact with a solvent [8, 54–60, 62]. They have found application in a broad range of fields, including colloid stabilization [74], tailoring surface properties and chemical gates [75]. Here we focus on polymers that are irreversibly grafted by one end to the substrate, where the substrate is assumed to be solid, planar and impenetrable to the polymer monomers. Additional effects include, e.g., polymers that have a tendency to adsorb to the substrate, brushes at curved interfaces, mixed brushes made of mutually incompatible grafted chains, grafted polymer layers in contact with a poor or θ solvent, and polymers end-grafted to fluid membranes. Most of these effects have been well studied, e.g., polymers which are attached to a fluid membrane, where essentially tensionless and very flexible surfaces are provided by membranes such as lipid bilayers in their fluid state [61]. Polymers which are attached to a fluid membrane by a single anchor exhibit a dilute mushroom regime and a semidilute brush regime, where scaling arguments and explicit calculations for ideal polymers show that the membrane is bent by the anchored polymer [62]. A rather nice discussion on additional effects considered in polymer brush systems can be found in reference [66] and the references therein.

In general, the behavior densely grafted polymer chains at a planar or curved surface is fundamentally different from that of free chains in solution. However, the theory is today quite well developed both analytically and numerically.

2.2.1.1 Scaling behavior of polymer brushes

The thickness of a neutral brush scales linearly with the chain length N , which is in obvious contrast to the well-known characteristics of free polymer chains in a good solvent, where the end-to-end distance scales as $R \simeq N^{3/5}$. For neutral brushes the simple scaling laws connecting grafting density and molecular weight with brush height were first derived by Alexander [8] and de Gennes [54, 55]. The scaling behavior can be analyzed using a Flory-like mean-field theory, which is a simplified version of the original Alexander theory [8] for polymer brushes. The main contribution to the polymer free energy comes from the elastic response due to stretching of chains, which leads to an entropic free energy⁷ loss of (see eqn. 2.22)

$$F_{\text{st}} \simeq \frac{\rho_a h^2}{Nb^2}, \quad (2.79)$$

where ρ_a is the anchoring density, h the brush height, and b being the segment length. F_{v_2} is the second virial contribution to the free energy, arising from steric repulsion between the monomers (see eqn. 2.49)

$$F_{v_2} \simeq v_2 h \left(\frac{\rho_a N}{h} \right)^2, \quad (2.80)$$

where v_2 is the second virial. The total free energy F can be now written down as the sum of the attractive (eqn. 2.79) and repulsive (eqn. 2.80) contributions to the chain conformation as

$$F = F_{\text{st}} + F_{v_2} \quad (2.81)$$

Evaluating the partial pressures given by the thermodynamic relation $\pi = -(\partial F / \partial h)_{T,N}$ the two terms in eqn. 2.81 yield

$$\pi_{\text{st}} \simeq -\frac{\rho_a h}{(Nb^2)}, \quad (2.82)$$

$$\pi_{v_2} \simeq v_2 \left(\frac{\rho_a N}{h} \right)^2. \quad (2.83)$$

Minimizing F with respect to h or balancing the corresponding partial pressures ($\pi_{\text{st}} = -\pi_{v_2}$) gives

$$h \simeq Nb(v_2 \rho_a / b)^{1/3}. \quad (2.84)$$

The linear relation between the brush height h with the polymerization index N is a clear signature of the strong stretching of the polymer chains, as was originally obtained by Alexander [8]. At the crossover grafting density, $\rho_a^* \sim b^{-2} N^{-6/5}$ (see eqn. 2.78) the height scales as $h \sim N^{3/5}$, and thus agrees with the scaling of an unperturbed chain radius in a good solvent, eqn. 2.51, as expected. The simple scaling calculation above predicts the brush height h correctly in the asymptotic limit of long chains and strong overlap. This result is consistent with

⁷From now on we write all free energy expressions per unit area and in units of thermal energy $k_B T$.

the more sophisticated scaling analysis by de Gennes viewing the brush as a stack of blobs [55]. In general, one finds that for high enough coverage that the chains overlap, h scales as

$$h \sim N(\rho_a)^{(1-\nu)/2\nu}, \quad (2.85)$$

where the exponent ν is the usual Flory exponent for the solvent quality.

This general scaling of the brush height have since largely been confirmed by more sophisticated theories [56–60], direct numerical solutions [64, 65], simulations [66, 67], and experiments [68–70, 72, 73].

The above scaling result assumes that all chains are stretched exactly to the same height, leading to a step-like shape for the density profile. However, Monte-Carlo and numerical mean field calculations exhibit a density profile which decreases monotonously to zero at the rim [64].

A better understanding of strong-stretching limit of polymer chains was made possible by Semenov [63], who recognized the importance of *classical paths* for such systems.

2.2.1.2 Interacting polymer brushes

Two polymer brushes repel each other as they are brought into contact. This repulsion, which is a result of the steric (entropic) interaction between the polymer segments, is the basis for colloid stabilization. This created an ample interest for studying these systems in detail. Experimental studies of such systems have focused on the direct measurements of the force between two surfaces onto which polymers have been terminally attached [68, 78–80, 82]. Theoretical treatments have utilized scaling arguments [8, 76] numerical self-consistent-field (SCF) calculations [64, 81], and analytical SCF equations [56] suitable for the limiting case of high molecular weight. These studies predict the equilibrium configuration of such brushes as well as the force profiles of two such brushes under compression. The forces obtained between the surfaces as a function of their separation can be described both by scaling and SCF theories and agree with the experimental force measurements [79] obtained using surface force apparatus.

However an important question not addressed by these theories and experiment is the extent of the interpenetration of the polymers from the two brushes. Both SCF and scaling theories assume that there is no interpenetration. Such questions, however, was answered by detailed molecular simulations in reference [66], where the interpenetration in the compressed brushes is described by a simple scaling form. It was found that for end-grafted polymers between parallel surfaces, the interaction is purely repulsive and it sets in as soon as the brushes touch each other before any interpenetration occurs [66].

Additional effects considered for interacting polymer brushes include, e.g., the penetration of a finite size particle into an end-grafted polymer layer [83], and applying shear forces between polymer brushes. In particular, neutral polymer brushes may lead to comparatively a massive reduction in sliding friction between the surfaces to which they are attached [84].

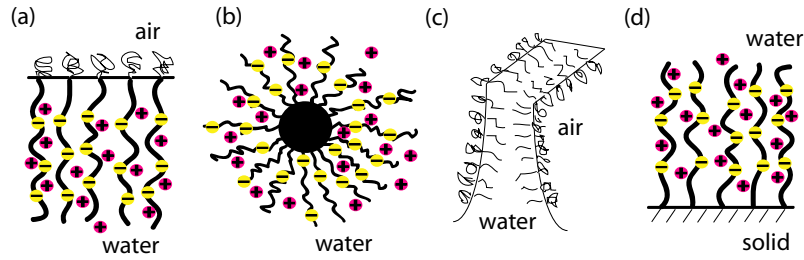


Figure 2.5: PEL brushes: (a) at air-water interface; (b) colloid particle covered by brush; (c) free-standing bilayer; (d) anchored to a solid surface.

2.2.2 Polyelectrolyte brushes

Polyelectrolyte brushes consist of charged polymers densely end-grafted to surfaces of various geometries (see Figure 2.5). PEL brushes are of two kinds. Strong or quenched PEL brushes and weak or annealed PEL brushes. Here we restrict ourselves to the case of quenched PELs end-tethered to a planar solid. However, weak polyelectrolyte brushes with an annealed charge distribution exhibit specific features [6, 7, 92]. Polyelectrolyte brushes form the subject of increasing interest by theory [9, 85–99], simulation [100–105] and experiment [10, 107–121].

Technological applications of PEL brushes includes, e.g., colloid stabilization [52], pH-controlled gating [126], and surface treatment and modification [127]. The colloid stabilization arises from steric (entropic) as well as electrostatic repulsion between the tethered chains. A strongly charged brush is able to trap its own counterions and generates a layer of locally enhanced salt concentration [9]. It is thus less sensitive to the salinity of the surrounding aqueous medium than a stabilization mechanism based on pure electrostatics (i.e. without polymers).

The general methods employed to graft polymer chains can also be employed for PEL brushes. However, in their preparation as opposite to neutral polymer chains, electrostatic

Table 2.1: A rough guide to experimental methods employed in studying properties of PEL brushes.

Properties or characteristics	Method
Chemical structure information	FTIR
Brush layer thickness	SFA, AFM, neutron scattering, neutron reflectivity, X-ray reflectivity, DLS, ellipsometry
Brush density	Neutron scattering, neutron reflectivity, X-ray reflectivity, DLS, isotherm
Surface charge interactions	SFA, AFM, isotherm

repulsions due to charges of the PEL chains are often so strong, especially in pure water, that they do not allow the chains to build a dense brush. Three major approaches are: (1) Langmuir-Blodgett method, (2) adsorption method, and (3) covalent bonding method. The Langmuir-Blodgett method uses amphiphiles bearing PELs as the hydrophilic group and prepares the brush at the air-water interface, which can be deposited on a solid substrate [109]. The second method also uses amphiphiles where the hydrophobic part can attach to a hydrophobic substrate and anchor the PEL chain [116]. The third method consists of grafting a diblock copolymer to a solid surface via a short, hydrophobic, reactive end group, which forms a covalent bond (grafting-to method). After grafting, the polyelectrolyte is formed by performing an ionization reaction on the longer block, which becomes hydrophilic [114].

Experimental methods applied to study tethered polymers can also be used for characterizing PEL brushes. Various experimental techniques employed to study the structure and properties of PEL brushes is roughly summarized in Table 2.1 together with informations the measurements provide.

2.2.2.1 Scaling behavior of PEL brushes

Theoretical work on polyelectrolyte brushes was initiated by the works of Miklavic and Marčelja [85] and Misra *et al.* [86]. Depending on grafting density ρ_a , degree of charging f and on the ionic strength of the medium quenched polyelectrolyte brushes exhibit a wide spectrum of different structures. Beginning in the last decade, the scaling behavior of strong polyelectrolyte brushes has been studied extensively from a theoretical point of view (see for a brief review, e.g., reference [19]). In 1991, Pincus [9] and Borisov *et al.* [87] presented scaling theories for charged brushes in the so-called osmotic regime, where the brush height results from the balance between the chain elasticity (which tends to decrease the brush height) and the repulsive osmotic counterion pressure (which tends to increase the brush height). In later studies, these works have been generalized to poor solvents [88, 95] and to the regime where excluded volume effects become important, the so-called quasi-neutral or Alexander regime [97], and the diagram of states of a polyelectrolyte brush was established [97].

To understand the scaling picture, assume a box model [89], where the charged brush is characterized by two length scales. The polymer chains are assumed to extend to a distance h from the grafting surface, the counterions in general form a layer with a thickness of H . Two different scenarios emerge, as is schematically presented in Figure 2.6. The counterions can either extend outside the brush, $H \gg h$, as shown in Figure 2.6(a), or be confined inside the brush, $H \approx h$ as shown in Figure 2.6(b). The case (a) is indicative of weakly charged brushes, while case (b) is typical for strongly charged brushes, both of which will be discussed below. Assuming the case of no added salt and for unit counterion valency, the contributions to the free energy are discussed below.

There are three repulsive contributions to the free energy. The osmotic free energy F_{os}

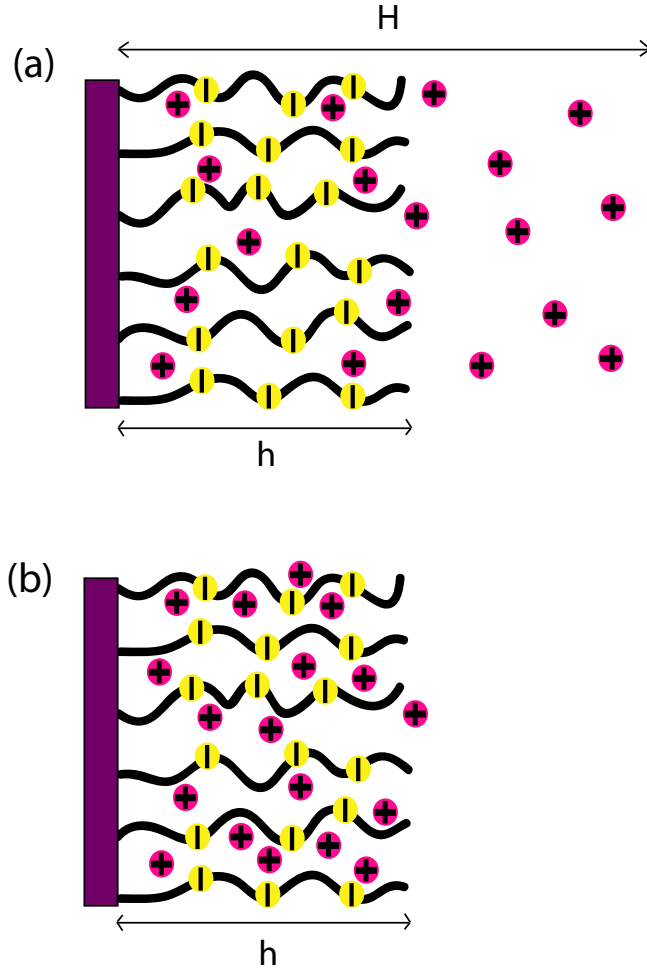


Figure 2.6: Schematic PEL brush structure: (a) weak charging limit where the counterion cloud has a thickness H larger than the thickness of the brush layer h ; (b) opposite case of strong charging limit, where all counterions are contained inside the brush and a single length scale $h \approx H$ exists.

associated with the ideal entropy cost of confining the counterions to a layer of thickness H is given by

$$F_{\text{os}} \simeq Nf\rho_a \ln \frac{Nf\rho_a}{H}. \quad (2.86)$$

F_{v_2} is the second virial contribution to the free energy, arising from steric repulsion between the monomers (contributions due to counter ions are neglected). Polymers are assumed to be in a good solvent ($v_2 > 0$). The contribution thus reads as given in eqn. 2.80.

Finally, a direct electrostatic contribution F_{el} occurs if the PE brush is not locally electro-neutral throughout the system, as for example is depicted in Figure 2.6(a). This is given

by [93]

$$F_{\text{el}} \simeq \lambda_{\text{B}}(Nf\rho_{\text{a}})^2 \frac{(h-H)^2}{H}. \quad (2.87)$$

This situation arises in the limit of low charge, when the counterion density profile extends beyond the brush layer, i.e., $H > h$.

The attractive free energy contribution is the the stretching free energy F_{st} for the polyelectrolyte chain as given in eqn. 2.79.

In strongly charged brushes with a large effective charge density of grafted PELs, i.e. for not too small grafting densities and degree of charging, effectively all the counterions are trapped inside the brush. Roughly speaking, this is the case when the Gouy-Chapman length

$$\lambda_{\text{GC}} = \frac{1}{2\pi\lambda_{\text{B}}Nf\rho_{\text{a}}}, \quad (2.88)$$

which is the height at which counterions are effectively bound to a surface of charge density $efN\rho_{\text{a}}$ [9], is small compared to the brush height h (Here $\lambda_{\text{B}} = e^2/(4\pi\epsilon_0\epsilon k_{\text{B}}T)$ is the Bjerrum length). This assumption can be explained as below. Consider the case where the counterions leave the brush, i.e., $H > h$. In this case, minimization of $F_{\text{os}} + F_{\text{el}}$ with respect to the counterion height H for an infinitely thin brush layer ($h = 0$) leads to a height

$$H \simeq 3\lambda_{\text{GC}}, \quad (2.89)$$

which scales linearly with the Gouy Chapman length, eqn. 2.88. Similarly, minimizing $F_{\text{os}} + F_{\text{el}}$ with respect to H , but now for a finite brush height h one obtains (to first order in powers of $(H - h)/h$) [10]

$$H \simeq h + 3\lambda_{\text{GC}}/2. \quad (2.90)$$

Because for a typical fully charged brush the Gouy-Chapman length λ_{GC} is of the order of 0.1 nm or less, the counterion layer basically has the same height as the brush layer. In that situation, the direct electrostatic contribution F_{el} vanishes. There are two ways of balancing the remaining free energy contributions. First, the free energy F can be written as the sum of F_{os} and F_{st} . Minimizing $F_{\text{os}} + F_{\text{st}}$ with respect to the brush height h or, equivalently, balancing the corresponding partial pressures (as discussed in the case of neutral brushes)

$$\pi_{\text{os}} \simeq \frac{Nf\rho_{\text{a}}}{h}, \quad (2.91)$$

and eqn. 2.82 one obtains in the so-called osmotic brush regime [9]

$$h \simeq Nbf^{1/2}. \quad (2.92)$$

Note that the predicted brush height is independent of the grafting density ρ_{a} . If polyelec-

trolyte brushes with very high grafting densities are considered the excluded volume interaction can no longer be neglected. If steric effects dominate over electrostatic effects the elastic pressure is again balanced by a second virial term and the behavior of the neutral brush, discussed above in eq. (2.84), is recovered. Precisely speaking, the prefactor is increased due to an electrostatic contribution to the excluded volume. In this case, however, the scaling properties of the brush depend strongly on the relative strength of the interaction of the polymer with the aqueous environment compared to the polymer-polymer interactions. The interactions of the polymer with water, however, will be in many systems strongly altered by charge recombination.

On the other hand, if the grafting density ρ_a and/or the degree of charging f is reduced the Gouy Chapman length can become larger than the brush height h . Then the counterion distribution extends beyond the rim of the brush, and one enters the weak charging limit. In this case the direct electrostatic forces caused by locally uncompensated charges dominate chain stretching. Minimization of $F_{\text{st}} + F_{\text{el}}$ with respect to h or balancing the corresponding partial pressures

$$\pi_{\text{el}} \simeq \lambda_{\text{B}}(Nf\rho_a)^2, \quad (2.93)$$

and eqn. 2.82, in the so-called charged or Pincus brush regime (PB), the brush height reads [9]

$$h \simeq N^3(bf)^2\lambda_{\text{B}}\rho_a, \quad (2.94)$$

which is dependent on the grafting density. However, as the phase region where such interactions dominate is rather narrow and the absolute changes in brush height are expected to be quite small, an experimental confirmation of such a polyelectrolyte brush phase remains extremely difficult.

Molecular simulation studies on PEL brushes were also employed to check theoretical predictions. Following the self-consistent work in references [85] and [86], polyelectrolyte brush structure has been studied numerically by a combination of Monte Carlo and mean-field theory, using the Poisson-Boltzmann equation to handle electrostatic interactions [100]. Within the Debye-Hückel approximation, an enumeration study [91] and a Monte Carlo and self-consistent field approach were employed [102]. In reference [101], a Monte Carlo simulation of two interacting polyelectrolyte brushes was performed with a truncated Coulomb potential. Recently, molecular dynamics simulations of polyelectrolyte brushes in salt-free solution at varying grafting density and charge fraction, at both relatively strong and moderate electrostatic coupling were performed [104, 105]. In these studies, any mean-field treatment or truncation is avoided. Treating the full Coulomb interaction, counterions are included explicitly. Varying the Bjerrum length λ_{B} , a non-monotonic behavior of the brush height is obtained [105]. Furthermore, two novel brush regimes first obtained by simulation and having features not predicted by previous theories were reported. At relatively strong interaction strength $\lambda_{\text{B}} \approx 14b$ a new

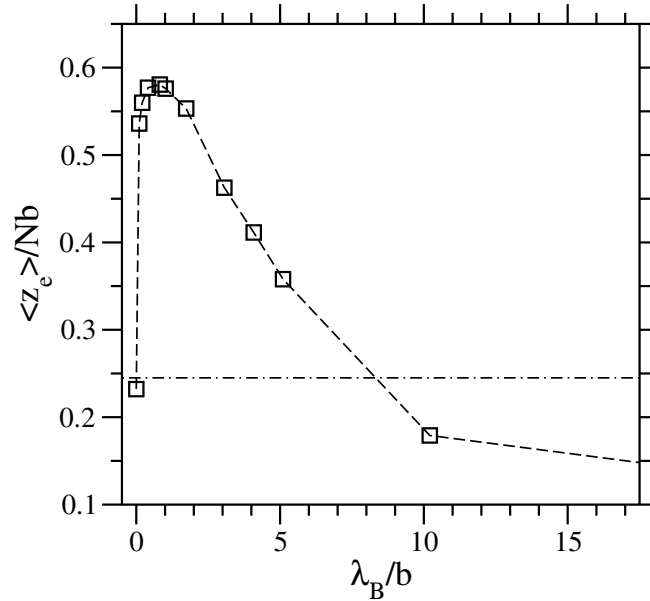


Figure 2.7: Average height of chain ends $\langle z_e \rangle$ (squares), rescaled with the contour length Nb ($N = 30$), versus Bjerrum length λ_B at grafting density $\rho_a \sigma^2 = 0.02$. The dot-dashed line indicates $\langle z_e \rangle$ of an identical system of uncharged chains.

collapsed regime is observed where the monomer density becomes independent of the grafting density resulting in a linear scaling of the brush height with ρ_a [104]. In Figure 2.7 plotted is the average height of chain ends $\langle z_e \rangle$ against the Bjerrum length λ_B for a polyelectrolyte brush with completely charged chains of length $N = 30$. Considering Figure 2.7, for $\lambda_B \gtrsim 9b$ it is observed that the stretching of the chains is indeed smaller than in a corresponding uncharged brush, indicating the influence of attraction due to electrostatic correlations.

Including electrostatic correlations, which cause an attractive interaction, the nature of the collapsed regime can be understood within an extended scaling model [93]. In the bulk and in the low density limit, for $H = h$, the DH free energy F_{DH} reads

$$F_{\text{DH}} \simeq -h \left(\frac{Nf\lambda_B\rho_a}{h} \right)^{3/2}. \quad (2.95)$$

A novel collapsed brush regime is obtained at strong coupling $\lambda_B^3 > v_2$ and strong charging $f > (v_2/\lambda_B^3)^{1/2}$ by comparing F_{v_2} and F_{DH} which give the brush height [93]

$$h \simeq N\rho_a \frac{(1+f)^4 v_2^2}{f^3 \lambda_B^3}. \quad (2.96)$$

Note that in the CB regime the DH term induces a scaling where $h \sim N\rho_a$, i.e., the system

maintains a constant particle density. An additional length scale enters, namely the Bjerrum length.

Reducing λ_B , the collapsed brush regime disappears [105] as predicted by the extended scaling model [93]. This is also evident in Figure 2.7. The maximum brush height occurs at $\lambda_B \approx b$. For smaller λ_B , the Gouy-Chapman length becomes larger than the brush height. Hence, counterions are expected to leave the brush, and the residual electrostatic repulsion between charged monomers is rather weak, leading to its relaxation back to the reduced extension of a quasi-neutral brush. Close to the maximum height a stretching of the chains up to about 2/3 of their contour length is observed. This is certainly beyond the range where Gaussian elasticity can be applied. However, contrary to the scaling law of the osmotic regime, the brush height exhibits still a weak dependence on ρ_a [105] (also see chapter 4). The corresponding brush regime is called nonlinear osmotic. This behavior can be reproduced by allowing a laterally inhomogeneous distribution of counterions [94] and/or taking into account the self-volume of polymers (see chapter 4).

2.2.2.2 PEL brushes with added salt

The picture of the polyelectrolyte brush behavior changes if salt is added to the solution. Varying salt concentration is an important parameter to tune structure and properties of PELs. Both in experiment [113–121] and in theoretical work [9,95–99], polyelectrolyte brushes with added salt form an interesting subject, where main attention is focused on the behavior of brush height and segment density profiles at varying salt concentration. Several models have been proposed to understand the effect of additional salt on the brush height (for a brief review see, e.g., references [116,117]). Consider the case when all counterions stay inside the brush layer. The addition of monovalent salt of concentration c_s gives rise to a Debye screening length $\lambda_D = \kappa_s^{-1} = (8\pi\lambda_B c_s)^{-1/2}$. With an increase in the salt concentration, the Debye screening is expected to reduce the counterion osmotic pressure, eqn. 2.91, as

$$\pi_{ci} \simeq \pi_{os} \kappa_0^2 / \kappa^2 = c_m f \kappa_0^2 / \kappa^2, \quad (2.97)$$

where polymer concentration $c_m = N\rho_a/h$, $\kappa_0^{-1} = (4\pi\lambda_B f c_m)^{-1/2}$ is the screening length associated with the counterions alone and $\kappa^2 = \kappa_0^2 + \kappa_s^2$. In the limit of $\kappa_s \gg \kappa_0$ the osmotic pressure, eqn. 2.97, becomes

$$\pi_{ci} \simeq c_m^2 f^2 / c_s \simeq v_{\text{eff}} c_m^2 \quad (2.98)$$

which is basically the expression of a second virial osmotic pressure. The effective excluded volume parameter v_{eff} , however, now reads $v_{\text{eff}} \simeq f^2/c_s$. Using eqn. 2.98 for the osmotic pressure, and balancing this against the polymer entropy loss on expanding, eqn. 2.82, yields

the scaling result [9]

$$h \simeq Nb \left(\frac{\rho_a f^2}{bc_s} \right)^{1/3}, \quad (2.99)$$

i.e., the brush height h decrease with c_s but only as a relatively weak power law. Later on the prediction has been confirmed and generalized by using refined theoretical approaches [95–98]. However, there is also a different prediction expecting a $h \sim c_s^{-2/3}$ scaling [99].

Weak polyelectrolyte brushes consist of anchored polymer chains, where an equilibrium exists between neutral, undissociated and the charged, dissociated moieties. In such systems the degree of dissociation depends on the local pH value [6]. Examples of such systems are weak polyacids. At low pH a large abundance of protons will result in a low charge density due to protonation of the salt moieties. A number of molecular parameters such as the charge density on the brush, the concentration of free counterions, and the degree of swelling can therefore be tuned via adjustment of the pH.

Upon the addition of large amounts of salt, weak polyelectrolyte brushes shrink similar to what is expected for strong polyelectrolyte brushes eq. (2.99) [6, 7, 92]. Theoretical expectations for the swelling behavior of weak brushes at low salt concentrations are, on the other hand, somewhat counter-intuitive. If only small amounts of salt are added to the solution the brush height increases. The reason for such a behavior is that the local concentration of protons in the brush is governed by the requirement of charge neutrality. However, when the ambient solvent contains ions other than protons, some of these cations can be exchanged with the protons without violation of charge neutrality. Hence, the degree of dissociation of the acid/base moieties on the polymer chains changes. Generally, some of the cations might also recombine with the acidic groups to yield a salt. The binding constant for this kind of association, however, is much lower than the binding constant of the pure acid/base equilibrium. As a consequence, a net increase of charge therefore remains, resulting in an increase in osmotic pressure. Thus the height of the weak polyacid brush increases with increasing salt concentration. This process has been thoroughly studied [6, 7, 92]. The outcome is a weak power law dependency predicted for the scaling of the brush height on the salt concentration,

$$h \simeq Nbc_s^{1/3} \rho_a^{-1/3}. \quad (2.100)$$

2.2.2.3 Donnan equilibrium for PEL brushes

In the present analysis, consider the polyelectrolyte brush as a system that consists of two different solutions separated by a semi-permeable membrane, permeable to small ions but not to macroions. As first pointed out in 1911 by F.G. Donnan [160], the difference of the electrostatic potential on both sides of the membrane causes a unequal distribution of the small ions.

Thermodynamic parameters on the polymer-free side will be designated by a single prime

while doubly primed ones are related to the polymer-containing part. For simplicity, we are dealing with 1-1 electrolytes and the macroion counterions are assumed to be identical to the salt counterions. Consider macroions of charge $Z = fN$ while M^+ and X^- are to refer to the small ions, both of originally counterions and of an added salt.

To study the thermodynamic behavior of electrolytes in solution it is appropriate to express the composition of the solution not in terms of the ionic species but in terms of neutral components. A convenient definition uses the following three components: component 1 - solvent (usually water), component 2 - macroion + $Z/2$ ions X^- - $Z/2$ ions M^+ , component 3 - neutral salt, MX . Because we are interested in the equilibrium distribution of the small ions, here we focus the analysis on component 3. The condition for thermodynamic equilibrium is given by the equality of the corresponding chemical potentials

$$\mu'_3 = \mu''_3. \quad (2.101)$$

For simple 1-1 electrolytes, it is most convenient to transform eq. (2.101) into a relation between activities a_i . On the side free from macroions, we have directly

$$\mu'_3 = \mu_3^0 + RT \ln a'_3. \quad (2.102)$$

where μ_3^0 is the chemical potential at a reference state. Neglecting the effect of the osmotic pressure, that gives for reasonable parameters a change in a_3 of about 0.05% [161], on the macroion-containing side it holds a similar expression

$$\mu''_3 = \mu_3^0 + RT \ln a''_3. \quad (2.103)$$

Thus, eq. (2.101) becomes simply

$$a'_3 = a''_3. \quad (2.104)$$

Since the activity of an electrolyte is the product of the constituent ion activities, $a_3 = a_+ a_-$, eq. (2.104) yields

$$a'_+ a'_- = a''_+ a''_-. \quad (2.105)$$

Replacing the activity by the product of ion concentration c_{\pm} and ion activity coefficient γ_{\pm} , $a_{\pm} = c_{\pm} \gamma_{\pm}$, and assuming the same activity coefficients on both sides, eq. (2.105) gives

$$\frac{n'_+ n'_-}{(L_z - h)^2} = \frac{n''_+ n''_-}{h^2}, \quad (2.106)$$

where n'_+ (n'_-) and n''_+ (n''_-) are the number of positive (negative) ions in the polymer-free and polymer-containing side, respectively. The demarcation line between the two sides is given by the brush height h which in our case is determined by the inflection point height z_i (see Sec. 5.1). L_z is the total height of the simulation box. Additionally, we have the condition of

electroneutrality on both sides, that gives

$$\frac{n'_+}{L_z - h} = \frac{n'_-}{L_z - h} \equiv \frac{c'_s}{\rho_a}. \quad (2.107)$$

and

$$n''_+ - n''_- = fN, \quad (2.108)$$

respectively, where c_s is the salt concentration. The combination of eqs. (2.106) - (2.108) yields

$$\begin{aligned} n''_+{}^2 - fNn''_+ &= c'_s{}^2 \left(\frac{h}{\rho_a} \right)^2, \\ n''_-{}^2 + fNn''_- &= c'_s{}^2 \left(\frac{h}{\rho_a} \right)^2. \end{aligned} \quad (2.109)$$

Defining the corresponding concentrations of small ions by $c''_{\text{si}} = (n''_+ + n''_-)\rho_a/h$ and $c'_{\text{si}} = (n'_+ + n'_-)\rho_a/(L_z - h)$, finally one obtains for the ratio of small ions on both sides

$$\frac{c'_{\text{si}}}{c''_{\text{si}}} = \left[1 + \left(\frac{fN\rho_a}{2hc'_s} \right)^2 \right]^{-1/2}, \quad (2.110)$$

which represents the classical Donnan equilibrium expression for the particular brush system. Note the asymptotic behavior at large salt concentration where eq. (2.110) gives $c'_{\text{si}} = c''_{\text{si}}$, i.e., a homogeneous distribution at the whole system. However, below we will see that the assumption of point-like ions made in the derivation of eq. 2.110 disagrees with simulation results due to high concentration in the brush state (see section 5.4).

2.2.2.4 Interacting PEL brushes

Interactions between two PEL brushes have received lot of attention recently, the main challenge being to capture and understand structure and forces in such systems under various conditions [9, 119, 122–125]. PEL brushes attached to surfaces rubbing across an aqueous medium provide means of efficient lubrication [123]. Inspired by biology, scientist are trying reduce mechanical wear by using biolubrication [124].

Recently, using surface forces apparatus the forces arising from two opposing PEL layers of sodium poly(styrenesulfonate) anchored at solid-liquid interface have been measured [119]. In the regions of weaker compression of the brushes, the experimental force-distance profiles are successfully explained based on equations derived from the scaling theory by Pincus [9]. Differences occur for higher compression where it appears that there is more resistance to compression of the two PEL layers in the high salt regime than at low concentration of additional salt. In this situation, simulation could provide further insight into the behavior of interacting

PEL layers and stimulate further development of the theory.

The scaling arguments by Pincus for two PEL brushes compressed between walls is based on the osmotic pressure of counterions in the brush. The pressure (at or below the region where the brushes start to overlap) reads (see eqn. 2.91)

$$\pi \simeq fN\rho_a/D, \quad (2.111)$$

where D is the separation between the two anchoring planes.

At large separations D where the brushes may not overlap, however the counterions can still interact. For surface force measurements on weakly charged interacting PEL brushes, where the counterions extend well beyond the brush, the double layer theory (DLVO) can explain the $\pi - D$ relation, but the theory is not satisfactory at high compressions [122, 123]. The situation might be different in the case of strongly charged brushes because the counterions stay inside the brush and any long range effects might not be obtained in the interaction force profiles [119].

Chapter 3

Simulation model and method

In recent years computer simulation has become a major tool in polymer science complementing both analytical theory and experiment. Simulations are able to check theoretical models and to probe quantities and regimes which are not easily observable experimentally [141]. However, despite strong efforts in recent years [142], simulations of PELs remain still challenging. First, long chain molecules relax slowly, and the energy landscape of a dense polymer system is highly complex containing large regions of metastability. To obtain satisfactory statistics, one has to resort to long simulation times. Second, the correct treatment of the long-ranged Coulomb interaction in a periodic system requires special methods which are computationally expensive (see section 3.2.2). This task is even more demanding in a brush geometry with planar periodicity in the anchoring plane and a finite slab perpendicular to this plane. Here, a straightforward application of Ewald sums is not possible [143]. Third, special attention on finite system size has to be taken due to the long-range nature of Coulomb interactions. For the reasons outlined above, only a few simulation studies of polyelectrolyte brushes are known in literature [100–105].

Usually the most time consuming part in the simulation code for PELs is the evaluation of Coulomb interactions. In principle, each charge q_i at position \mathbf{r}_i interacts with all others, leading to a computational effort of $\mathcal{O}(N_{\text{tot}}^2)$ already within the central simulation box (N_{tot} is the total number of charged particles). For many physical investigations one wants to simulate bulk properties and therefore introduces periodic boundary conditions to avoid surface effects [156]. The Coulomb energy then has to be computed as a sum over all periodic images which can be done, for instance, using the Ewald summation method [22]. However, the computational times have been so long that simulations of PELs have used, e.g., the minimum image method which only include all Coulomb interaction within the minimum image [135], and the Debye-Hückel (DH) approximation (eqn. 2.68) for the Coulomb interaction [102, 133, 134]. The advantage of DH approximation is that the potential is finite ranged and counterions and salt ions are not simulated explicitly. Thus, DH simulations are much faster than ones which explicitly treat each Coulomb interaction. But the general disadvantage of

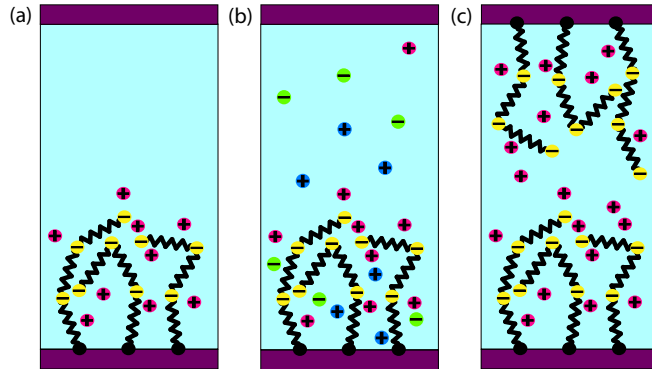


Figure 3.1: Schematic representation of the simulation model: (a) PEL brush; (b) PEL brushes with added salt; (c) two interacting PEL brushes.

the DH approximation is that it is not probably realistic for many of the relevant range of parameters, except at very dilute concentrations, high salt concentrations or for Coulomb interaction energies less than thermal energy $k_B T$. Hence, DH approximations are typically suspect for strongly charged polyelectrolytes because the Coulomb interaction energies for these systems are often greater than $k_B T$. That is why for the simulation of PEL brushes, the full Coulomb interaction of monomers, counterions, and salt ions is explicitly treated here.

This chapter presents the simulation model and method used to study polyelectrolyte brushes. The technical task to treat long ranged Coulomb interaction, especially applied to the brush system, is also discussed.

3.1 Simulation model

In this study an off-lattice model (see Figure 3.1(a)) is used where the brush is represented by M freely jointed bead-spring chains of length $N + 1$ which are anchored by one end to an uncharged planar surface at $z = 0$. Within the simulation box of size $L \times L \times L_z$ the grafting density is given by $\rho_a = M/L^2$. The uncharged anchor segments are fixed and form a square lattice with lattice spacing $d = \rho_a^{-1/2}$. For completely charged chains, due to electroneutrality there are $M \times N$ monovalent counterions. Additional salt ions of monovalent 1:1 type are modeled exactly in the same way as counterions (Figure 3.1(b)). For a system of two apposing planar surfaces with grafted polyelectrolytes, the model is identical to the brush grafted to a single planar surface except that a second similarly anchored brush is assigned to the top planar surface.

The chains are assumed to be in a good solvent modeled by a purely repulsive short-range

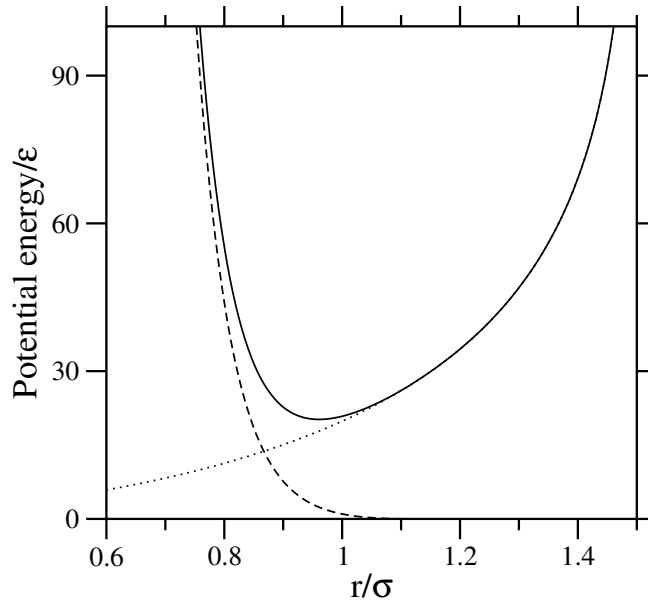


Figure 3.2: Potential energy functions for the bead-spring chains. Shown are the FENE (dotted line), repulsive Lennard-Jones (dashed line), and their sum (solid line). Note that the maximum bond extension $R_0 = 1.5\sigma$.

interaction which is described by a shifted Lennard-Jones potential

$$u_{\text{LJ}}(r) = \begin{cases} 4\epsilon \left\{ \left(\frac{\sigma}{r}\right)^{12} - \left(\frac{\sigma}{r}\right)^6 - \left(\frac{\sigma}{r_c}\right)^{12} + \left(\frac{\sigma}{r_c}\right)^6 \right\}, & \text{if } r < r_c \\ 0, & \text{if } r \geq r_c, \end{cases} \quad (3.1)$$

where the cutoff radius is $r_c = 2^{1/6}\sigma$ and ϵ, σ are the usual Lennard-Jones parameters. For simplicity, we assume that monomers, counterions, and the added salt ions have the same Lennard-Jones diameter σ as well as energy ϵ . Henceforth, ϵ and σ are used as basic units of the model. In addition to the repulsive potential, beads being neighbors along the polymer chains are coupled by a FENE (finitely extensible nonlinear elastic) bond potential (which is of an empirical origin) [141]

$$u_{\text{bond}}(r) = \begin{cases} -\frac{kR_0^2}{2} \ln \left\{ 1 - \left(\frac{r}{R_0}\right)^2 \right\}, & \text{if } r < R_0, \\ \infty, & \text{if } r \geq R_0, \end{cases} \quad (3.2)$$

with bond strength $k = 30\epsilon/\sigma^2$ and maximum bond length $R_0 = 1.5\sigma$. These parameters ensure that a reasonable time step can be employed in simulations but bond crossings are en-

ergetically infeasible [152]. Figure 3.2 shows the plot of potential energy functions of Lennard-Jones, FENE and their sum for a pair of bonded monomers. For uncharged chains, this choice of parameters gives an average bond length of $b = 0.97\sigma$ [77]. The Coulomb repulsion between adjacent monomers slightly stretches the bond length compared to uncharged chains, where $b = 0.98\sigma$ has been reported, which fluctuates by about 4% [104].

All particles except anchor segments interact repulsively with the grafting surface at short distances. The exact form of the wall potential is arbitrary. In principle, one can use any strongly repelling short-range potential. Here we use a potential similar to the shifted Lennard-Jones potential introduced in eq. (3.1) which vanishes smoothly as $z \rightarrow 0.5\sigma$

$$u_{\text{wall}}(z) = \begin{cases} 4\epsilon \left[\left(\frac{\sigma}{z + \Delta z} \right)^{12} - \left(\frac{\sigma}{z + \Delta z} \right)^6 + \frac{1}{4} \right], & \text{if } z < 0.5\sigma \\ 0, & \text{if } z \geq 0.5\sigma, \end{cases} \quad (3.3)$$

with $\Delta z = (2^{1/6} - 0.5)\sigma$.

In addition to the repulsive wall potential at the $z = 0$ plane, a similar potential is assigned to the top boundary of the simulation box at $z = L_z$. This model construction ensure that divergences at large Gouy-Chapman lengths is prevented. In earlier simulation studies [104, 105], setting $L_z = 3N\sigma$ for completely charged chains ensured that the counterions never visit the $z = L_z$ boundary in the course of the simulations. With additional salt ions, however, the second wall is necessary to reach a finite salt concentration.

Counterions and salt ions are treated as individual, non-bonded particles and all charged entities interact with the bare Coulomb interaction

$$u_{\text{Coul}}(r) = k_B T q_i q_j \frac{\lambda_B}{r}, \quad (3.4)$$

with q_i and q_j being the corresponding charges in units of elementary charge e , and λ_B is the Bjerrum length (see eqn. 2.69).

The implementation of the long-range Coulomb interaction requires special care. The simulation box has periodic boundary conditions only in x and y directions while perpendicular to the grafting surface (z -direction) the system is restricted to one layer. A technique introduced by Strebel and Sperb [144] and modified by Arnold and Holm [145] for laterally periodic systems (MMM2D) is applied to account for the long-range nature of Coulomb interactions. This algorithm's computation time scales as $\mathcal{O}(N_{\text{tot}}^{5/3} \log(N_{\text{tot}})^2)$, where N_{tot} is the total number of charged particles. Although the resulting relation scales only with $\mathcal{O}(N_{\text{tot}}^{5/3} \log(N_{\text{tot}})^2)$, already for $N_{\text{tot}} > 100$ the factor becomes larger than unity when compared with $\mathcal{O}(N_{\text{tot}}^2)$ methods, for e.g., the method due to Lekner [146]. Such scaling is essential to perform these calculations as added salt increases number of charged particles significantly. The implementation of the long-range Coulomb interaction is further detailed in section 3.2.2 where also the relation

between the $\mathcal{O}(N_{\text{tot}}^2)$ method and the $\mathcal{O}(N_{\text{tot}}^{5/3} \log(N_{\text{tot}})^2)$ method is discussed in detail.

The system is assumed to have a matching ε boundary condition, so that no image charges appear across the anchoring surface. This assumption is also implicitly made in theoretical treatments of charged brushes. In experiments however the grafting substrate (e.g., air sub-phase) will generally have a lower dielectric constant than water. In this case, an estimate of the image charge energy has been given by Wittmer and Joanny [89]. For highly charged and densely grafted systems, the lateral charge density is approximately uniform and image charge effects are expected to be small.

3.2 Simulation method

To study the system in equilibrium, we use stochastic molecular dynamics [152, 156]. The equation of motion for particle i at position $\mathbf{r}_i(t)$ is the Langevin equation,

$$m \frac{d^2 \mathbf{r}_i}{dt^2} = -\nabla_i U - m\Gamma \frac{d\mathbf{r}_i}{dt} + \mathbf{W}_i(t), \quad (3.5)$$

where all particles carry the same mass m and Γ is a friction constant which couples the particles to a heat bath. U is the potential energy

$$U = U_{\text{LJ}} + U_{\text{bond}} + U_{\text{wall}} + U_{\text{Coul}}. \quad (3.6)$$

The system is held at thermal equilibrium by a Gaussian random force $\mathbf{W}_i(t)$

$$\begin{aligned} \langle \mathbf{W}_i(t) \rangle &= 0, \\ \langle \mathbf{W}_i(t) \cdot \mathbf{W}_j(t') \rangle &= 6mk_{\text{B}}T\Gamma \delta_{ij}\delta(t-t'), \end{aligned} \quad (3.7)$$

where the coupling to Γ is a consequence of the fluctuation-dissipation relation. For free diffusive motion, the Einstein relation leads to an overall diffusion constant [2] $D_{\text{free}} = k_{\text{B}}T/m\Gamma$.

3.2.1 Parameters and integration scheme

The simulation parameters chosen for the study of PEL brushes are given in Table 3.1. The mass m is set to unity. The simulation method described above to be efficient, the value of friction coefficient Γ cannot be too small, since then the coupling to the heat bath will be too weak and the system will not sample phase space very well. However, if the coupling is too strong, then the viscous damping term and the random force term dominate over the inertia term in eq. 3.5. The motion will be then dominated by Langevin dynamics even for very early times and there would be very little cooperative motion of monomers, which is important in particularly dense systems. In this limit the algorithm will also be very ineffective. For a given bead friction, the motion of a monomer for $t < \Gamma^{-1}$ is undamped, subject to only the chain

constraint, while for $t \gg \Gamma^{-1}$ the motion is Rouse-like¹.

For a given preset temperature $k_B T = 1.2\epsilon$, equation (3.5) was integrated by means of the velocity-Verlet algorithm [156] with a time step $\delta t = 0.008\tau_{LJ}$, where $\tau_{LJ} = (m\sigma^2/\epsilon)^{1/2}$. Γ is chosen to be $0.5\tau_{LJ}^{-1}$ [155]. For a Newtonian trajectory with a quite similar time step, the total energy fluctuations have shown to be less than 10^{-4} [104]. However, to simulate at a particular temperature but with different solvent qualities can be achieved by, for instance, choosing different r_c in the LJ potential [131].

A Gaussian distributed noise in eqn. 3.7 was used [153]. However, the Gaussian noise term can also be replaced by equally distributed random numbers, which has the same mean and second moment as required by eqn. 3.7 [154].

In principle, for not so large Γ so that the inertia term becomes irrelevant, eqn. 3.5 can be integrated with any standard algorithm, where third- and fifth- order predictor-corrector [156] and velocity-Verlet algorithms have been tested [155]. For similarly chosen simulation parameters as above, the velocity-Verlet algorithm was found to be stable for a time step δt about a factor of two larger than for the predictor-corrector algorithm [155].

The velocity-Verlet algorithm takes the form [156]

$$\mathbf{r}(t + \delta t) = \mathbf{r}(t) + \delta t \mathbf{v}(t) + \frac{1}{2} \delta t^2 \mathbf{a}(t), \quad (3.8)$$

$$\mathbf{v}(t + \delta t) = \mathbf{v}(t) + \frac{1}{2} \delta t [\mathbf{a}(t) + \mathbf{a}(t + \delta t)]. \quad (3.9)$$

It is implemented as follows. Firstly, the new position at time $t + \delta t$ are calculated using eqn. 3.8, and the velocities at mid-step are computed using

$$\mathbf{v}(t + \frac{1}{2}\delta t) = \mathbf{v}(t) + \frac{1}{2} \delta t \mathbf{a}(t). \quad (3.10)$$

The forces and accelerations at time $t + \delta t$ are then computed, and the velocity move completed

$$\mathbf{v}(t + \delta t) = \mathbf{v}(t + \frac{1}{2}\delta t) + \frac{1}{2} \delta t \mathbf{a}(t + \delta t). \quad (3.11)$$

The whole process is iterated using the newly computed position and velocity. Since we get the velocities at each time step from eqn. 3.11, the instantaneous temperature can be calculated as [156]

$$\left\langle \sum_{i=0}^{N_{\text{tot}}} m_i |\mathbf{v}_i^2| \right\rangle = 3N_{\text{tot}} k_B T, \quad (3.12)$$

where N_{tot} is the total number of particles. However, since the force calculation depends on positions as well as on velocities, the plain integration velocity scheme, eqns. 3.8, 3.9, 3.10 and

¹The Rouse model [136] for the dynamics of a single polymer describes the motion of an ideal chain immersed in a viscous solvent by a Langevin equation. This model neglects the self-repelling of the chain monomers as well as any hydrodynamic effects [137].

Table 3.1: Simulation parameters and length scales.

Mass m	1
Temperature $k_B T$	1.2ϵ
Friction constant Γ	$0.5\tau_{LJ}^{-1}$
Time step δt	$0.008\tau_{LJ}$
Monomer number N	30
Number of chains M	36
Grafting density	$\rho_a = M/L^2 \approx (0.02 \dots 0.15)\sigma^{-2}$
Degree of charging	$f = N_c/N = 1$
Bjerrum length	$0 < \lambda_B/b < 20$
Salt concentration	$0 < c_s\sigma^3 < 0.2$
Particle number N_{tot}	≤ 10000

3.11 needs to be modified [162]. The modified relations reveals that \mathbf{v} and \mathbf{a} differ from the above schemes by terms of the order δt^2 for the velocity and δt for the acceleration. Since some test simulations showed no difference between the two implementations, the above mentioned scheme is chosen for the present work.

Three types of finite size effects may interfere with the simulation results discussed below. First, the chain length N should be long enough to capture typical polymeric behavior. Second, because of possible self-interaction of chains, a small lateral system size due to the restricted number of chains M may also influence the large scale properties such as brush thickness. In this study we have considered systems with $M = 36$ polyelectrolyte chains, each consisting of an uncharged fixed anchor and $N = 30$ negatively charged free chain monomers. With this particular choice of system size both types of finite size effects can be kept small [104]. In previous simulations without additional salt ions there were no limitations of L_z , except arguments of numerical accuracy [104]. Therefore it could be chosen large enough that collisions of counterions with the top boundary of the simulation box were in fact rare events. For small Bjerrum lengths, however, the Gouy-Chapman length becomes large and L_z has to be taken of the order of some multiples of polymer contour length. Obviously with added salt the situation is drastically changed because in any case a second wall potential at $z = L_z$ is necessary to maintain the desired finite salt concentration. On the other hand box heights should be chosen as small as possible because additional salt ions will occupy preferentially the free space above the brush and one would have to add a rather larger number before succeeding with a remarkable concentration within the brush. However, reducing L_z a third kind of finite size effect might become important. To check this problem we studied carefully the influence of a variation in box height on the structure of the brush.

In Figure 3.3 the monomer density profiles are compared for three different heights L_z

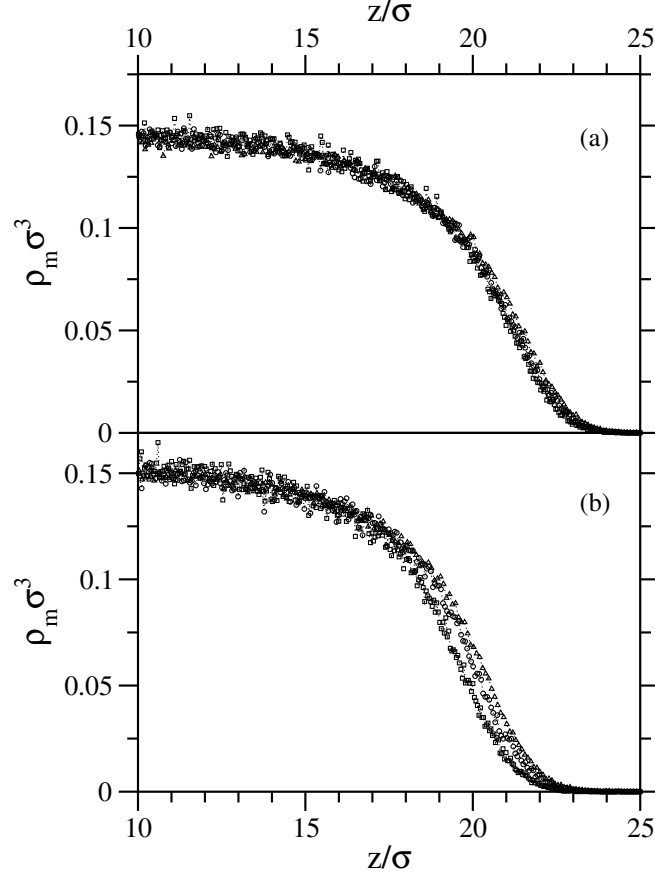


Figure 3.3: Monomer density $\rho_m(z)$ as function of the distance from grafting surface at $\rho_a = 0.094\sigma^{-2}$ for three different box heights: $L_z = 1.5N\sigma$ (squares), $L_z = 2N\sigma$ (circles), $L_z = 3N\sigma$ (triangles). Shown is the outer part of the brush being eventually affected by the finite box height. a) $c_s \sigma^3 = 0.016$, b) $c_s \sigma^3 = 0.042$.

while all the other simulation parameters were kept constant. The plots are shown for two different salt concentrations. At the very tails, the profiles obtained with $L_z = 1.5N\sigma$ clearly deviate from those with $L_z = 3N\sigma$, indicating a finite size effect at box height $L_z = 1.5N\sigma$. The effect is enlarged with increasing salt concentration. On the other hand a fairly good agreement is found between the profiles obtained for $L_z = 3N\sigma$ and $L_z = 2N\sigma$. Therefore, if not otherwise stated, we use a box height $L_z = 2N\sigma$ in the simulations reported here. Note that the suitability of the particular choice is also supported by the scaling behavior discussed in chapter 5 where data obtained with both L_z equal to $2N\sigma$ and $3N\sigma$ are included (see Figure 5.5). The numerical results given in Table 5.1 show that, for different box heights, but at identical system parameters the average brush height differs by 2% at maximum; in a large range the difference is less than 1%.

The polymer model used here can be viewed as a coarse-grained representation of a flexible

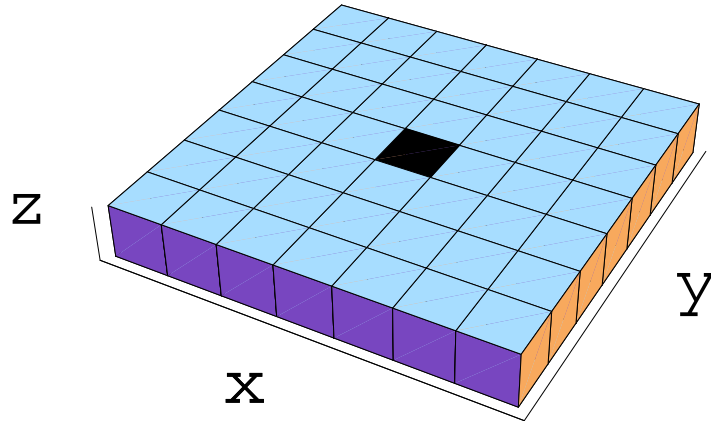


Figure 3.4: Schematic picture showing 2D+1 slab geometry. The central box (shaded dark) repeats to infinity in x and y -directions, respectively, while has a finite length in the z -direction.

polyelectrolyte such as, e.g., poly(styrene sulfonate) (PSS). The length scale of the model is set by the Bjerrum length λ_B which is about 0.7 nm for water at room temperature. Therefore, with the setting $\lambda_B = \sigma$, the average bond length b becomes approximately 0.7 nm and the dimensionless manning ratio is $\lambda_B/b = 1$, same as the Manning condensation limit for a fully stretched chain. Using for PSS a monomer size of about 0.25 nm, one results with a fraction of charged monomer $f \approx 1/3$. In comparison, Manning theory predicts a charge fraction $f = 0.25 \text{ nm}/0.7 \text{ nm} = 0.35$ for a fully stretched PSS chain in water.

3.2.2 Coulomb forces in 2D+1 slab geometry

It is well known that the handling of long-range forces in simulations requires special methods [156]. To treat them in the particular 2D+1 slab geometry (see Figure 3.4) where the simulation box is periodic only in x and y directions while perpendicular to the grafting surface the system is restricted to one layer, previous simulations [93, 104, 105] used a direct summation technique proposed by Lekner [146] and modified by Sperb [147, 148]. This approach is, however, a so-called $\mathcal{O}(N_{\text{tot}}^2)$ method where the CPU time scales with square of the total number of charged particles N_{tot} . Unfortunately, such a behavior results in drastic restrictions on the maximum system size being accessible by simulation.

In the new simulation code implemented here, the Lekner method is replaced by the so-called MMM technique introduced by Strebel and Sperb [144] and modified for laterally periodic systems (MMM2D) by Arnold and Holm [145]. Although, due to symmetry breaking, the MMM scaling $\mathcal{O}(N_{\text{tot}} \log(N_{\text{tot}}))$ is not maintained in the 2D + 1 case, the remaining $\mathcal{O}(N_{\text{tot}}^{5/3} \log(N_{\text{tot}})^2)$ behavior enables to increase significantly the total number of charged particles. Figure 3.5 shows the performance gain defined by the ratio of the corresponding CPU

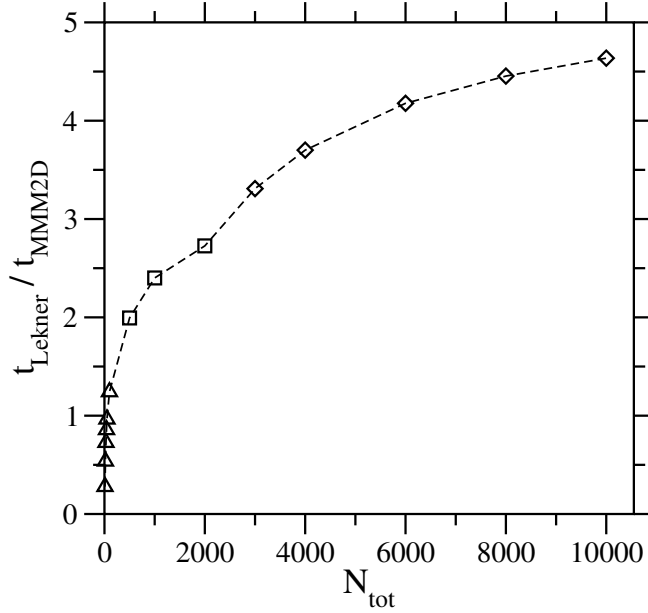


Figure 3.5: Performance gain between the MMM2D approach and Lekner's method measured by the relation between corresponding CPU times as a function of particle number N_{tot} . Different symbols correspond to a different number of layers the simulation box is subdivided in the MMM method: 8 (triangles), 16 (squares) and 32 (diamonds).

times as a function of particle number. Note that the dip at $N_{\text{tot}} \approx 2000$ is related to a change in the number of layers the simulation box is subdivided in the MMM method. Infact, already for about 100 particles the MMM2D turns out to be faster than Lekner's method. The considerable performance gain allows to increase the maximum number of charges from about 2000 up to more than 7000. Finally, we are indeed able to add a sufficiently large number of salt ions to reach reasonable concentrations.

In the above mentioned methods, generally one has to do the Coulomb summation for particles in the central simulation box as well as in the image boxes which is given as (for 2D+1 periodic systems)

$$U_{\text{Coul}}(r) = \frac{e^2}{4\pi\epsilon_0\epsilon} \sum_{k=-\infty}^{\infty} \sum_{l=-\infty}^{\infty} \sum_{i=1}^{N_{\text{tot}}-1} \sum_{j=i+1}^{N_{\text{tot}}} \frac{q_i q_j}{|\mathbf{r}_{ij} + kL\mathbf{e}_x + lL\mathbf{e}_y|}, \quad (3.13)$$

where $\mathbf{r}_{ij} = \mathbf{r}_i - \mathbf{r}_j$ (\mathbf{r}_i and \mathbf{r}_j are the position vectors of particle i and j , respectively), \mathbf{e}_x and \mathbf{e}_y are unit vectors in x - and y -direction respectively, and the indices k and l run over the periodic images of the simulation box. ϵ_0 and ϵ are the vacuum permittivity and the dielectric constant of the solvent, respectively, and q_i is the charge of particle i in units of the elementary charge e . N_{tot} is the total number of charges, and L is the planar box length.

This sum is merely conditionally convergent, meaning that its value depends on the summation order. A typical choice for the order of the summation is a spherical limit, i.e. the vectors $k\mathbf{e}_x$ and $l\mathbf{e}_y$ are added in the order of increasing length. Then U_{Coul} can be computed, e.g., via the traditional Ewald summation method [22, 149]. The basic idea of this method is to split the original sum via a simple transformation involving the splitting parameter α into two exponentially convergent parts [22],

$$U(r) = U_s(r) + U_l(r), \quad (3.14)$$

where

$$U_s(r) = \frac{1}{r} - \frac{\text{erf}(\alpha r)}{r} = \frac{\text{erfc}(\alpha r)}{r}, \quad (3.15)$$

and

$$U_l(r) = \frac{\text{erf}(\alpha r)}{r}. \quad (3.16)$$

erf is the error function defined by [139]

$$\text{erf}(x) = \frac{2}{\sqrt{\pi}} \int_0^x e^{-t^2} dt. \quad (3.17)$$

$U_s(r)$ is short-ranged and evaluated in real space, while $U_l(r)$ is long-ranged and can be analytically Fourier transformed and evaluated in Fourier space. It can be shown that the potential $U_l(r)$ corresponds to a Gaussian shaped charge distribution [156]. For any choice of the Ewald parameter α and no truncation in the sums the formula yields the exact result. In practice one cuts off the infinite sums at some finite values and obtains U_{Coul} to a user controlled accuracy, which can be possible by using, e.g., error estimates for the cut-offs [138]. However, methods based on Ewald summation are mostly $\mathcal{O}(N_{\text{tot}}^2)$ in computation [149, 150]. Another approach is to transform the sum over all periodic images in the plane into a rapidly convergent expansion in terms of Bessel functions and is evaluated pairwise [146]. Again, the method has the disadvantage of being an $\mathcal{O}(N_{\text{tot}}^2)$ method. An alternative way of computing eqn. 3.13 is to use an exponential convergence factor [145],

$$U_{\text{Coul}}(r) = \lim_{\beta \rightarrow 0} \frac{e^2}{4\pi\epsilon_0\epsilon} \sum_{n_x=-\infty}^{\infty} \sum_{n_y=-\infty}^{\infty} \sum_{i=1}^{N_{\text{tot}}-1} \sum_{j=i+1}^{N_{\text{tot}}} \frac{q_i q_j e^{-\beta|\mathbf{r}_{ij} + n_x L\mathbf{e}_x + n_y L\mathbf{e}_y|}}{|\mathbf{r}_{ij} + n_x L\mathbf{e}_x + n_y L\mathbf{e}_y|} \quad (3.18)$$

This idea was originally proposed by Strebler and Sperber for 3D periodic systems [144]. For 2D systems summation using the convergence factor, eqn. 3.18, gives exactly the same results as the spherical limit, eqn. 3.13 [145]. For particles well separated, a far formula is employed which can be evaluated in the Fourier space while for N_b neighboring particles a near formula is used. As already discussed above, particularly for large N_{tot} , this method is much faster than usual $\mathcal{O}(N_{\text{tot}}^2)$ methods. For details of the MMM2D method see Appendix A.

There are also other methods, e.g., P³M (particle-particle particle-mesh) mesh-Ewald method [151], which gives a better scaling compared to $\mathcal{O}(N_{\text{tot}}^2)$ methods [129, 130].

3.2.3 Equilibration and error estimates

Fully stretched chains with a line of counterions were used as initial configuration. The salt ions were distributed homogeneously in the simulation box. The initial velocity for particles were drawn from a Maxwell-Boltzmann distribution. The relaxation was monitored by studying the decay of the endpoint height of the chains. In addition, the convergence of the cumulative average for various observables (endpoint height, potential energy and density profiles) were observed. Below a brief survey on the equilibration procedure is discussed, where in general the route suggested by Csajka and Seidel [104] is applied. The autocorrelation functions can be estimated as

$$C_X(t) = \frac{\langle (X(t) - \langle X \rangle)(X(0) - \langle X \rangle) \rangle}{\langle X^2 \rangle - \langle X \rangle^2}, \quad (3.19)$$

where X , e.g., is the average brush thickness $\langle z_m \rangle$ or the average endpoint height $\langle z_e \rangle$, defined in eq. 4.1 (see chapter 4), with notations $C_m(t)$ and $C_e(t)$, respectively. A relaxation time τ_m is obtained from $C_m(t)$ using [77]

$$\tau_m = \frac{\int_0^T C_m(t) dt}{(1 - C_m(T))}. \quad (3.20)$$

The autocorrelation function $C_m(t)$ of the brush height is shown in Figure 3.6. The decay of $C_m(t)$ is modulated by oscillations of the brush height. The salient features of relaxation are: The decay of $C_m(t)$ is approximately exponential at short times. The relaxation time τ_m generally increases for increasing chain length [104], although this trend is far less pronounced than for neutral chains in a good solvent [77]. Also, brushes with higher anchoring densities lead to longer relaxation time [104] consistent with the power law $\tau_m \propto \rho_a^\lambda$, $\lambda \approx 1$, observed for neutral brushes [77].

As an additional check of equilibration three different initial configurations were considered: one with salt ions homogeneously distributed (see above), second with all salt ions confined above the fully stretched chains, and third with all salt ions completely inside the polymer layer. All simulation runs converged to the same equilibrium values. Typically, the relaxation of brushes take some hundreds of τ_{LJ} . After reaching equilibrium, trajectories between $2000\tau_{\text{LJ}}$ and $3000\tau_{\text{LJ}}$ were calculated depending on the anchoring density. With this trajectory lengths one can ensure that the relative error of the average height of chain ends is less than 1%.

For the simulation results, errors were estimated by computing block averages [156] and by monitoring cumulative averages [158]. For τ_{run} number of time steps, the run average (or

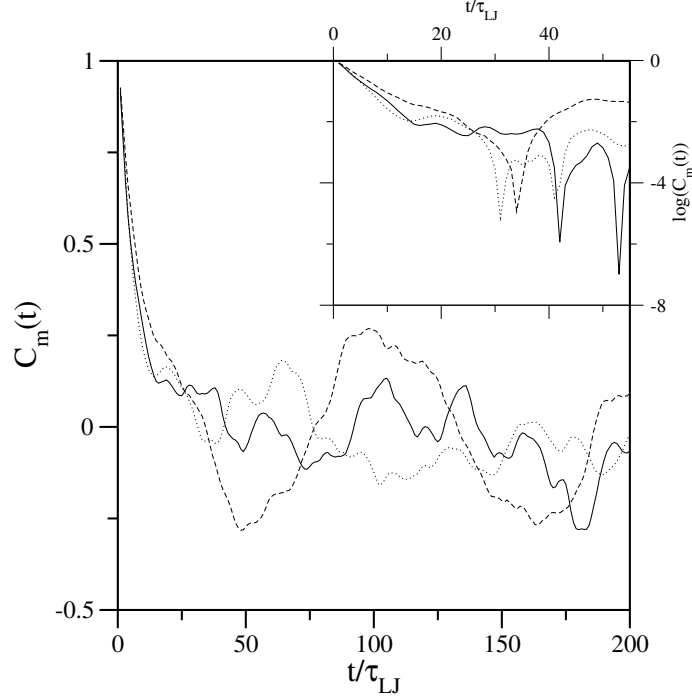


Figure 3.6: Autocorrelation function $C_m(t)$ of the brush height. Shown are chains of length 30 and grafting densities $\rho_a \sigma^2 = 0.094$ (solid line), $\rho_a \sigma^2 = 0.0625$ (dotted line), and $\rho_a \sigma^2 = 0.042$ (dashed line). Inset: Autocorrelation function $C_m(t)$ of the mean brush height on a semilogarithmic scale, same symbols as in main plot.

mean) of a statistical variable \mathcal{A} is defined as

$$\langle \mathcal{A} \rangle_{\text{run}} \equiv \frac{1}{\tau_{\text{run}}} \sum_{\tau=1}^{\tau_{\text{run}}} \mathcal{A}(\tau). \quad (3.21)$$

If each data point $\mathcal{A}(\tau)$ is statistically independent of the others, the variance in the mean is

$$\sigma^2(\langle \mathcal{A} \rangle_{\text{run}}) = \sigma^2(\mathcal{A})/\tau_{\text{run}}, \quad (3.22)$$

where

$$\sigma^2(\mathcal{A}) = \frac{1}{\tau_{\text{run}}} \sum_{\tau=1}^{\tau_{\text{run}}} (\mathcal{A}(\tau) - \langle \mathcal{A} \rangle_{\text{run}})^2. \quad (3.23)$$

The estimated error in the mean is given by $\sigma(\langle \mathcal{A} \rangle_{\text{run}})$. However, in real simulations this is not the case, i.e., the data points are usually not independent. To handle this problem the sequence of measured values of the quantity \mathcal{A} is broken up into blocks each of length τ_b . The

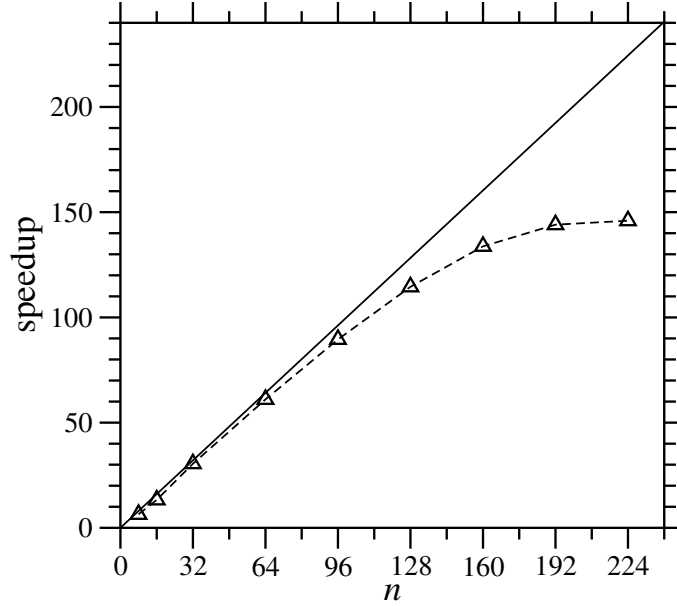


Figure 3.7: Parallel computing: Speedup vs. number of processors n for a PEL brush system having $M = 36$ chains of length $N = 30$ at grafting density $\rho_a \sigma^2 = 0.063$ and salt concentration $c_s \sigma^3 = 0.014$ following a Newtonian trajectory ($\lambda_B = \sigma, f = 1$). The solid line shows the linear or ideal speedup ($\frac{t_1}{t_n} = n$).

number of blocks is $n_b = \tau_{\text{run}}/\tau_b$. The average \mathcal{A} is calculated for each block

$$\langle \mathcal{A} \rangle_b = \frac{1}{\tau_b} \sum_{\tau=1}^{\tau_b} \mathcal{A}(\tau), \quad (3.24)$$

where the sum runs over configurations in block b only. The variance of the block average values $\langle \mathcal{A} \rangle_b$ is estimated by

$$\sigma^2(\langle \mathcal{A} \rangle_b) = \frac{1}{n_b} \sum_{b=1}^{n_b} (\langle \mathcal{A} \rangle_b - \langle \mathcal{A} \rangle_{\text{run}})^2. \quad (3.25)$$

At large τ_b , when the blocks become large enough to be statistically uncorrelated this quantity is expected to be inversely proportional to τ_b . Then, the statistical inefficiency s_{ineff} is defined as

$$s_{\text{ineff}} = \lim_{\tau_b \rightarrow \infty} \frac{\tau_b \sigma^2(\langle \mathcal{A} \rangle_b)}{\sigma^2(\mathcal{A})}. \quad (3.26)$$

It is the limiting ratio of the observed variance of an average to the limit expected on the assumption of uncorrelated Gaussian statistics. For quantities whose autocorrelation function shows an exponential decay, it can be shown that after equilibration, for large τ_{run} and $\delta t \ll \tau_m$,

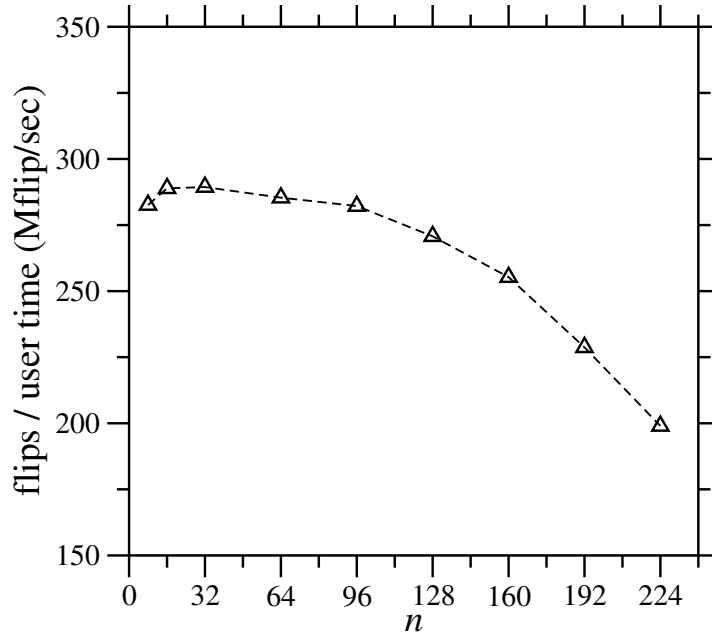


Figure 3.8: Parallel computing: Flips/user time vs. number of processors n for a PEL brush system having $M = 36$ chains of length $N = 30$ at grafting density $\rho_a \sigma^2 = 0.063$ and salt concentration $c_s \sigma^3 = 0.014$ following a Newtonian trajectory ($\lambda_B = \sigma, f = 1$).

the statistical inefficiency is

$$s_{\text{ineff}} \approx \frac{2\tau_m}{\delta t}. \quad (3.27)$$

Therefore the appropriate sampling interval for getting independent samples are approximately twice the correlation time.

3.2.4 Parallel computing

The sequential version of the molecular dynamics code with MMM2D implementation for evaluating the long-range Coulomb interaction ran on local compute servers with Alpha EV67/667 and Intel Xeon/3.06 processors. For using the IBM Regatta supercomputer at Juelich, the molecular dynamics code was parallelized by means of a self-scheduling (master-slave) algorithm [104, 157] for the force loop.

In order to obtain the efficiency of the parallel code for different processor numbers n , speedup vs. number of processors is plotted in Figure 3.7. In parallel computing, speedup defined as $\frac{t_1}{t_n}$ refers to how much a parallel algorithm is faster than a corresponding sequential algorithm, where t_1 is the execution time of the sequential algorithm (actually the sequential algorithm is parallel with 2 processors, one slave processor plus the master processor) and t_n is the execution time of the parallel algorithm with n processors. Also, plotted in Figure 3.8

is the flips/user time against n . This gives the number of arithmetic operations done by CPU per user time (time in the user mode). However, this is to be differentiated from flip rate which gives the number of arithmetic operations done by CPU per wall clock time (time in the system mode) which include overheads. The Hardware Performance Monitor (HPM) toolkit is available for performance measurement of applications running on IBM systems supporting the following processors and operating systems: Power3 and Power4 with AIX 5L and AIX 4.3.3. An utility (hpmcount) from the HPM toolkit, which starts an application and provides at the end of execution wall clock time, hardware performance counters information, derived hardware metrics, and resource utilization statistics. The hardware counters on the Power4 considers an arithmetic operation, an float-multiply-add (fma) operation and a floating point store (fst) as a single floating point operation. Therefore, a flip \equiv fpu0 + fpu1 + fma - fst.

Comparing the two figures, Figure 3.7 and Figure 3.8, we find that the efficiency is optimal in the range of $n = 64$ to $n = 128$ processors, where an efficiency of over 90% is reached (the speedup for $n = 128$ processors is $0.90 \times 128 = 115$). Lower numbers of processors lead to a loss in efficiency due to the idle master processor, while large processor numbers are less efficient because communication time becomes a dominant contribution. For larger number of processors, $n > 128$, the flip rate is comparatively less, however it remains almost constant below $n = 128$.

Chapter 4

Behavior of PEL brushes in the nonlinear osmotic regime

In this chapter molecular dynamics simulation results [10] on PEL brushes (with no added salt) in the nonlinear osmotic brush regime are discussed. The Bjerrum length is set $\lambda_B = \sigma$, and results are obtained for completely charged brushes ($f = 1$) with $M = 36$ chains of length $N = 30$, at five different anchoring densities $\rho_a \sigma^2 = 0.020, 0.042, 0.0625, 0.094,$ and 0.120 (which are comparable to experimental systems).

4.1 Height of the brush

Figure 4.1 shows snapshots from the equilibrium trajectories of completely charged brushes at five different anchoring densities considered in the study. In this representation, the connectivity of chains has been preserved, such that chains may extend beyond the simulation box. Counterions are assigned to the closest chain monomer. Considering the snapshots two points are addressed: (i) Immediately one can realize that the chains become strongly stretched and aligned perpendicular to the grafting surface. (ii) As expected from the estimation of the Gouy-Chapman length (see eqn. 2.88), in the case of completely charged brushes almost all the counterions remain trapped inside the brush. Both features will be quantitatively discussed below.

For completely charged brushes, Figure 4.2 gives the monomer density $\rho_m(z)$ (and counterion density) as a function of the distance from the grafting surface. $\rho_m(z)$ is normalized such that $\int_0^\infty dz \rho_m(z) = N \rho_a$. As seen, both monomers and counterions follow very similar nearly steplike profiles. Remember that, for the collapsed regime, obtained in the strong coupling limit, the monomer density becomes independent of anchoring density (see eqn. 2.96) resulting in a linear scaling of brush height with anchoring density [93, 104]. Obviously, at $\lambda_B = \sigma$ there remain no reminiscences of such a behavior. The extension in brushes is substantially increased and its dependence on anchoring density becomes much weaker (see below). The

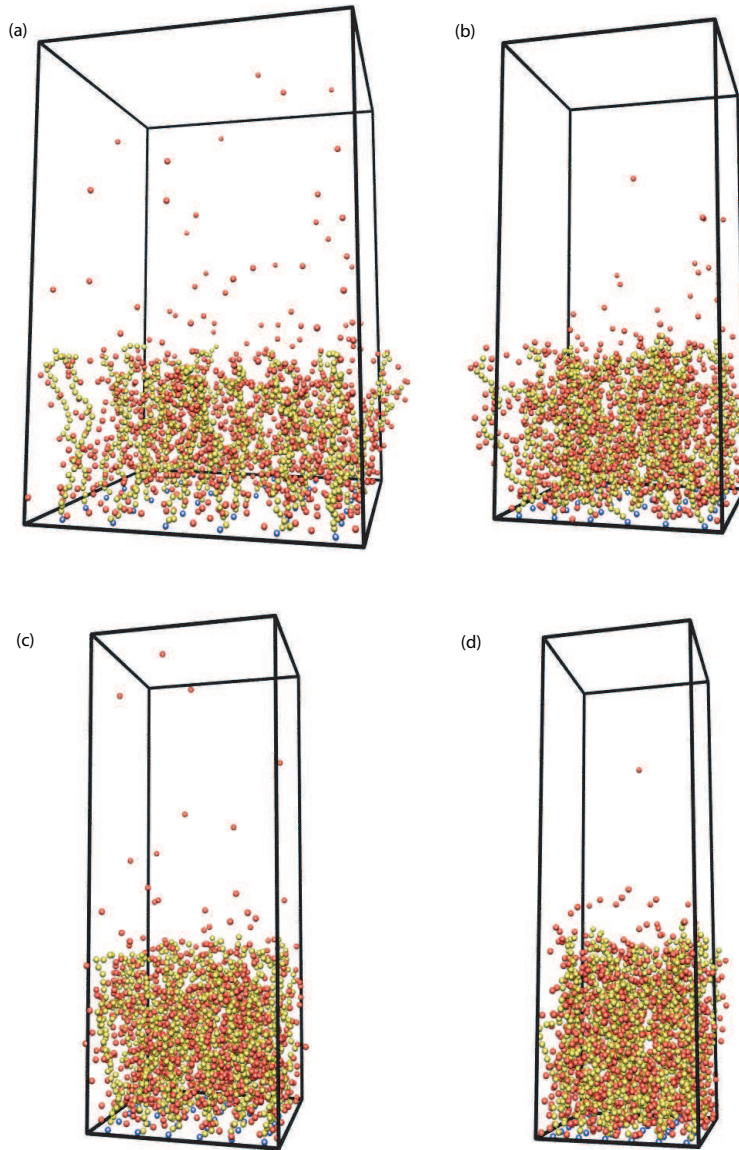


Figure 4.1: Polyelectrolyte brushes with $M = 36$ chains of length $N = 30$, completely charged at grafting density (a) $\rho_a \sigma^2 = 0.020$; (b) $\rho_a \sigma^2 = 0.042$; (c) $\rho_a \sigma^2 = 0.0625$; (d) $\rho_a \sigma^2 = 0.094$. The Bjerrum length is $\lambda_B = \sigma$. Counterions are assigned to the closest polyelectrolyte chain; polyelectrolyte chains are light yellow, counterions are red, and anchor monomers are blue. The box height perpendicular to the grafting surface has been reduced for the sake of representation. Snapshots have been represented by using the visualization program VMD [159].

average thickness of the brush and of the counterion layer is measured by taking the first

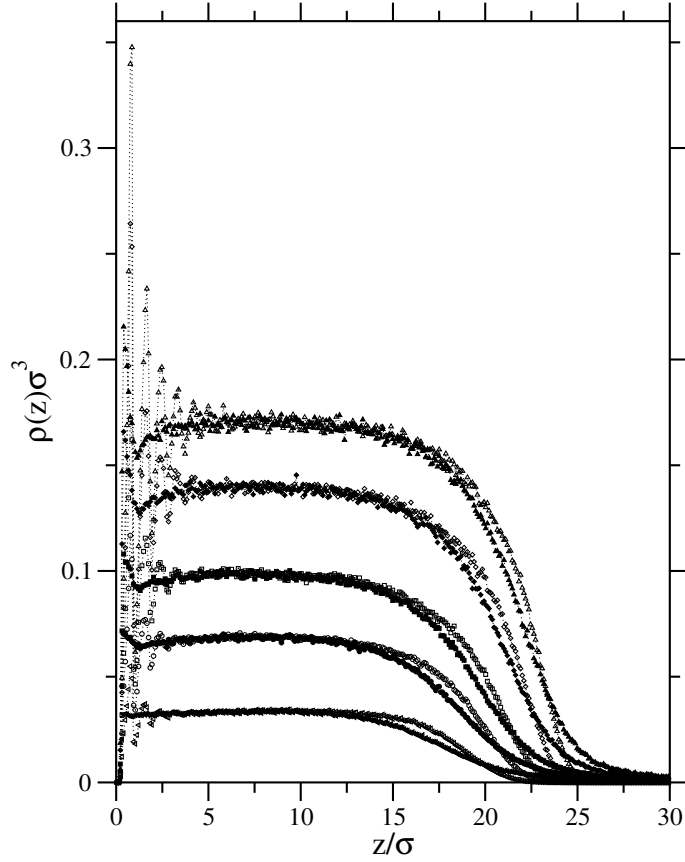


Figure 4.2: Simulated density profiles of monomers $\rho_m(z)$ (open symbols) and counterions $\rho_{ci}(z)$ (filled symbols) as a function of the distance from the grafting surface. Shown are profiles for fully charged brushes of 36 chains of $N = 30$ monomers with $\lambda_B = \sigma$ at anchoring densities (from bottom to top) $\rho_a\sigma^2 = 0.020$ (triangles left), 0.042 (circles), 0.0625 (squares), 0.094 (diamonds), and 0.120 (triangles up).

moments of the corresponding density profiles

$$\langle z_m \rangle = \frac{\int_0^\infty z \rho_m(z) dz}{\int_0^\infty \rho_m(z) dz}, \quad \langle z_{ci} \rangle = \frac{\int_0^\infty z \rho_{ci}(z) dz}{\int_0^\infty \rho_{ci}(z) dz}. \quad (4.1)$$

Note that a possible logarithmic divergence in the first moment of the counterion density at large λ_{GC} due to the $1/z^2$ - decay of $\rho_{ci}(z)$ is canceled by the finite size of the simulation box in the z -direction. The term neglected by closing the system is of the order of $A \log(L_z/\lambda_{GC})$ with a pre-factor $A \ll 1$. A systematic simulation study of the behavior of counterions at charged plates in both open and closed systems can be found in reference [163].

The average monomer and counterion heights for all systems studied with $\lambda_B = \sigma$, are given in Table 4.1. Figure 4.3 shows the plot of brush height $\langle z_m \rangle$, counterion height $\langle z_{ci} \rangle$, and brush

Table 4.1: Simulation results on completely charged PEL brushes ($f = 1$) for varying grafting density ρ_a : average brush height $\langle z_m \rangle$, average counterion height $\langle z_{ci} \rangle$, and average endpoint height $\langle z_e \rangle$ for $M = 36$ chains of length $N = 30$ at Bjerrum length $\lambda_B = \sigma \approx b$.

$\rho_a \sigma^2$	$\langle z_m \rangle / \sigma$	$\langle z_{ci} \rangle / \sigma$	$\langle z_e \rangle / \sigma$
0.020	9.29 ± 0.01	10.42 ± 0.01	17.20 ± 0.03
0.042	9.55 ± 0.01	10.32 ± 0.01	17.85 ± 0.03
0.0625	9.86 ± 0.01	10.51 ± 0.01	18.53 ± 0.03
0.094	10.39 ± 0.01	10.97 ± 0.02	19.67 ± 0.03
0.120	10.79 ± 0.01	11.34 ± 0.02	20.60 ± 0.03

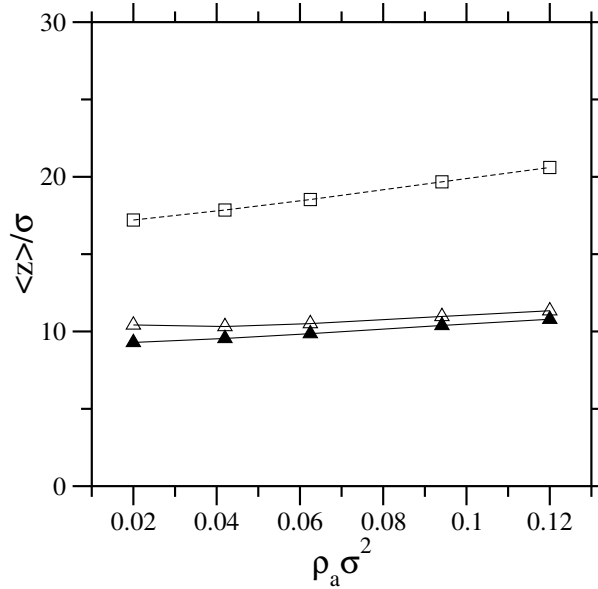


Figure 4.3: Average brush height $\langle z_m \rangle$ (filled triangles), average counterion height $\langle z_{ci} \rangle$ (triangles), and average brush endpoint height $\langle z_e \rangle$ (squares) of completely charged polyelectrolyte brushes with $M = 36$ chains of length $N = 30$ vs. anchoring density ρ_a . $\lambda_B = \sigma \approx b$. Error bars are smaller than symbol size.

endpoint height $\langle z_e \rangle$ for completely charged brushes at varying grafting density. Compared to the behavior obtained at strong coupling [104] the relation between $\langle z_m \rangle$ and $\langle z_{ci} \rangle$ is not perceptibly changed showing that counterions are mostly confined inside the brush layer and that electroneutrality condition is satisfied locally. This is also evident in the snapshots shown in Figure 4.1. Also one may observe looking at endpoint heights given in Table 4.1 that the polyelectrolyte chains are stretched up to about 60% of their contour length ($N = 30$), and thus their elastic behavior is far beyond the linear regime, eqn. 2.23.

However, contrary to the well-known scaling law for charged brushes in the osmotic regime, eqn. 2.92, which predicts a thickness independent of the anchoring density, Figure 4.3 shows a weak, but non-negligible dependence on ρ_a which will be examined further below. It is known that a logarithmic dependence of the brush height on grafting density is produced by inhomogeneities of the counterion profile in the direction normal to the anchoring plane [92] which may be caused by diffusion of counterions outside the brush. However, from the above discussions it is clear that the percentage of counterions which diffuse outside is very small for the systems considered here and can be neglected. This behavior, meanwhile obtained also in experiments, can be explained using scaling arguments where the self volume of the polymers is taken into account [10]. Assuming a box model as described in the introduction (see section 2.2.2.1), let's continue here the scaling arguments using a free-volume approximation very much in the spirit of the van der Waals equation for the liquid-gas transition. The effective hard-core volume of a single polyelectrolyte chain v_{self} , reduces the free volume that is available for the counterions. This free volume theory therefore takes the hard-core interactions between the polymer monomers and the counterions into account in a nonlinear fashion and is valid even at large densities in the limit of close-packing. Compared to that, the excluded volume interaction between counterions is small since the monomers are more bulky than the counterions and therefore it is neglected. The nonlinear entropic free energy contribution of the counterions read

$$F_{\text{ion}} \simeq Nf\rho_a \left[\ln \left(\frac{Nf\rho_a}{H - \rho_a v_{\text{self}}} \right) - 1 \right], \quad (4.2)$$

where H is the counterion layer thickness (see Figure 2.6). In the limit of vanishing polymer excluded volume, $v_{\text{self}} \rightarrow 0$, one recovers the standard ideal entropy expression, eqn. 2.86. As the volume available for the counterions in the brush, which per polymer is just H/ρ_a , approaches the self volume of polymers, v_{self} , the free energy expression eqn. 4.2 diverges, which means the entropic prize for that scenario becomes infinitely large. The self volume of the polymers is roughly independent of the polymer brush height, and can be written in terms of the effective monomer hardcore diameter σ_{eff} and the polymer contour length Nb as $v_{\text{self}} = Nb\sigma_{\text{eff}}^2$, where σ_{eff} takes into account the monomer and counterion diameters. This leads to the final expression [10]

$$F_{\text{ion}} \simeq Nf\rho_a \left[\ln \left(\frac{Nf\rho_a}{H - \rho_a \sigma_{\text{eff}}^2 Nb} \right) - 1 \right]. \quad (4.3)$$

Recall that the entropy of chain stretching was accounted for by linear elasticity theory, with a spring constant proportional to $1/R^2$, where R is the end-to-end distance of the polymer (see eqn. 2.22). However, from above discussions on chain stretching where it is observed that chains extend up to about 2/3 of their contour length, it is clear that the chains are in the strong stretching limit. For a freely jointed chain (our simulation model is supposed to mimic a freely jointed chain), the strong stretching entropy can be calculated exactly (see eqn. 2.26).

Writing down the free energy asymptotic expressions for the weak and strong stretching, one has

$$F_{\text{st}} \simeq \begin{cases} 3\rho_a h^2 / (2Nb^2), & \text{for } h \ll Nb, \\ -N\rho_a \ln(1 - h/Nb), & \text{for } h \approx Nb, \end{cases} \quad (4.4)$$

where h is the brush height (see Figure 2.6). Balancing eqn. 4.3 in the limit $\sigma_{\text{eff}} = 0$ and $H = h$, with the weak stretching term of the polymer elasticity ($h \ll Nb$) given in eqn. 4.4, the result is the standard osmotic brush regime [9,97]

$$h \simeq Nb \sqrt{\frac{f}{3}}. \quad (4.5)$$

The assumption that $H = h$ is verified to a great extent by looking at snapshots, Figure 4.1 or Figure 4.3, which shows that counterions have almost the same average height as chains for different anchoring densities. It is clear that for highly charged chains ($f = 1$), the predicted stretching in eqn. 4.5 goes beyond the assumption of weak stretching.

In the strongly stretched osmotic brush regime, one chooses the strong stretching analogue of eqn. 4.4 ($h \approx Nb$) and balances it with the counterion entropy eqn. 4.3 for vanishing polymer self volume $v_{\text{self}} = 0$ for the case $H = h$. The result is,

$$h \simeq Nb \frac{f}{1+f}, \quad (4.6)$$

which is the large stretching analogue of eq. (4.5). The maximal stretching predicted from this equation is 50% (for $f = 1$), which is considerably smaller than what is observed in simulations and experiments. Moreover the predicted brush height in eqn. 4.6 does not depend on the grafting density. This means that something is "missing" in the above scaling description. This something is proposed to be the increased entropic pressure, which is growing as the volume within the brush is progressively more filled up by the polymer self-volume. The fact that the nonlinear elastic stretching of the chains by itself does not lead to a grafting density dependence for the brush height has also been noted in previous studies [132].

Combining the high stretching (nonlinear) version of the chain elasticity, eqn. 4.4, with the nonlinear entropic effects of the counterions due to the finite volume of the polymer chains, i.e., choosing a finite σ_{eff} in eqn. 4.3, in the so-called nonlinear osmotic brush regime the brush height is

$$h \simeq Nb \frac{f + \sigma_{\text{eff}}^2 \rho_a}{1+f}, \quad (4.7)$$

which in the limit of maximal grafting density, i.e., close packing $\rho_a = 1/\sigma_{\text{eff}}^2$, reaches the maximal value $h = Nb$, as one would expect (compressing the brush laterally increase the vertical height and finally leads to a total extended structure). In Figure 4.4, we compare the prediction given by eqn. 4.7, shown as a solid line, with simulation results for the brush height

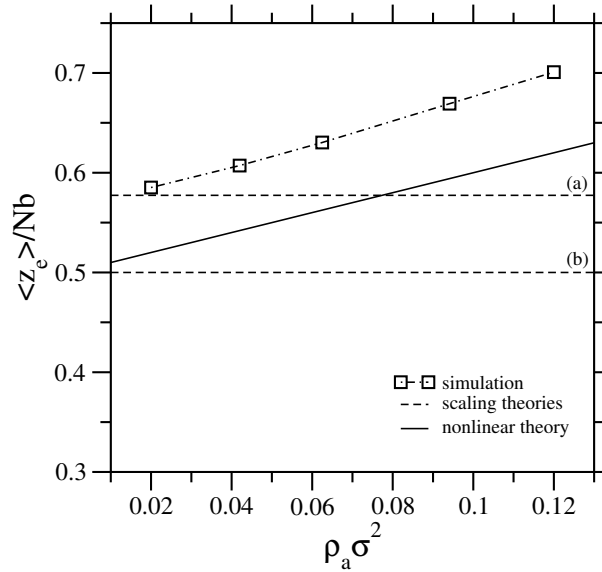


Figure 4.4: Brush height $\langle z_e \rangle$ as a function of grafting density ρ_a for polyelectrolyte chains of $N = 30$ monomers of length $N = 30$ with charge fraction $f = 1$. Symbols show simulation data with the corresponding linear fit (dot-dashed line), the solid line represents the prediction of the nonlinear scaling theory, eq. (4.7), with $\sigma_{\text{eff}}^2 = 2\sigma^2$. The dashed lines (a) and (b) show the scaling predictions eq. (4.5) and eq. (4.6), respectively.

as a function of grafting density. Note that we have used

$$\sigma_{\text{eff}}^2 = 2\sigma^2 \quad (4.8)$$

where $\sigma = \sigma_m = \sigma_{ci}$ is the Lennard-Jones diameter of monomers and counterions in the simulations. This choice corresponds to an approximate 2D square-lattice packing of monomers and counterions on two interpenetrating sublattices. The scaling prediction, eqn. 4.7, qualitatively captures the slow increase of the brush height with grafting density. The deviations from the simulation data may be explained by considering additional effects, such as lateral inhomogeneity of counterion distribution around the brush chains (see below) and intermediate stretching elasticity of the chains. Also, the simulation is not dealing with hard spheres but with soft potentials, which will modify the ratio $\sigma_{\text{eff}}/\sigma$.

However, note that the above weak dependence of the brush height on grafting density can also be reproduced by taking into account both nonlinear elasticity of the chains and lateral inhomogeneity of the counterion distribution [94]. All the previous theoretical studies of polyelectrolyte brushes were restricted by two major approximations. First, the counterion distribution was assumed uniform in lateral direction parallel to the grafting plane. However, inhomogeneous distributions were obtained both in simulation [104] and experiment [112].

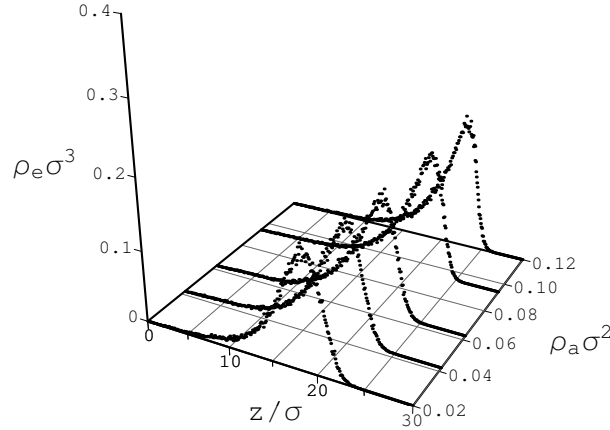


Figure 4.5: Endpoint distributions of completely charged polyelectrolyte brushes at $\lambda_B = \sigma$. Grafting densities are the same as in Figure 4.2.

Secondly, in most of the theories Gaussian elasticity is used for the mechanical stretching of chains which is hardly true in strongly stretched brush states. In the model used by Naji *et al.* [94] the electrostatic free energy is evaluated within the cylinder model by means of nonlinear Poisson-Boltzmann theory. The elastic free energy of the chains is treated using a freely jointed chain model (as discussed above) and the short-range volume interaction is included by imposing a constant volume constraint for the polyelectrolyte. Doing so, reasonable agreement between simulation data and theoretical predictions has been obtained without any fitting parameter in the nonlinear osmotic brush regime.

Figure 4.5 gives the endpoint distribution $\rho_e(z)$ for $M = 36$ chains of length $N = 30$, normalized to unity. One notes that, for all grafting densities ρ_a , the endpoint distribution exhibits a pronounced peak at large z and decays strongly inside the brush. These features reflect the highly ordered brush state due to strong stretching perpendicular to the grafting surface. The behavior is in contrast to that found in the collapsed brush regime at low grafting densities [104], where a second peak of the endpoint distribution was obtained at small z , indicating that the chains are likely to fold back onto the surface. Thus, the average end point height $\langle z_e \rangle$ is a good measure of the brush height and the above box model is a reasonable approximation. The average endpoint height is also given in Table 4.1. Note that $\langle z_e \rangle$ is less reliable than $\langle z_m \rangle$ because of the reduced statistical significance (of the order N per data collection) and because of higher sensitivity to finite size effects [104].

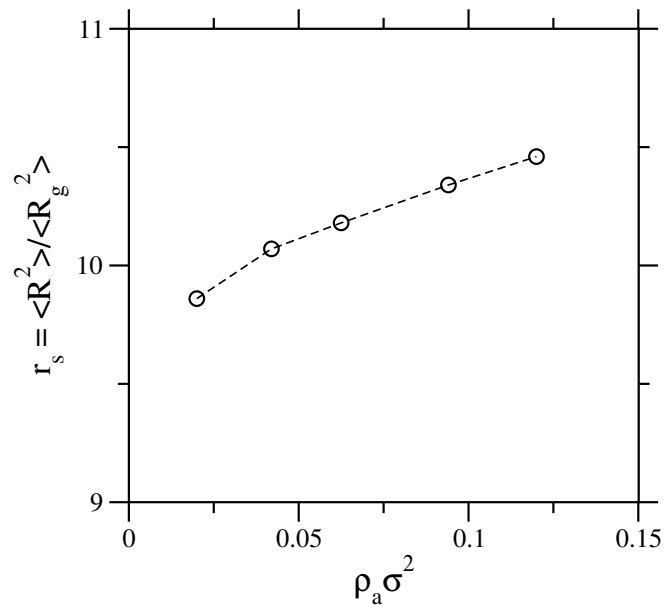


Figure 4.6: Shape factor $r_s = \langle R^2 \rangle / \langle R_g^2 \rangle$ for systems with $M = 36$ chains of length $N = 30$ as a function of grafting density. Error bars are less than 0.3 unit.

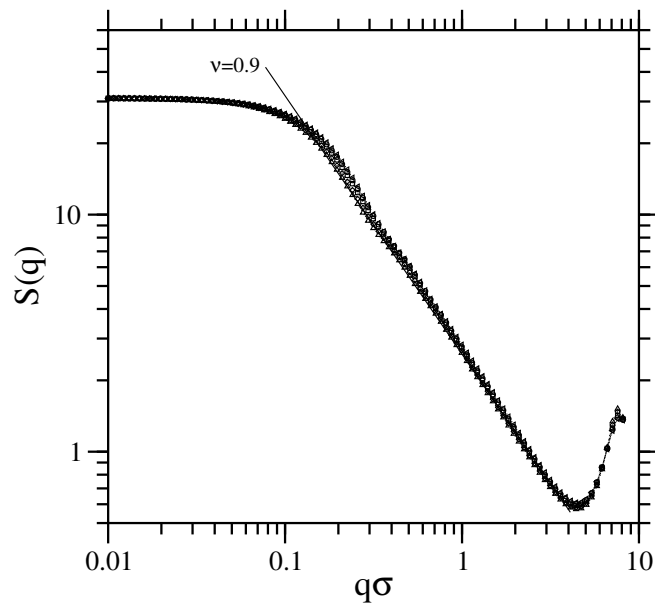


Figure 4.7: Spherically averaged structure factor $S(q)$ for different grafting densities ρ_a . The solid line indicates scaling for $\nu = 0.9$. Symbols as in Figure 4.2.

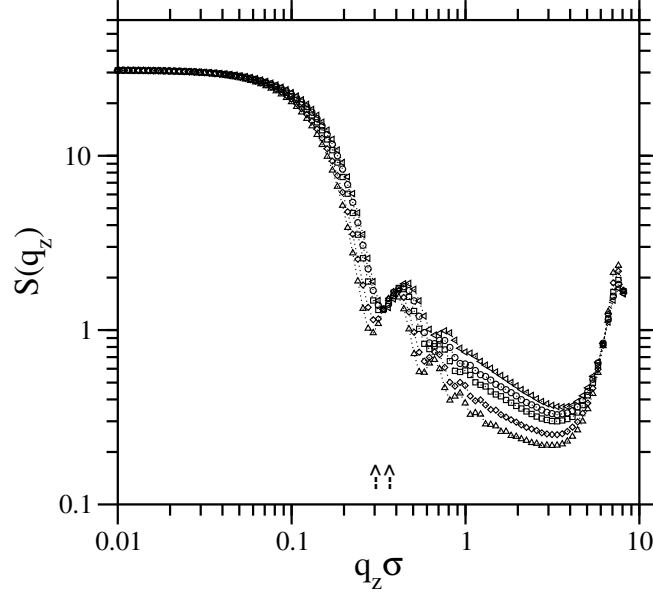


Figure 4.8: Structure factor $S(q_z)$ perpendicular to the grafting plane for different grafting densities ρ_a . Symbols as in Figure 4.2. Region between the arrows indicate small dips at $q_z^* = 2\pi/\langle z_e \rangle$ for varying anchoring densities from $\rho_a \sigma^2 = 0.020$ (right arrow) to 0.120 (left arrow).

4.2 Chain Structure

The overall shape of the grafted polyelectrolyte can be described by the stretching ratio $r_s = \langle R^2 \rangle / \langle R_G^2 \rangle$ (see eqn. 2.35), where $\langle R^2 \rangle$ is the average square end-to-end distance and $\langle R_G^2 \rangle$ is the average radius of gyration squared. For a free Gaussian chain, one finds $r_s = 6$, and a rigid rod has the stretching ratio $r_s = 12$. For an isolated end-grafted neutral chain, a stretching ratio $r_s = 6.94$ has been obtained [104]. As shown in Figure 4.6 the ratio r_s is sensitive to the grafting density of the brush, but less compared to the collapsed brush regime [104]. At all grafting densities, values typical of strongly stretched chains are obtained, in agreement with the high stretching assumption for the elasticity of chains as discussed in section 4.1. Lowering the grafting density the chain extension is reduced, however.

For a more detailed examination of the intra-chain structure of grafted polyelectrolytes at all length scales, the single chain structure factor is studied. Here we consider the spherically averaged one (see eqn. 2.36)

$$S(q) = \left\langle \left\langle \frac{1}{N+1} \left| \sum_{j=0}^N \exp(i\mathbf{q} \cdot \mathbf{r}_j) \right|^2 \right\rangle_{|\mathbf{q}|} \right\rangle \quad (4.9)$$

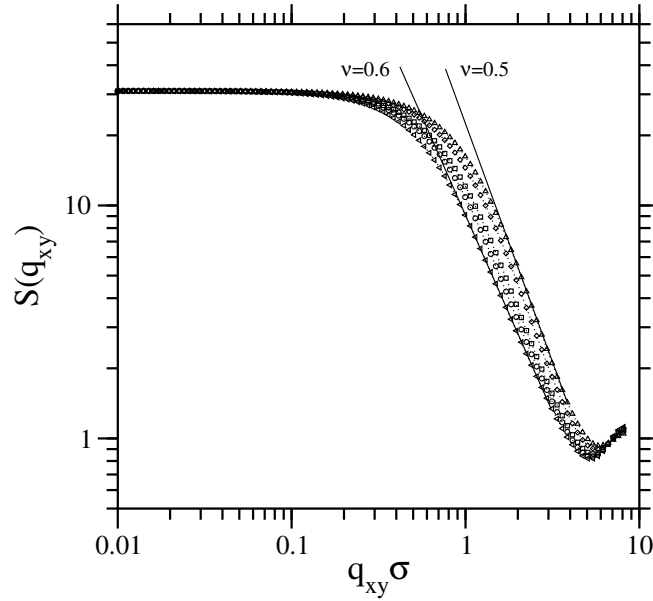


Figure 4.9: In-plane averaged structure factor $S(q_{xy})$ for different grafting densities ρ_a . The solid lines indicate scaling for $\nu = 0.5$ and 0.6 . Symbols as in Figure 4.2.

as well as the structure factor in transverse direction $S(q_z)$ and the in-plane averaged one $S(q_{xy})$. In analogy to free chains, in the asymptotic regime $2\pi/R \ll q \ll \pi/b$ (Porod region), the structure factor is expected to obey the scaling relation $S(q) \sim q^{-1/\nu}$ (see eqn. 2.57) where ν is the exponent of the N dependence of the chain radius $R \sim N^\nu$. Figure 4.7 gives the spherically averaged structure factor. Within the range of anchoring densities studied in simulations, the spherically averaged structure factor $S(q)$ is almost not changed, reflecting strong stretching with a exponent $\nu \approx 0.9$. This result is consistent with the structure perpendicular to the grafting plane, shown by $S(q_z)$ in Figure 4.8. In analogy to the oscillations of $S(q_z)$ of a rigid rod oriented perpendicular to the grafting surface, the structure factor exhibits strong features of a rigid-rod like behavior amplified with increasing anchoring density. The small dips in the low q -regime agree well (to within 10%) with the average endpoint position $\langle z_e \rangle$ (indicated by arrows). Note that a highly ordered layering evolves close to the grafting surface. The transverse monomer profiles shown in Figure 4.2 indicate short-range ordering in a stack ranging from three up to seven layers above the grafting surface.

The most interesting additional information gives the in-plane averaged structure factor $S(q_{xy})$ shown in Figure 4.9. Note that the in-plane behavior of the grafted polyelectrolyte chains is determined by the properties of the underlying neutral chains. In agreement with our model, which is supposed to mimic polyelectrolytes under good-solvent conditions, at low grafting densities $S(q_{xy})$ gives an in-plane scaling $R_{xy} \sim N^{0.6}$. At large ρ_a , however, $S(q_{xy})$ indicates $R_{xy} \sim N^{0.5}$, i.e., the scaling behavior of a Gaussian chain well-known for chains in

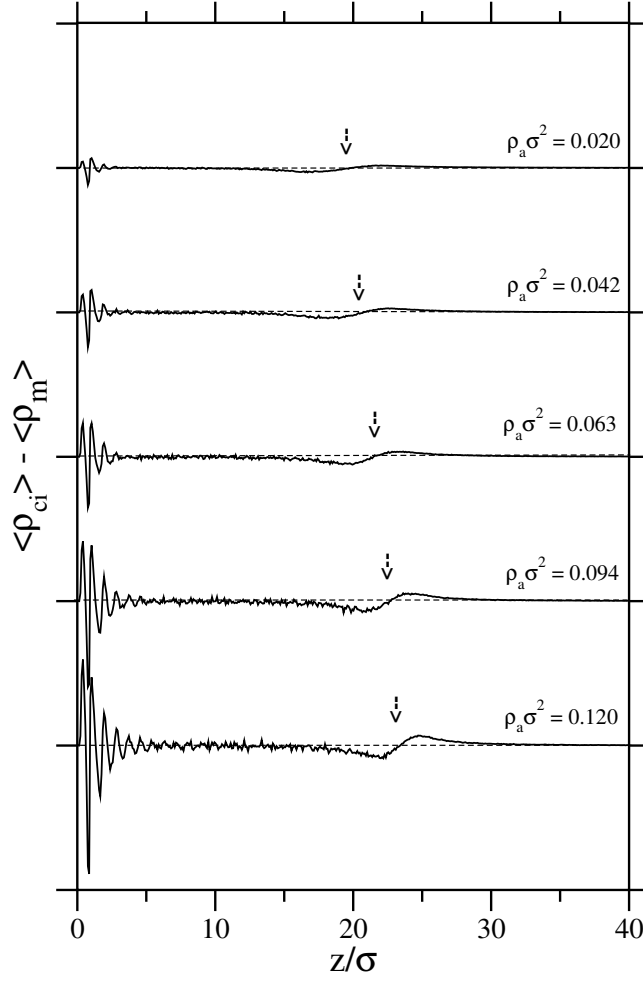


Figure 4.10: Local net brush charge $\langle \rho_{ci} \rangle - \langle \rho_m \rangle$ as a function of the distance from the grafting surface, z . Shown are systems of 36 chains of length 30 where each zero line (dashed lines) is shifted by 0.2 units in y -direction for each grafting density. The average endpoint height $\langle z_e \rangle$ is indicated by an arrow. Monomers carry a negative, counterions a positive unit charge.

melt.

Thus, for varying grafting densities the chain structure of grafted polyelectrolytes remain almost strongly stretched.

4.3 Local net charge and counterion distribution

The local net charge is shown in Figure 4.10, where we have assigned positive charges to counterions and negative charges to monomers, respectively. Charge neutrality is not only satisfied globally ($\int_0^\infty dz \langle \rho_{ci} - \rho_m \rangle = 0$), but also to a good approximation at the local level

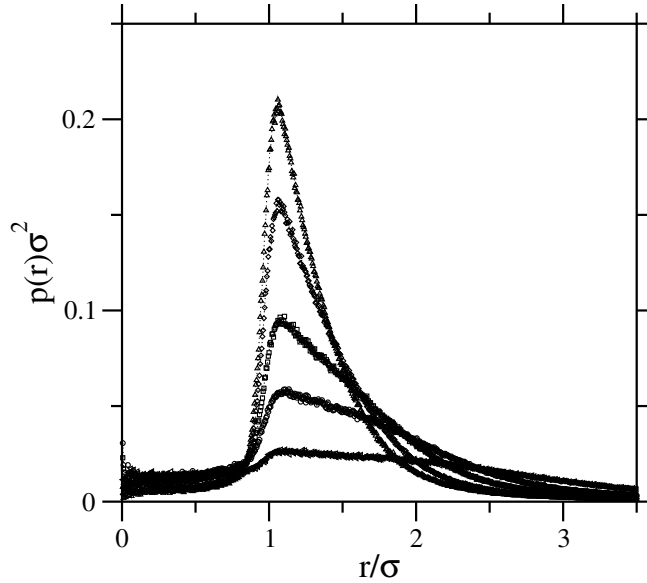


Figure 4.11: Ion-polyelectrolyte distribution function for completely charged chains at $\lambda_B = \sigma$. Grafting densities and symbols are the same as in Figure 4.2.

which is in agreement with the assumptions used in section 4.1. At low grafting density, a small tail of positive charge develops at the outer edge of the brush which is enhanced as the grafting density is increased. This can be explained as a consequence of simple packing effect while the brush is being compressed laterally. These dipoles located at the rim of the brush might influence interactions between charged brushes. The fluctuations at small z are a consequence of the layering of the monomers close to the surface. Larger fluctuations at higher grafting densities are a consequence of the histogram construction because a constant binning interval for all grafting values was used.

In references [93, 104] it has been shown that the particular behavior of polyelectrolyte brushes in the strong coupling limit, i.e. the existence of a collapsed regime, is caused by Coulomb correlations (see also section 2.2.2.1). To discuss the role of correlations and the degree of counterion condensation, the ion-polyelectrolyte distribution function $p(r)$ is plotted in Figure 4.11, where r is the separation between counterion center and closest polyelectrolyte bond. The distribution $p(r)$ is normalized according to $2\pi \int_0^\infty r p(r) dr = 1$. For strong Coulomb interaction, distribution functions show a pronounced peak at $r = \sigma$ [104]. As the coupling is reduced, at $\lambda_B = \sigma$, the peak is much weaker and the probability remains finite up to larger distances (see Figure 4.11). There is still another remarkable difference between the two situations: At strong interaction strength the lowest anchoring density shows the highest peak value. This can be understood due to the decreasing effective line charge density

$N/2\langle z_m \rangle$ with increasing stretching of the chain, i.e. with increasing anchoring density. Thus, the effective Manning ratio $\xi_{\text{eff}} = N\lambda_B/2\langle z_m \rangle$ exhibits its largest value at the lowest anchoring density, giving rise for a large fraction of 'condensed' counterions [104]. On the other hand at weak interaction, Figure 4.11 shows that the peak becomes monotonously enhanced with growing anchoring density which is probably a simple packing effect. Note that a simple estimation of the degree of condensed counterions by assuming them to be condensed if they are closer than λ_B yields $f_{\text{eff}} > 0.98$ although the fraction of condensed counterions is slightly growing with increasing grafting density. Thus, for an osmotic brush it is reasonable that the counterion osmotic pressure has a play in chain stretching.

Chapter 5

PEL brushes with added salt

In this chapter, results of extensive molecular dynamics simulations [106] on PEL brushes with added salt in the nonlinear osmotic brush regime (Bjerrum length is set, $\lambda_B = \sigma$) are reported. The results obtained are for completely charged brushes ($f = 1$) at two different anchoring densities $\rho_a = 0.042\sigma^{-2}$ and $0.094\sigma^{-2}$, respectively, with $M = 36$ chains of length $N = 30$. Note that these simulations are computationally rather expensive: Typically depending on the number of charges treated, one data point on IBM Power4+, 1.7 GHz supercomputer (massively parallel with 64 CPUs) takes between two to ten days, while on sequential Alpha EV67/667 or Intel Xeon/3.06 processors it takes roughly from couple of weeks to a month.

Previous simulation studies on PEL brushes in salt-free solution [104,105], have shown that varying the Bjerrum length λ_B , a non-monotonic behavior of the brush height is obtained. Figure 5.1 shows the plot of average height of chain ends $\langle z_e \rangle$, described in eqn. 4.1, against the Bjerrum length λ_B , both in the case with and without added salt, for a polyelectrolyte brush with completely charged chains of length $N = 30$. For the salt-less case, Figure 5.1 reproduces the previous result [105] which has been discussed already in section 2.2.2.1. When a finite concentration of salt is added to the system, there is indeed a reduced brush height observed in the nonlinear osmotic regime close to maximum stretching at $\lambda_B/b \approx 1$ which is consistent with the scaling analysis by Pincus (see section 2.2.2.2) where it is proposed that the Debye screening from the salt reduces the counterion osmotic pressure, which stretches the polymers obtaining the expression for the brush height h as

$$h \simeq Nb \left(\frac{\rho_a f^2}{bc_s} \right)^{1/3}, \quad (5.1)$$

where Nb is the contour length. This behavior will be discussed in detail below. In the collapsed regime at large Bjerrum lengths, added salt is expected to reduce the attractive interaction that causes chain collapse. Indeed we find that at $\lambda_B/b \gtrsim 9$ the brush becomes slightly swollen with additional salt.

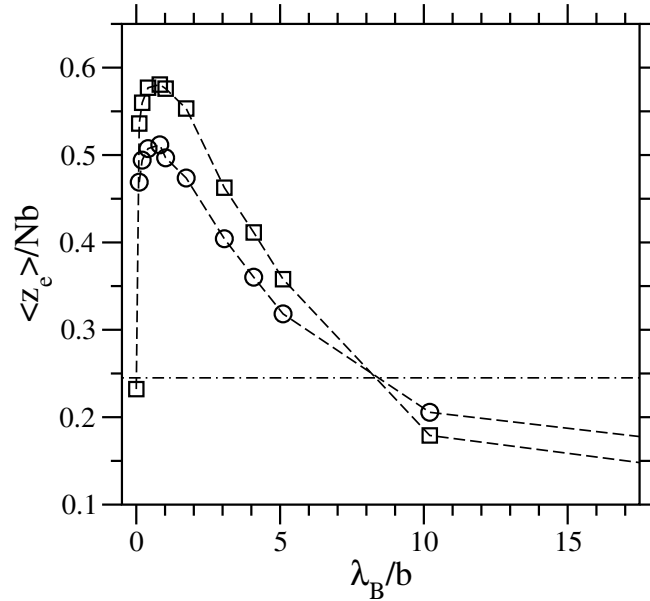


Figure 5.1: Average height of chain ends $\langle z_e \rangle$ for zero salt (squares) and with salt concentration $c_s \sigma^3 = 0.009$ (circles), both rescaled with the contour length Nb ($N = 30$), versus Bjerrum length λ_B at grafting density $\rho_a \sigma^2 = 0.02$. The dot-dashed line indicates $\langle z_e \rangle$ of an identical system of uncharged chains.

5.1 Height of the brush

Figure 5.2 shows a snapshot from the equilibrium trajectory for brushes at $\rho_a = 0.094\sigma^{-2}$ with salt concentration $c_s = 0.110\sigma^{-3}$. In contrast to the salt-less case (compare Figure 4.1(d)), now the particle distribution looks rather homogeneous over the total height of the simulation box. Because in the present model polyelectrolyte counterions and salt counterions are considered to be identical they are subject to an unrestricted exchange. As one can see from the snapshot, salt coions are diffusing into the brush layer. Although it can not be seen directly in snapshots, due to local electroneutrality these coions are escorted by a corresponding number of counterions. The different aspects of the ion distribution inside and outside the brush layer will be discussed below in detail. The effect of added salt on the brush structure is shown in Figure 5.3. The monomer density $\rho_m(z)$ is plotted as a function of the distance from the grafting surface for the anchoring densities $\rho_a = 0.042\sigma^{-2}$ and $0.094\sigma^{-2}$. $\rho_m(z)$ is normalized such that $\int_0^\infty dz \rho_m(z) = N\rho_a$. From Figure 5.3, it is observed (i) that chain stretching is slightly reduced with growing salt concentration, and (ii) that the monomer density inside the brush is little increased with reduced stretching. These features are in agreement with the brush behavior in the nonlinear osmotic regime (see chapter 4). Note that the step-like shape of the density profiles becomes less pronounced with increasing salt, in particular for small

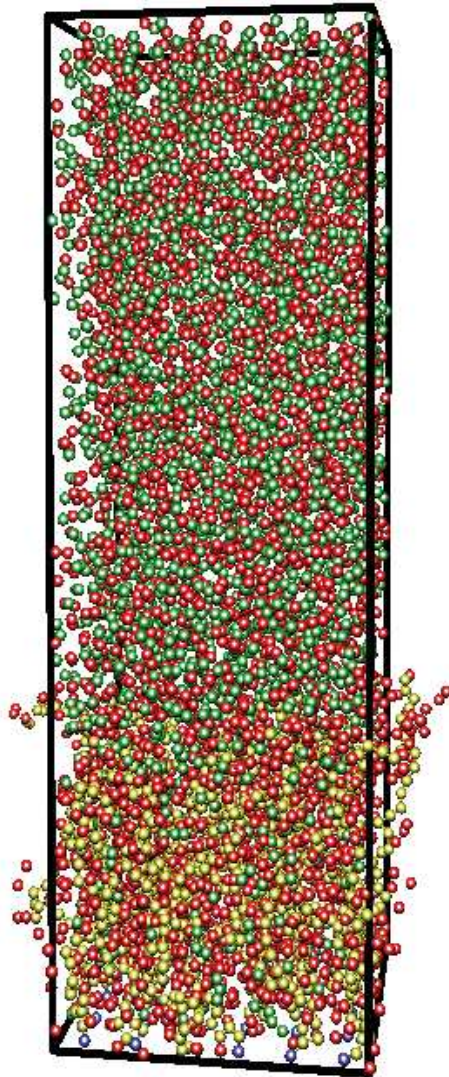


Figure 5.2: Polyelectrolyte brush with $M = 36$ chains of length $N = 30$, completely charged at grafting density $\rho_a \sigma^2 = 0.094$ with a salt concentration $c_s = 0.110 \sigma^{-3}$ ($\lambda_B = \sigma$). Counterions in the brush are assigned to the closest chain monomer; polyelectrolyte chains are yellow, counterions and salt ions being oppositely charged as monomers are red, likely charged salt ions are green, and anchor monomers are blue. The box height perpendicular to the grafting surface is $L_z = 2N\sigma$. The snapshot out of an equilibrium trajectory has been represented by using the visualization program VMD. [159]

grafting density.

The average thickness of the brush is measured by taking the first moment of the monomer density profile (see eqn. 4.1). The average monomer height for the systems considered in the

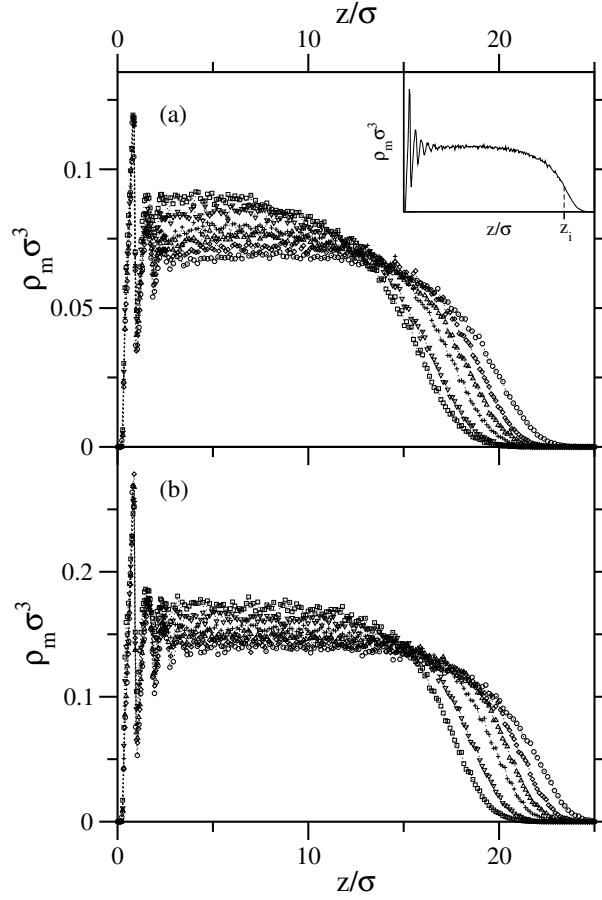


Figure 5.3: Monomer density profiles $\rho_m(z)$ of completely charged polyelectrolyte brushes ($N = 30, \lambda_B = \sigma$) as a function of the distance from the grafting surface: (a) at grafting density $\rho_a \sigma^2 = 0.042$ and varying salt concentration ($c_s \sigma^3 = 0$ (circles), 0.007 (diamonds), 0.014 (triangles up), 0.021 (plus), 0.035 (triangles down), 0.049 (squares)); (b) at grafting density $\rho_a \sigma^2 = 0.094$ ($c_s \sigma^3 = 0$ (circles), 0.016 (diamonds), 0.031 (triangles up), 0.047 (plus), 0.078 (triangles down), 0.110 (squares)). The inset shows schematically the estimation of inflection point z_i .

present study (varying grafting density and salt concentration) are given in Table 5.1. For highly charged and densely tethered polyelectrolyte brushes, the mean-field scaling theories distinguish two different regimes depending on the ionic strength in the solution: the osmotic brush and the salted brush regimes [97]. In the osmotic brush regime, the concentration of counterions inside the brush is greater than external salt concentration in solution, i.e., $c_{ci} \gg c_s$; thus, stretching is produced by the osmotic pressure of the confined counterions. In this regime, the stretching forces resisted by the elastic force, balances the counterion osmotic pressure, modeled as an ideal gas of counterions. The resulting brush height is (see scaling discussions in section 2.2.2.1) [9]

$$h_0 \simeq N b f^{1/2}. \quad (5.2)$$

Table 5.1: Simulation results on completely charged polyelectrolyte brushes with varying salt concentration c_s ($\lambda_B = \sigma \approx b$): average brush height $\langle z_m \rangle$, average endpoint height $\langle z_e \rangle$, position of inflection point z_i , ion concentration inside the brush c''_{si} and buffer concentration c'_{si} at two different grafting density ρ_a .

$\rho_a \sigma^2$	$c_s \sigma^3$	$\langle z_m \rangle / \sigma$	$\langle z_e \rangle / \sigma$	z_i / σ	$c''_{si} \sigma^3$	$c'_{si} \sigma^3$
0.042 ^a	0	9.55 ± 0.01	17.85 ± 0.03	20.5	0.059	0
0.042 ^a	0.007	9.18 ± 0.01	16.98 ± 0.04	19.3	0.064	0.018
0.042 ^a	0.014	8.88 ± 0.01	16.31 ± 0.04	18.4	0.072	0.034
0.042 ^a	0.019	8.65 ± 0.01	15.72 ± 0.05	17.8	0.077	0.045
0.042 ^a	0.028	8.30 ± 0.01	14.94 ± 0.03	16.7	0.088	0.066
0.042 ^a	0.033	8.20 ± 0.01	14.83 ± 0.04	16.2	0.094	0.076
0.042 ^b	0.007	9.15 ± 0.01	16.92 ± 0.04	19.2	0.065	0.021
0.042 ^b	0.014	8.78 ± 0.01	15.97 ± 0.04	18.5	0.073	0.039
0.042 ^b	0.021	8.46 ± 0.01	15.27 ± 0.04	17.8	0.081	0.055
0.042 ^b	0.028	8.27 ± 0.01	14.78 ± 0.03	17.0	0.091	0.072
0.042 ^b	0.035	7.98 ± 0.01	14.20 ± 0.04	16.2	0.101	0.087
0.042 ^b	0.042	7.76 ± 0.01	13.65 ± 0.04	15.8	0.111	0.103
0.042 ^b	0.049	7.63 ± 0.01	13.47 ± 0.05	15.7	0.122	0.118
0.042 ^b	0.063	7.43 ± 0.01	12.91 ± 0.05	14.8	0.142	0.149
0.094 ^a	0	10.40 ± 0.01	19.72 ± 0.02	22.5	0.122	0
0.094 ^a	0.016	10.16 ± 0.01	19.21 ± 0.03	21.5	0.129	0.042
0.094 ^a	0.031	9.88 ± 0.01	18.57 ± 0.03	20.5	0.138	0.081
0.094 ^a	0.042	9.73 ± 0.01	18.25 ± 0.03	20.0	0.147	0.106
0.094 ^a	0.063	9.30 ± 0.01	17.28 ± 0.03	19.0	0.164	0.155
0.094 ^a	0.073	9.13 ± 0.01	16.95 ± 0.03	18.5	0.174	0.179
0.094 ^b	0.016	10.05 ± 0.01	18.96 ± 0.03	21.4	0.131	0.049
0.094 ^b	0.031	9.78 ± 0.01	18.33 ± 0.03	20.3	0.142	0.093
0.094 ^b	0.047	9.44 ± 0.01	17.56 ± 0.03	19.7	0.155	0.135
0.094 ^b	0.063	9.12 ± 0.01	16.90 ± 0.03	18.7	0.170	0.173
0.094 ^b	0.078	8.91 ± 0.01	16.41 ± 0.03	18.3	0.189	0.211
0.094 ^b	0.091	8.73 ± 0.01	16.03 ± 0.03	18.0	0.206	0.239
0.094 ^b	0.110	8.47 ± 0.01	15.38 ± 0.03	17.5	0.231	0.281
0.094 ^b	0.141	7.95 ± 0.01	14.16 ± 0.03	16.5	0.272	0.351
0.094 ^b	0.173	7.62 ± 0.01	13.44 ± 0.03	16.0	0.323	0.417
0.094 ^b	0.188	7.54 ± 0.01	13.04 ± 0.03	15.7	0.346	0.451

^aheight of simulation box: $L_z = 3N\sigma$.

^bheight of simulation box: $L_z = 2N\sigma$.

When the external salt concentration is greater than the concentration of counterions inside the brush, i.e., $c_{ci} \ll c_s$ the salted brush regime is entered. The electrostatic interaction among chain segments becomes screened. The brush remains stretched by the excluded volume repul-

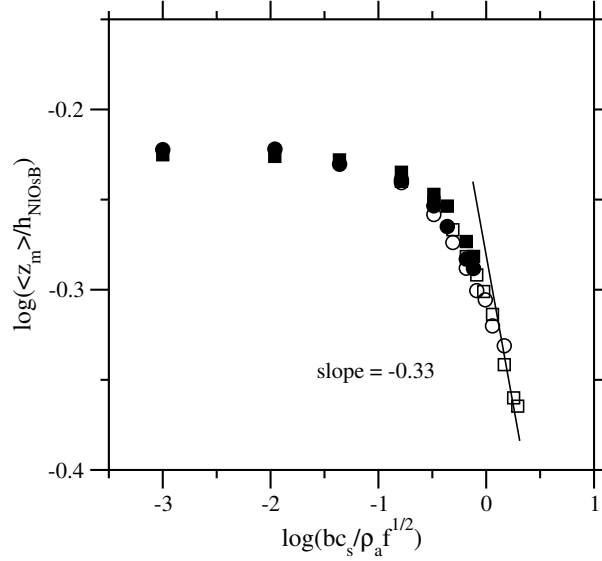


Figure 5.4: Salt concentration dependence of the brush height $\langle z_m \rangle$ ($\lambda_B = \sigma$, $f = 1$) as a master plot for two different grafting densities: $\rho_a = 0.042\sigma^{-2}$ (circles) and $0.094\sigma^{-2}$ (squares). Simulation results with $L_z = 2N\sigma$ (open symbols) and $3N\sigma$ (filled symbols). For the sake of representation, the asymptotic value at $c_s = 0$ is shown at $\log(bc_s/\rho_a) = -3$. ($\sigma_{\text{eff}}^2 = 2\sigma^2$, see text).

sion, where the chains may still be swollen locally (within a Debye length) by electrostatics. This can be modeled using an effective second virial coefficient ($v_{\text{eff}} \simeq f^2/c_s$). In this salted regime, balancing the chain elasticity with the excluded volume repulsion, the resulting brush height is eqn. 5.1 [9].

According to the predictions of eqns. 5.1 and 5.2, the brush height depends on four variables: the chain length N , fraction of free counterions f , anchoring density ρ_a , and salt concentration c_s . It is desirable to plot all the data in a master curve based on the scaling forms of eqns. 5.1 and 5.2, which takes all four parameters into consideration. Rewriting the brush height given in eqn. 5.1 in terms of h_0 one has

$$h \simeq h_0 \left(\frac{\rho_a f^{1/2}}{bc_s} \right)^{1/3}. \quad (5.3)$$

Thus the generic choice is to plot h/h_0 vs $bc_s/\rho_a f^{1/2}$ [119]. From the study of the salt-less case one knows, however, that there occurs also a weak dependence of brush height on grafting density in contrast to eqn. 5.2. Therefore to rescale the brush height with a salt-free value h_0 instead of the osmotic brush height given in 5.2 we use that of the nonlinear osmotic brush

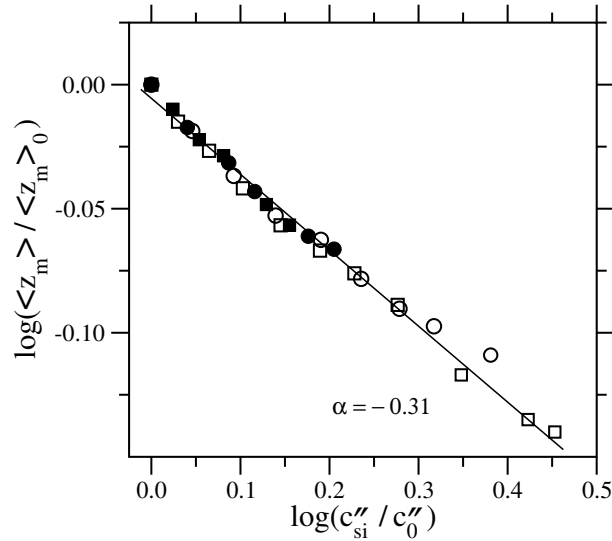


Figure 5.5: The average brush height $\langle z_m \rangle$ of completely charged polyelectrolyte brushes ($\lambda_B = \sigma$) versus the ion concentration inside the brush c_{si}'' (both variables rescaled with the corresponding salt-free values $\langle z_m \rangle_0$ and c_0'' respectively). Symbols are the same as in Figure 5.4. The solid line shows a power-law fit.

derived in the previous chapter (see eq. 4.7),

$$h_{\text{NIOsB}} \simeq Nb \frac{f + \sigma_{\text{eff}}^2 \rho_a}{1 + f}, \quad (5.4)$$

where the effective monomer hard-core diameter σ_{eff} takes into account the monomer and counter-/coion diameters. Figure 5.4 gives the plot for $h(c_s)/h_{\text{NIOsB}}$ vs $bc_s/(\rho_a f^{1/2})$. Here we used $\sigma_{\text{eff}}^2 = 2\sigma^2$ as with the salt-less case (see eqn. 4.8) [10]. Now, all data points fall indeed onto a universal curve in a log-log plot, which tends to a slope of zero in the low salt regime and a slope of $-1/3$ in the high salt regime. This supports on the one hand the validity of the asymptotic relation eqn. 5.4, for nonlinear osmotic brush, and on the other hand the validity of eqn. 5.1, for salted brush. Note that a simple estimation of the degree of condensed counterions by assuming them to be condensed if they are closer than λ_B yields $f_{\text{eff}} > 0.98$. That is why the fraction of free counterions is set $f = 1$ although the fraction of condensed counterions is slightly growing with increasing grafting density. Figure 5.4 shows, on the other hand, obviously not much simulation data points in the asymptotic limit of a salted brush, where the influence of counterions can be neglected. However, a further increase of the total number of charges would enlarge the CPU time beyond a reasonable limit and a reduced size of the simulation box would cause serious finite size effects. Therefore, to account properly for the screening within the brush, the counterion concentration c_{ci} cannot be neglected.

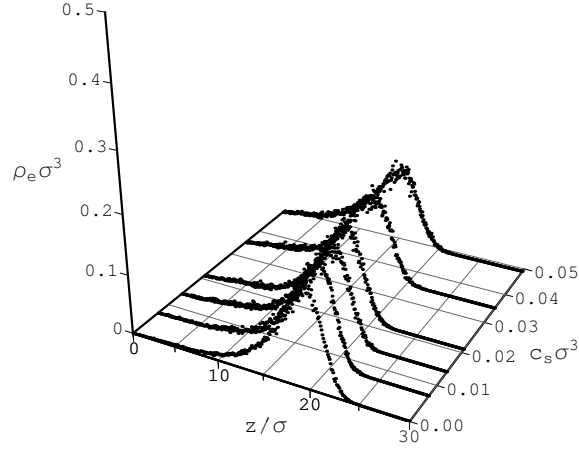


Figure 5.6: Endpoint distributions of completely charged polyelectrolyte brushes at grafting density $\rho_a = 0.042\sigma^{-2}$ ($\lambda_B = \sigma$) for varying salt.

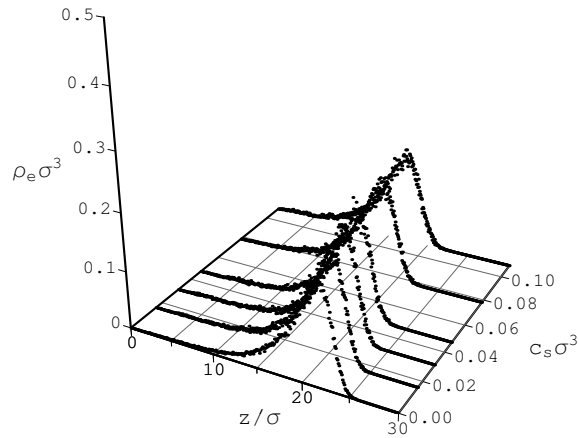


Figure 5.7: Endpoint distributions of completely charged polyelectrolyte brushes at grafting density $\rho_a = 0.094\sigma^{-2}$ ($\lambda_B = \sigma$) for varying salt.

To account for the concentration of mobile ions (chain counterions, salt counterions and salt coions) which causes an effective screening inside the brush, the brush height is measure by the inflection point z_i , occurring in the monomer profile at the rim of the brush (see inset of Figure

5.3). Thus, the concentration of small ions inside the brush c''_{si} is obtained by counting the mobile ions within the layer $0 < z < z_i$. The corresponding values are also given in Table 5.1. On a log-log scale, in Figure 5.5, the average brush height $\langle z_m \rangle$ versus the ion concentration inside the brush c''_{si} is plotted. Both $\langle z_m \rangle$ and c''_{si} are rescaled with the corresponding salt-free values $\langle z_m \rangle_0$ and c''_0 respectively. The brush height scales with c''_{si} showing an exponent $\alpha \approx -0.31$. This result is in good agreement with the scaling law $h \sim c_s^{-1/3}$ predicted by Pincus for the salt dependence of the brush height in the osmotic regime [9]. Moreover, it is clear from Figure 5.5 that finite size effects due to the setting $L_z = 2N\sigma$ do not affect, at least, the scaling behavior (see the discussion on finite size effects in chapter 3).

Figures 5.6 and 5.7 show the endpoint height distribution $\rho_e(z)$ as a function of distance from the grafting surface z and for varying salt at grafting densities $\rho_a = 0.042\sigma^{-2}$ and $0.094\sigma^{-2}$, respectively, for $M = 36$ chains of length $N = 30$. The distribution $\rho_e(z)$ is normalized to unity. The average endpoint heights for systems considered in the present study (varying grafting density and salt concentration) are also listed in Table 5.1. Considering the salt free case here, one notes that, for the two grafting densities, the endpoint distribution exhibits a pronounced peak at large z and decays strongly inside the brush. These features reflect the highly ordered brush state due to strong stretching perpendicular to the grafting surface. As the salt concentration c_s is increased, the distribution remains qualitatively the same. In particular the peak that is shifted to lower z -values is still well pronounced. However, its height is slightly reduced and on the other hand its width becomes a bit larger. This result is in agreement with monomer density profiles shown in Figure 5.3 where one observes that the extension of the brush is reduced with added salt. However, note that $\langle z_e \rangle$ is less reliable than $\langle z_m \rangle$ because of the reduced statistical significance and because of higher sensitivity to finite size effects.

5.2 Chain Structure

The overall shape of the grafted polyelectrolyte can be described by the stretching ratio $r_s = \langle R^2 \rangle / \langle R_G^2 \rangle$ (see eqn. 2.35), where $\langle R^2 \rangle$ is the average square end-to-end distance and $\langle R_G^2 \rangle$ is the average radius of gyration squared. As shown in Figure 5.8 the ratio r_s is sensitive to the ionic strength in solution. As the concentration of salt is increased the ratio decreases as expected. However, the lower grafting density $\rho_a = 0.042\sigma^{-2}$ show a deeper decrease in r_s from the salt-less value compared to $\rho_a = 0.094\sigma^{-2}$ as the salt concentration is increased. This behavior is a consequence of high concentration in the brush phase which is growing for increasing anchoring density and salt concentration (see section 5.4).

For a more detailed examination of the chain structure of grafted polyelectrolytes at all length scales, the single chain structure factor is considered (see the salt-less case, section 4.2). We examine the spherically averaged structure factor, eqn. 4.9, as well as the structure factor

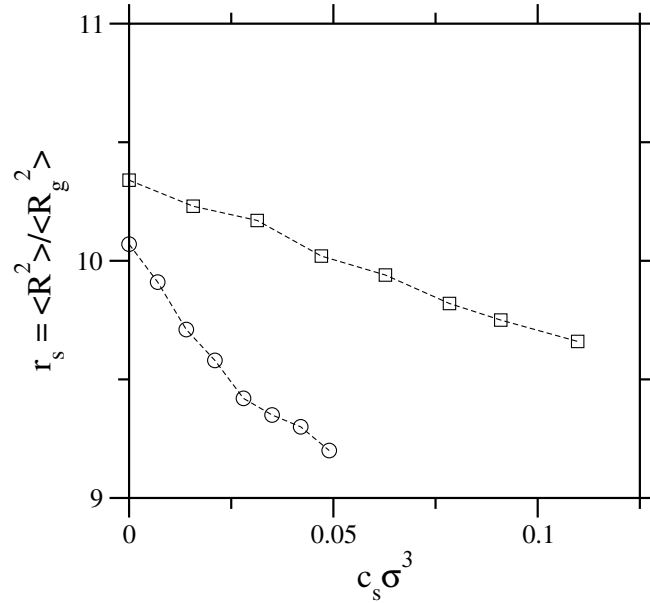


Figure 5.8: Shape factor $r_s = \langle R^2 \rangle / \langle R_g^2 \rangle$ for systems with $M = 36$ chains of length $N = 30$ as a function of salt concentration. Symbols are the same as in Figure 5.4.

in transverse direction $S(q_z)$ and the in-plane averaged one $S(q_{xy})$. Remember that in analogy to free chains, in the asymptotic regime the structure factor is expected to obey the scaling relation $S(q) \sim q^{-1/\nu}$ (see eqn. 2.57), where ν is the exponent of the N dependence of the chain radius $R \sim N^\nu$. Figure 5.9 gives the three different structure factors for the systems studied. Within the range of added salt for the two different anchoring densities studied, the spherically averaged structure factor $S(q)$ is almost not changed, reflecting strong stretching with Flory exponents in the range between 0.88 (no salt) and 0.82 (maximum salt). This result is consistent with the structure perpendicular to the grafting plane reflected by $S(q_z)$ which exhibits strong features of a rigid-rod-like behavior. However, the oscillations in $S(q_z)$ being related to ordering in z -direction get damped with increasing salt concentration which is in agreement with the reduction in chain stretching obtained in Figure 5.3. The in-plane behavior of the grafted polyelectrolyte chains is determined by the properties of the underlying neutral chains. As expected for our model, which is supposed to mimic polyelectrolytes under good solvent conditions, at grafting density $\rho_a = 0.042\sigma^{-2}$ and without salt $S(q_{xy})$ exhibits an in-plane scaling $R_{xy} \sim N^{0.57}$ close to the good solvent value 0.6. At larger grafting density $\rho_a = 0.094\sigma^{-2}$, however, the salt free $S(q_{xy})$ indicates $R_{xy} \sim N^{0.52}$, i.e., a scaling behavior close to that of a Gaussian chain well-known for chains in melt. Independent on the anchoring densities, additional salt tends to shift the behavior towards that of a better solvent quality, i.e., the correlation length is slightly growing and the blobs becomes little more swollen.

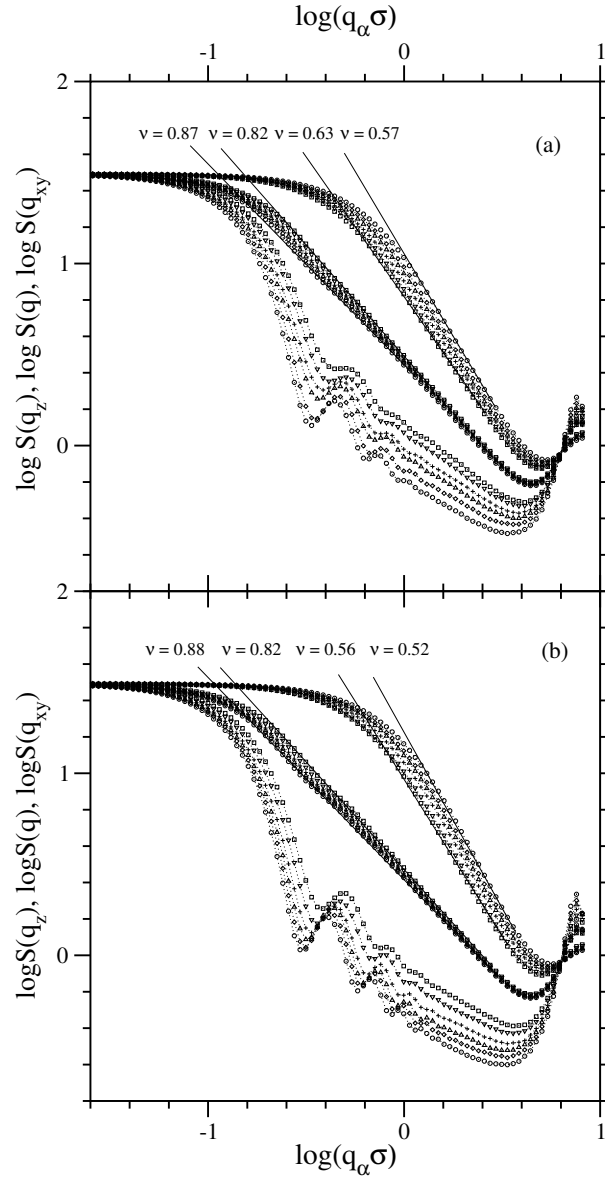


Figure 5.9: Spherically averaged structure factor $S(q)$ (middle set), in-plane averaged structure factor $S(q_{xy})$ (upper set), and structure factor perpendicular to the grafting plane $S(q_z)$ (lower set) of completely charged polyelectrolyte brushes ($\lambda_B = \sigma$): (a) grafting density $\rho_a = 0.042\sigma^{-2}$; (b) $\rho_a = 0.094\sigma^{-2}$. Symbols in (a) and (b) correspond to the same salt concentrations as in Figure 5.3(a) and 5.3(b), respectively.

5.3 Local net charge and ion distribution close to PEL chains

Results from the previous chapter shows that local electroneutrality for charged brushes in the nonlinear osmotic brush regime is fulfilled in perpendicular direction over almost the total

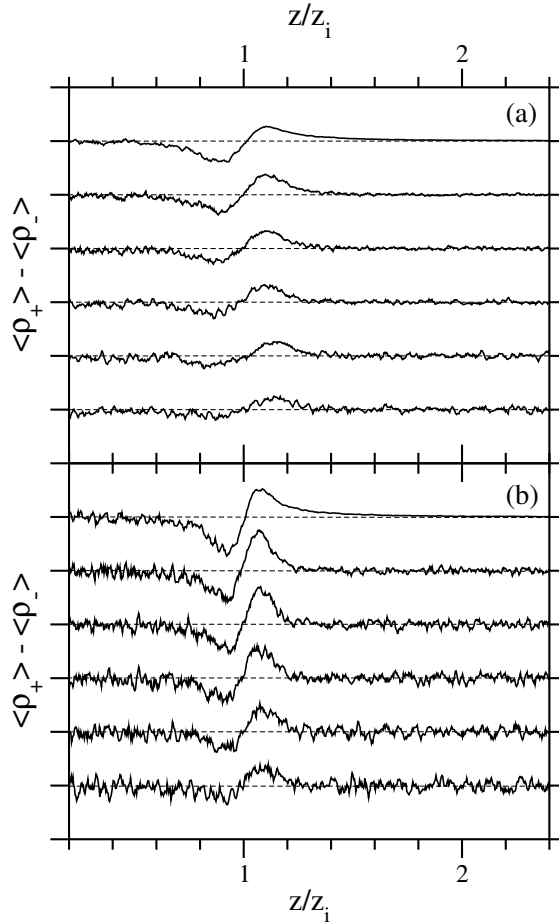


Figure 5.10: Local net charge $\langle \rho_+ \rangle - \langle \rho_- \rangle$ as a function of the distance from grafting surface z (rescaled with the inflection point height z_i): (a) grafting density $\rho_a = 0.042\sigma^{-2}$; (b) $\rho_a = 0.094\sigma^{-2}$. Each curve corresponds to a certain salt concentration that is growing from top to down with the values given in Figure 5.3(a) and 5.3(b), respectively. In both subplots the topmost curve shows the salt-less case and each zero line (dashed lines) is shifted by 0.02 in y -direction.

brush height except (i) in a rather thin layer close to the interface, and (ii) at the rim of the brush [10]. The local charge at small z is a consequence of the layering of monomers close to the grafting surface. The local net charge is compensated, however, over a length of the order of bond length. In Figure 5.10 the local net charge in layers parallel to the grafting plane as a function of their distance from that plane is plotted. For the sake of representation the region close to the anchoring points is omitted. Two features are evident: Except at the rim region $z \approx z_i$ one obtains only weak fluctuations around net charge zero. On the other hand, at the rim of the brush there appears a typical dipole with a depletion of counterions at $z \lesssim z_i$ and a corresponding enrichment beyond z_i . The strength of the dipole grows with grafting density while additional salt damps both the amplitude of local charges and its range in z -

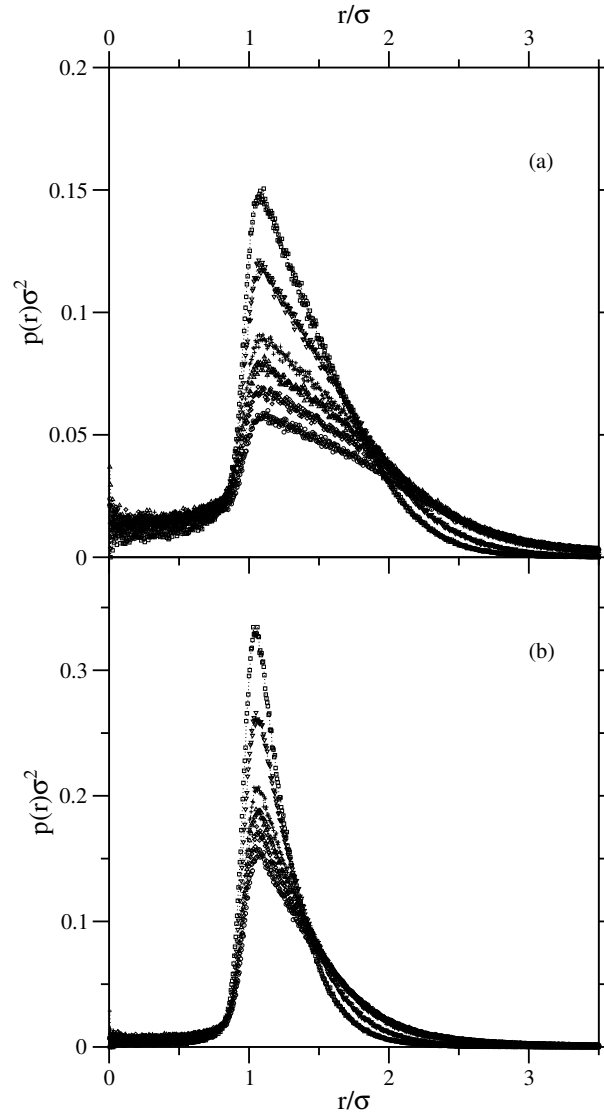


Figure 5.11: Ion-polyelectrolyte distribution function for completely charged chains ($\lambda_B = \sigma$): (a) grafting density $\rho_a = 0.042\sigma^{-2}$; (b) $\rho_a = 0.094\sigma^{-2}$. Symbols in (a) and (b) correspond to the same salt concentrations as in Figure 5.3(a) and 5.3(b), respectively. Note the different scale in y-direction in (a) and (b).

direction. Note that this dipole charge might have some influence on the interaction between two polyelectrolyte brushes (see chapter 6).

In the osmotic regime, the overall structure of the brush is determined by the balance between the polymer elasticity and the counterion osmotic pressure. Debye screening caused by additional salt ions reduces the counterion osmotic pressure. To discuss the role of correlations and the degree of counterion condensation, the ion-polyelectrolyte distribution function $p(r)$ is

calculated and shown in Figure 5.11, where r is the separation between the center of a positive ion and the closest polyelectrolyte bond. The distribution $p(r)$ is normalized according to $2\pi \int_0^\infty r p(r) dr = 1$. Figure 5.11 shows that the strength of correlations is monotonically growing both with grafting density and salt concentration. Comparing this behavior with previous results at strong [104] and moderate (see chapter 4) [105] electrostatic coupling, it can be concluded that this is a fingerprint of simple packing effects. Although the chain stretching is slightly reduced with increasing salt concentration, giving rise to an increased effective line charge density of the polyelectrolytes, both the range of the distribution function and its amplitude indicate that counterion condensation does not give a significant contribution to the enhanced correlations.

5.4 Transverse ion distribution and Donnan equilibrium

The relation between buffer concentration and the effective ion strength inside the brush is of interest both from theoretical as well as experimental point of view. To get the relationship between the ion concentration inside the brush c''_{si} and the buffer concentration c'_{si} which is obtained by counting all the small ions above the inflection point z_i (see inset of Figure 5.3), the ratio $c'_{\text{si}}/c''_{\text{si}}$ versus the salt concentration c'_s is plotted in Figure 5.12. From the point of view of the ion distribution perpendicular to the grafting plane a polyelectrolyte brush is very similar to the membrane equilibria problem where the membrane is impermeable to macroions but permeable to small ions. Hence one can divide the simulation box into two compartments with the membrane “boundary” located at the rim of the brush that is defined in our model by z_i . Due to the presence of the macroions in one compartment similarly charged ions are expelled from this compartment, giving rise to a somewhat nonhomogeneous distribution of the small ions as already pointed out by Donnan in 1911 [160, 161]. Applying the Donnan approach to the brush system the ratio of the small ions in both compartments becomes (see eqn. 2.110)

$$\frac{c'_{\text{si}}}{c''_{\text{si}}} = \left[1 + \left(\frac{fN\rho_a}{2z_i c'_s} \right)^2 \right]^{-1/2}, \quad (5.5)$$

with $fN = Q_p$ being the total charge of a polyelectrolyte chain and $\rho_a/z_i = c_p$ is the polymer concentration within the brush.

Because systems considered here are characterized by very small Gouy-Chapman lengths $\lambda_{\text{GC}} \ll h$, all the counterions are basically trapped inside the brush. Therefore the free ion concentration in the polymer-free volume can be set $c'_{\text{si}} = 2c'_s$. Although there occurs ion exchange between ‘original’ counterions and salt counterions, due to electroneutrality such an approximation remains reasonable. Note, however, that because of the finite volumes considered in the simulations the salt concentration in the polymer free volume c'_s is larger than the bare salt concentration c_s (see Table 5.1). Equation (5.5) shows clearly the nonhomogeneous

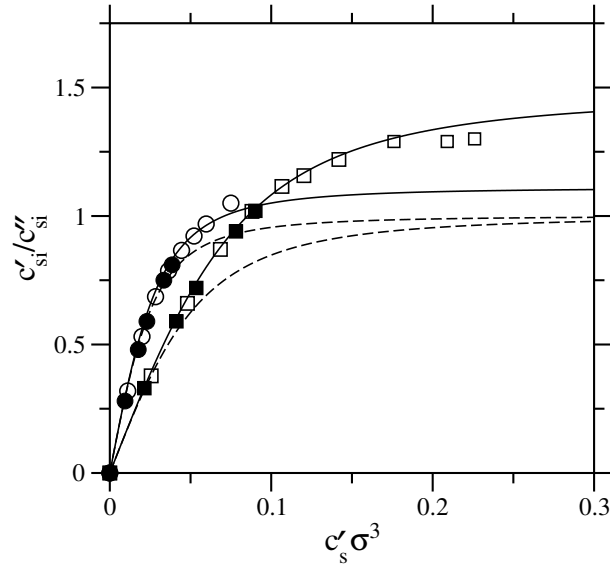


Figure 5.12: Relation between the ion concentration inside the brush c''_{si} and buffer concentration c'_{si} for different salt concentration c'_s . Simulation results (symbols as in Figure 5.4) and predictions of original (eqn. 5.5, dashed lines) and modified (eqn. 5.10, solid lines) Donnan approach. ($\sigma_{\text{eff}}^2 = 2\sigma^2$, see text).

distribution of small ions. However, with increasing salt concentration the difference between the two compartments is compensated and at $c_s \gg Q_p c_p$ one should obtain a uniform ion concentration $c'_{\text{si}} = c''_{\text{si}}$. In Figure 5.12, the predictions following from eq. (5.5) are given by dashed lines. Obviously the behavior disagrees with the simulation data that do not give a uniform ion concentration in the high-salt limit. But a surplus of small ions on the polymer-free side is obtained that is growing with increasing grafting density, i.e., with enhanced polymer concentration.

Note that the Donnan effect has been evaluated for a system of point-like constituents. While such an approximation is appropriate for dilute solutions obviously it fails for rather dense phases like polymer brushes. In chapter 4 it was shown that hard-core interactions between polymer monomers and counterions can be effectively taken into account within a free-volume approximation [10]. Here, the same approximation can be used to extend the Donnan equilibrium for dense solutions. Within that approach lets concentrate on the effective hard-core volume of a single polyelectrolyte chain v_{self} , which reduces the free volume that is available for the small ions. This free-volume theory therefore takes the hard-core interaction between the polymer monomers and the small ions into account in a nonlinear fashion. Compared to that the excluded-volume interaction between small ions is weak and will be neglected. Note that this approximation might fail at very high salt concentrations

where the short-ranged ion-ion interaction is expected to give a noticeable contribution. Due to the self-volume v_{self} the effective concentration of small ions on the polymer-containing side is growing as

$$c_i'' = \frac{n_i''}{V''} \implies \frac{n_i''}{V'' - v_{\text{self}}}, \quad (5.6)$$

with the bare volume in the brush available for a chain $V'' = h/\rho_a$. The self-volume of a polymer chain is roughly independent of the brush height and can be expressed in terms of the polymer contour length Nb and an effective monomer hard-core diameter σ_{eff} as $v_{\text{self}} = Nb\sigma_{\text{eff}}^2$, where σ_{eff} takes into account both the monomer and counterion diameters. Thus, the effective concentration can be written

$$c_i'' = \frac{n_i''}{V''(1-\eta)}, \quad (5.7)$$

with $\eta = v_{\text{self}}/V'' = \rho_a\sigma_{\text{eff}}^2Nb/h$ being the ratio of the polymer self-volume and the volume in the brush available for a chain and thus is the degree of close packing in the brush where the brush height h now being measured by the inflection point height z_i .

Using eq. (5.7) the condition of equilibrium given in eq. (2.106) becomes

$$\frac{n_+'n_-'}{(L_z - h)^2} = \frac{n_+''n_-''}{h^2(1-\eta)^2}, \quad (5.8)$$

which yields together with the conditions of electroneutrality, eqs. (2.107) and (2.108),

$$\begin{aligned} n_+''^2 - fNn_+'' &= c_s'^2 \left(\frac{h(1-\eta)}{\rho_a} \right)^2, \\ n_-''^2 + fNn_-'' &= c_s'^2 \left(\frac{h(1-\eta)}{\rho_a} \right)^2. \end{aligned} \quad (5.9)$$

Finally the ratio of small ions on both sides reads

$$\frac{c_{\text{si}}'}{c_{\text{si}}''} = \frac{1}{1-\eta} \left[1 + \frac{1}{(1-\eta)^2} \left(\frac{fN\rho_a}{2hc_s'} \right)^2 \right]^{-1/2}. \quad (5.10)$$

Hence, at a finite packing fraction η the distribution of the small ions at large c_s is never homogeneous, but it exhibits the asymptotic limit

$$\frac{c_{\text{si}}'}{c_{\text{si}}''} = \frac{1}{1-\eta}. \quad (5.11)$$

Now both the asymptotic value of the ratio of the small ions at $c_s \gg Q_p c_p$ as well as the particular shape of the function on c_s depend on η , i.e., on anchoring density and chain stretching. Applying the same effective polymer thickness $\sigma_{\text{eff}}^2 = 2\sigma^2$ [10] (eqn. 4.8) used in the previous chapter for the salt-less case to verify the weak dependence of brush height on grafting density (in the nonlinear osmotic brush regime), in Figure 5.12 the behavior following

from eq. (5.10) is given by solid lines. To obtain a continuous function the inflection point z_i is identified with the salt-free value z_i^0 although the brush height varies with salt concentration but, as discussed above, with a relatively weak power law $c_s^{-1/3}$. With these settings, one obtain packing fractions $\eta = 0.10$ and 0.32 for $\rho_a = 0.042\sigma^{-2}$ and $0.094\sigma^{-2}$, respectively, and the modified Donnan approach gives an almost perfect agreement with the simulation data.

Chapter 6

Interactions between two PEL brushes

Interactions between two PEL brushes that are grafted to two parallel surfaces are important, e.g., in preventing colloids in polar media from flocculation [52]. Scaling theory [9] suggests that in the case of compressed PEL brushes between walls, the disjoining pressure is the osmotic pressure of counterions and therefore the pressure scales as $1/D$, where D is the distance between the two anchoring surfaces. However, surface force apparatus experiments on interacting PEL brushes [119] neither observe this scaling prediction nor a refined theory exist to explain these experimental findings, at least at higher compressions. In such a situation simulations are a promising tool to validate theoretical predictions and experimental observations.

In this chapter, molecular dynamics simulation results on two interacting PEL brushes grafted between two parallel planes for decreasing separation between grafting planes D are discussed. The Bjerrum length is set, $\lambda_B = \sigma$. The results obtained are for completely charged brushes ($f = 1$) at two different anchoring densities $\rho_a = 0.042\sigma^{-2}$ and $0.094\sigma^{-2}$, respectively, with each brush having $M = 36$ chains of length $N = 30$. Note that these simulations are computationally rather expensive: Typically, depending on separation between the two grafting surfaces or on anchoring density one data point on IBM Power4+, 1.7 GHz supercomputer (massively parallel with 64 CPUs) takes between two to five days, while on sequential Alpha EV67/667 or Intel Xeon/3.06 processors it takes roughly from couple of weeks to a month.

6.1 Profile and interpenetration of two interacting brushes

Figure 6.1 shows snapshots from the equilibrium trajectories of two interacting brushes completely charged at grafting density $\rho_a\sigma^2 = 0.094$ for decreasing separation between grafting planes D . While chains with straight conformations would overlap at $D = 2Nb$, two brushes

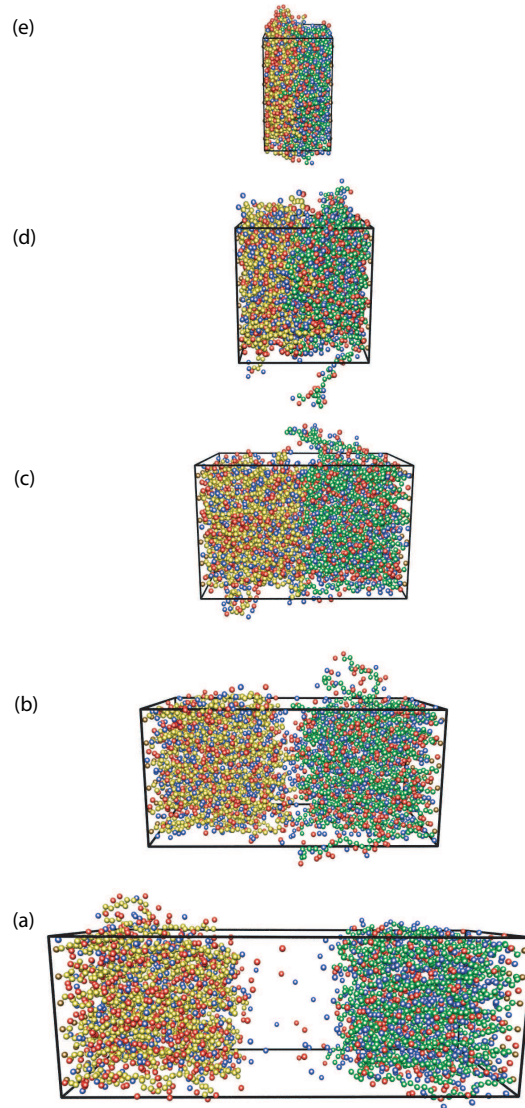


Figure 6.1: Two interacting polyelectrolyte brushes with each brush having $M = 36$ chains of length $N = 30$, completely charged at grafting density $\rho_a \sigma^2 = 0.094$ for decreasing separation between grafting planes D : (a) $D = 60\sigma$; (b) $D = 44\sigma$; (c) $D = 32\sigma$; (d) $D = 20\sigma$; (e) $D = 12\sigma$. The Bjerrum length is $\lambda_B = \sigma$. Counterions are assigned to the closest polyelectrolyte chain; polyelectrolyte chains are light yellow (or green), counterions are red (or blue), and anchor monomers are brown. The red and blue counterions were assigned to the proximity of yellow and green chains, respectively in the initial configuration. Snapshots have been represented by using the visualization program VMD [159].

come into contact only at smaller distances. At large separations D chains are far apart from overlap. In this case, immediately one realize that chains become strongly stretched and aligned perpendicular to the grafting surface similar to what is observed for PEL brushes

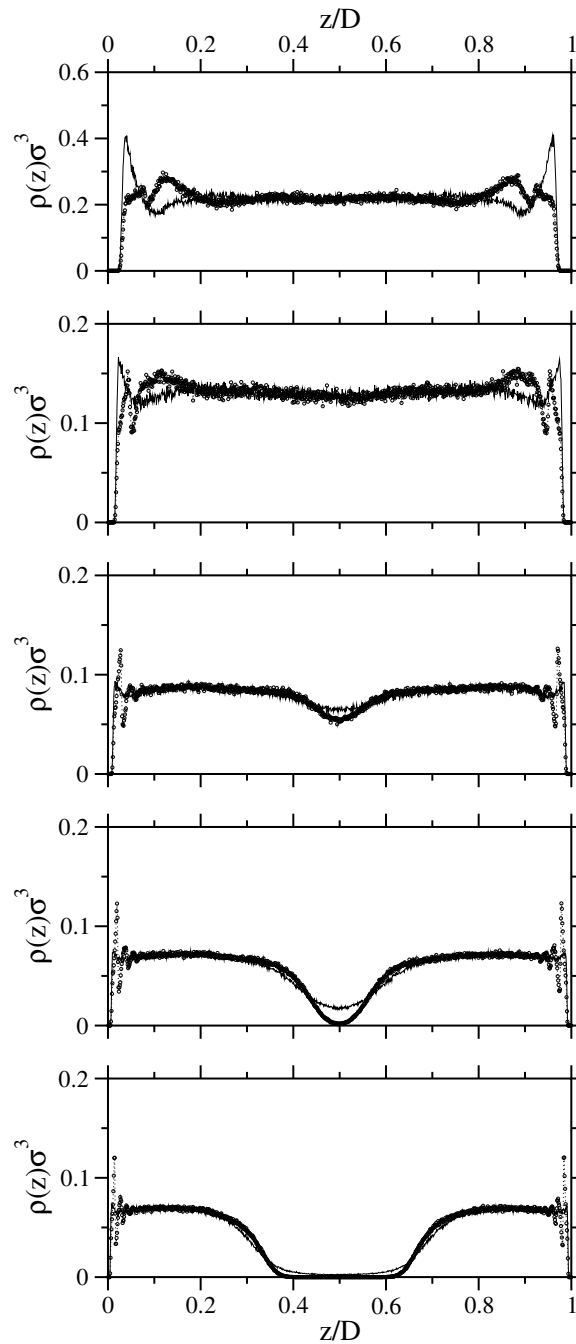


Figure 6.2: Simulated density profiles of monomers $\rho_m(z)$ (circles) and counterions $\rho_{ci}(z)$ (solid lines) for chains of length $N = 30$ at anchoring density $\rho_a\sigma^2 = 0.042$ for (from top to down) $D = 12\sigma$, $D = 20\sigma$, $D = 32\sigma$, $D = 44\sigma$, and $D = 60\sigma$. See the different values in y -direction for different D .

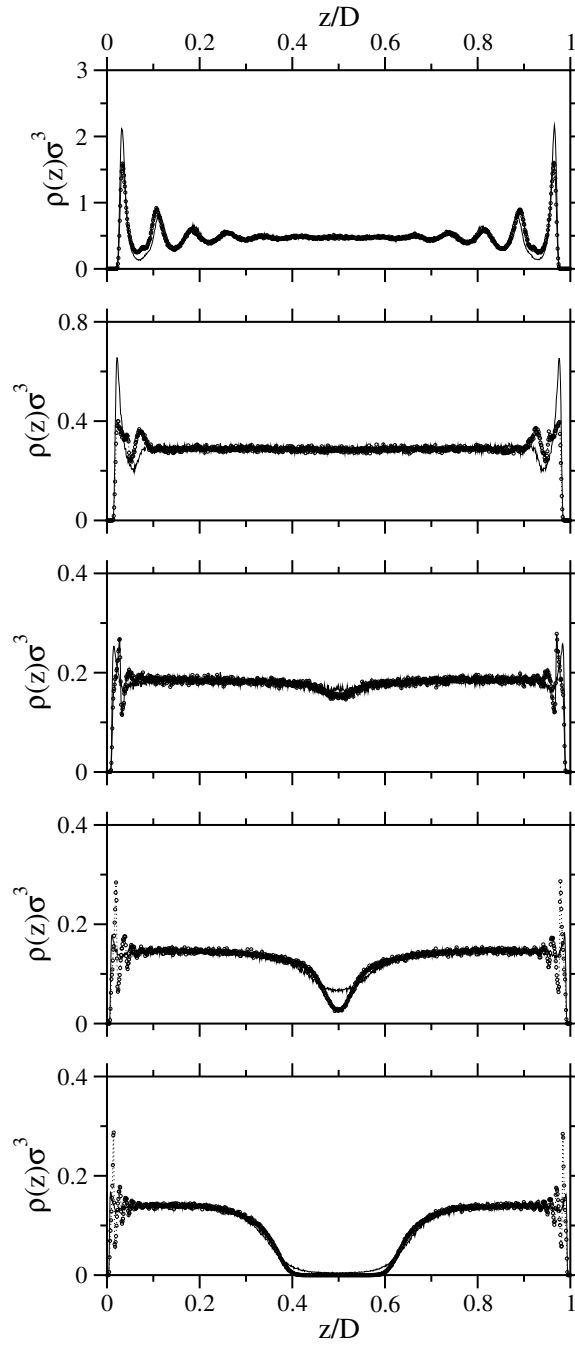


Figure 6.3: Same as Figure 6.2, but at anchoring density $\rho_a\sigma^2 = 0.094$. See the different values in y -direction for different D .

grafted to a single wall (Figure 4.1(d) and compare it with Figure 6.1(a)). As the separation between grafting planes is decreased, chains start overlapping for $D \lesssim (4Nb)/3$ (see Figure 6.1(b)). Again, this is in agreement with the previous finding (see chapter 4) for single grafted

Table 6.1: Simulation results on completely charged polyelectrolyte brushes with varying separation D between the two anchoring surfaces: average brush height $\langle z_m \rangle$, average endpoint height $\langle z_e \rangle$, and pressure π at two different grafting density ρ_a . ($\lambda_B = \sigma$).

$\rho_a \sigma^2$	D/σ	$\langle z_m \rangle/\sigma$	$\langle z_e \rangle/\sigma$	$\pi \sigma^3/\epsilon$
0.042	90	9.51 ± 0.01	17.89 ± 0.04	0.023
0.042	65	9.56 ± 0.01	17.77 ± 0.04	0.033
0.042	60	9.51 ± 0.01	17.73 ± 0.04	0.035
0.042	56	9.48 ± 0.01	17.59 ± 0.04	0.037
0.042	52	9.42 ± 0.01	17.52 ± 0.04	0.041
0.042	48	9.33 ± 0.01	17.30 ± 0.04	0.045
0.042	44	9.23 ± 0.01	17.10 ± 0.04	0.053
0.042	40	8.89 ± 0.01	16.31 ± 0.04	0.063
0.042	36	8.35 ± 0.01	15.00 ± 0.04	0.079
0.042	32	7.67 ± 0.01	13.37 ± 0.04	0.098
0.042	28	6.91 ± 0.01	11.66 ± 0.04	0.129
0.042	24	6.11 ± 0.01	9.91 ± 0.04	0.172
0.042	20	5.24 ± 0.01	8.17 ± 0.04	0.248
0.042	16	4.42 ± 0.01	6.60 ± 0.04	0.400
0.042	12	3.91 ± 0.01	5.82 ± 0.05	0.800
0.042	10	3.59 ± 0.01	5.12 ± 0.06	1.306
0.042	8	3.24 ± 0.01	4.43 ± 0.05	2.526
0.094	90	10.41 ± 0.01	19.80 ± 0.04	0.085
0.094	65	10.36 ± 0.01	19.66 ± 0.04	0.121
0.094	60	10.35 ± 0.01	19.67 ± 0.04	0.133
0.094	56	10.38 ± 0.01	19.72 ± 0.04	0.144
0.094	52	10.35 ± 0.01	19.69 ± 0.04	0.155
0.094	48	10.20 ± 0.01	19.22 ± 0.04	0.177
0.094	44	9.91 ± 0.01	18.60 ± 0.04	0.213
0.094	40	9.37 ± 0.01	17.40 ± 0.04	0.276
0.094	36	8.63 ± 0.01	15.67 ± 0.04	0.369
0.094	32	7.82 ± 0.01	13.80 ± 0.04	0.498
0.094	28	6.93 ± 0.01	11.72 ± 0.04	0.701
0.094	24	6.00 ± 0.01	9.75 ± 0.04	1.055
0.094	20	5.09 ± 0.01	8.03 ± 0.04	1.793
0.094	16	4.16 ± 0.01	6.33 ± 0.04	3.73
0.094	12	3.33 ± 0.01	5.10 ± 0.05	11.01
0.094	10	2.72 ± 0.01	5.37 ± 0.06	24.32
0.094	8	2.19 ± 0.01	4.27 ± 0.05	77.43

PEL brushes, that chains are extended up to about 2/3 of their contour length. Another point to note is that at all separations D , almost all counterions remain trapped inside the two brushes.

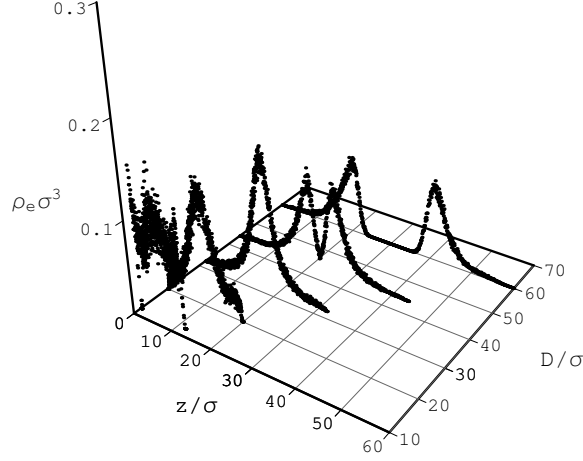


Figure 6.4: Endpoint distributions of two interacting brushes completely charged at grafting density $\rho_a = 0.042\sigma^{-2}$ ($\lambda_B = \sigma$) for varying D (values as given in Figure 6.2).

For completely charged brushes, Figures 6.2 and 6.3 give the monomer density $\rho_m(z)$ (and counterion density $\rho_{ci}(z)$) as a function of the distance from one of the anchoring planes z , and for decreasing separation D between grafting planes at anchoring densities $\rho_a\sigma^2 = 0.042$ and 0.094 , respectively. To place all the curves on the same scale z is scaled by D . $\rho_m(z)$ is normalized such that $\int_0^D dz \rho_m(z) = 2N\rho_a$. Considering Figure 6.2, both monomers and counterions follow very similar nearly steplike profiles at large separations where the brushes do not overlap. The fluctuations near grafting planes are a consequence of layering of monomers and counterions close to the walls. This result is consistent with the profiles obtained for PEL brushes anchored to a single wall (see Figure 4.2). As D is decreased, monomer and counterion densities increase everywhere and become almost uniform for $D \lesssim Nb$. In this case, counterion layering close to walls grows well above the monomer density. For high compressions layering due to the restricted motion of particles starts to appear in the density profiles with its range increasing with increasing compression. Such packing effects or short-range ordering is typical in liquids [82]. At large separations there is almost no qualitative difference in the profiles when the anchoring density is increased to $\rho_a\sigma^2 = 0.094$ (Figure 6.3). However, for denser grafting the layering is more clear at high compressions.

The average thickness of the brush is measured by taking the first moment of the monomer density profile (see eqn. 4.1). The average monomer height for the systems considered in the present study (varying separation D between grafting surfaces for the two different grafting

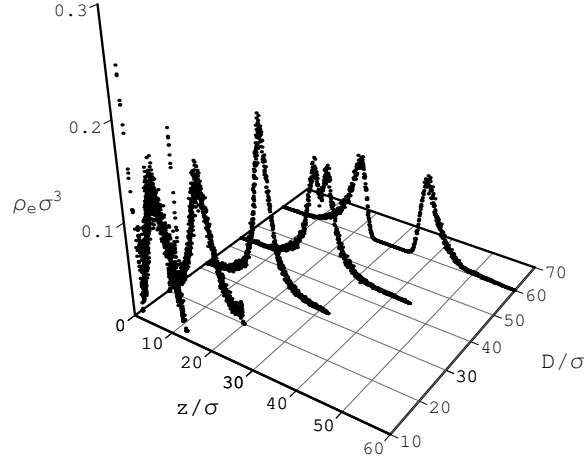


Figure 6.5: Endpoint distributions of two interacting brushes completely charged at grafting density $\rho_a = 0.094\sigma^{-2}$ ($\lambda_B = \sigma$) for varying D (values as given in Figure 6.2).

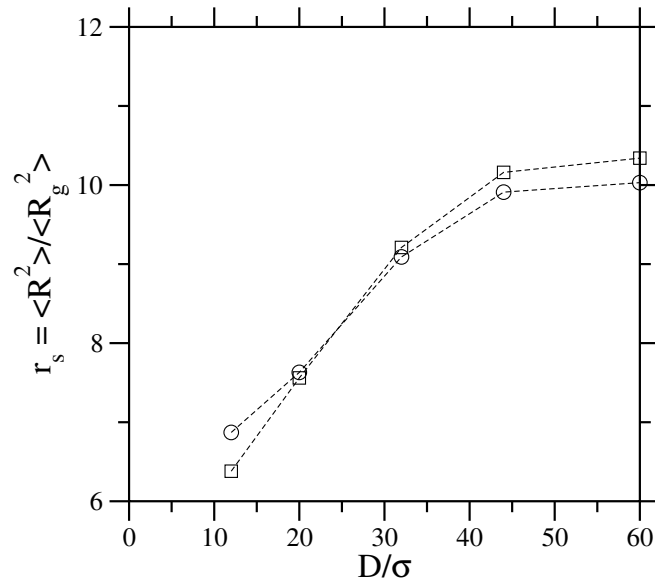


Figure 6.6: Shape factor $r_s = \langle R^2 \rangle / \langle R_g^2 \rangle$ for systems with $M = 36$ chains of length $N = 30$ as a function of separation D . The data given are for grafting density $\rho_a = 0.042\sigma^{-2}$ (circles) and $\rho_a = 0.094\sigma^{-2}$ (squares).

densities) are given in Table 6.1. As the separation D decreases, the chains overlap and the brush height decreases.

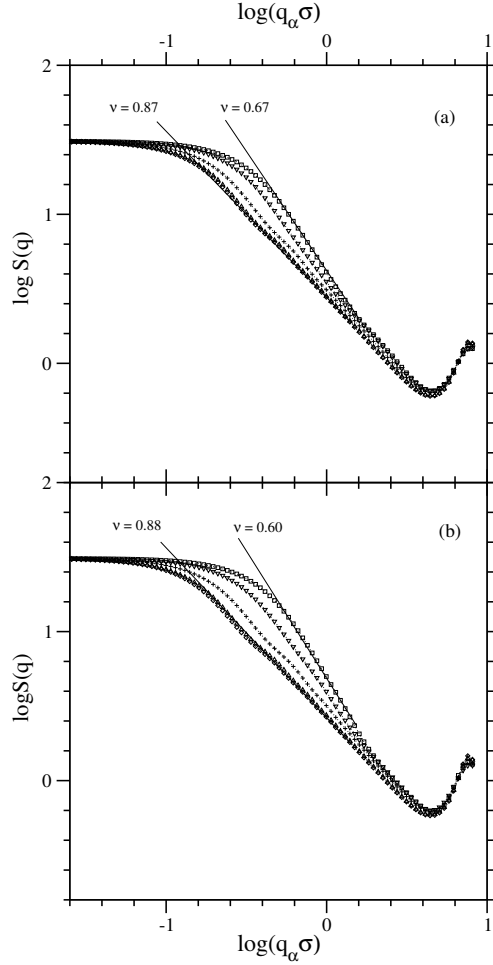


Figure 6.7: Spherically averaged structure factor $S(q)$ of completely charged polyelectrolyte brushes ($\lambda_B = \sigma$): (a) grafting density $\rho_a = 0.042\sigma^{-2}$; (b) $\rho_a = 0.094\sigma^{-2}$. Symbols in (a) and (b) correspond to $D = 60$ (diamonds), $D = 44$ (triangles up), $D = 32$ (plus), $D = 20$ (triangles down), and $D = 12$ (squares).

Figures 6.4 and 6.5 show the endpoint height distribution $\rho_e(z)$ at grafting densities $\rho_a\sigma^2 = 0.042$ and 0.094 , respectively, for $M = 36$ chains of length $N = 30$. The distribution $\rho_e(z)$ is normalized to unity. The average endpoint heights for systems considered in the present study (varying separation D between grafting surfaces for the two different grafting densities) are also listed in Table 6.1. When the separation between the grafting surfaces is well above $D \approx (4Nb)/3$, the endpoint density profile is very similar to the case of the single brush (see Figure 4.5). As D is decreased the corresponding two maximum at large z -values in the endpoint distribution for the two brushes start to overlap. For higher compressions the density profile broadens and consequently the amplitude of the coalesced maxima decreases, i.e., the probability of finding the ends in the region $z > D/2$ significantly increases. The increased

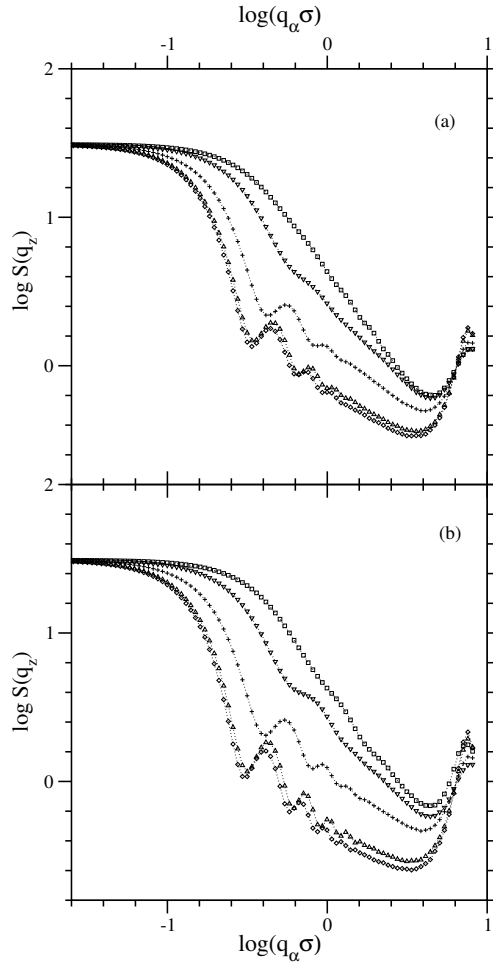


Figure 6.8: Structure factor perpendicular to grafting planes $S(q_z)$ of completely charged polyelectrolyte brushes ($\lambda_B = \sigma$): (a) grafting density $\rho_a = 0.042\sigma^{-2}$; (b) $\rho_a = 0.094\sigma^{-2}$. Symbols as in Figure 6.7.

noise at the minimum D given in the figures is mainly due to averaging over comparatively less statistical realizations due to a smaller trajectory length obtained in simulations.

6.2 Chain Structure

The overall shape of the grafted polyelectrolyte can be described by the stretching ratio $r_s = \langle R^2 \rangle / \langle R_G^2 \rangle$ (see eqn. 2.35), where $\langle R^2 \rangle$ is the average square end-to-end distance and $\langle R_G^2 \rangle$ is the average radius of gyration squared. As shown in Figure 6.6 the ratio r_s is sensitive to the separation D . At large separations $D \gtrsim (4Nb)/3$ the ratio saturates to the value observed for PEL brushes grafted to a single wall. As D is decreased the ratio also decreases, i.e. chains are being reduced in their extensions as the two brushes are compressed against each other and

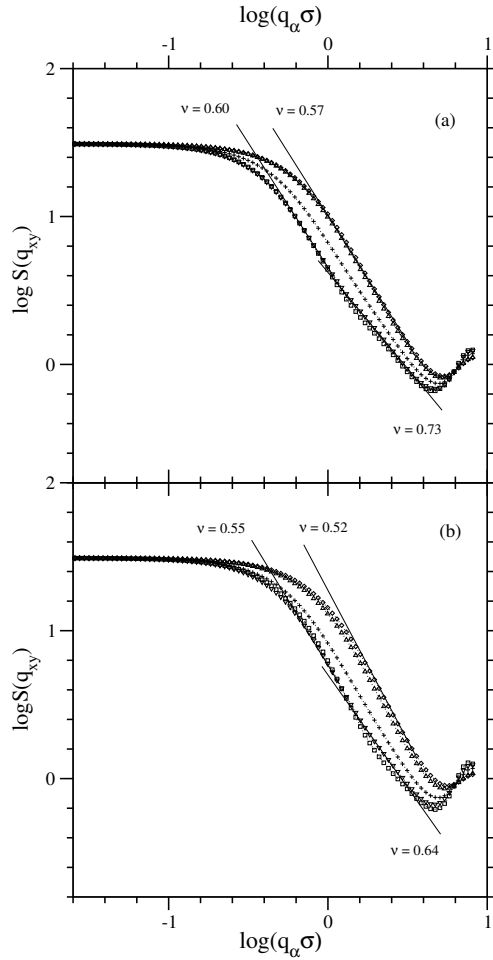


Figure 6.9: In-plane averaged structure factor $S(q_{xy})$ of completely charged polyelectrolyte brushes ($\lambda_B = \sigma$): (a) grafting density $\rho_a = 0.042\sigma^{-2}$; (b) $\rho_a = 0.094\sigma^{-2}$. Symbols as in Figure 6.7.

at the maximum compression shown in the figure one obtains a value close to Gaussian chain, $r_s = 6$, well-known for chains in melt. The deviation observed in the figure due to $D = 12\sigma$ at anchoring density $\rho_a\sigma^2 = 0.042$ is probably because of increased statistical error in this data point (see also Figure 6.4).

For a more detailed examination of the chain structure of grafted polyelectrolytes at all length scales, the single chain structure factor is considered. We examine the spherically averaged structure factor, eqn. 4.9, as well as the structure factor in transverse direction $S(q_z)$ and the in-plane averaged one $S(q_{xy})$. Remember that in analogy to free chains, in the asymptotic regime the structure factor is expected to obey the scaling relation $S(q) \sim q^{-1/\nu}$, where ν is the exponent of the N dependence of the chain radius $R \sim N^\nu$. Figure 6.7 gives the spherically averaged structure factor $S(q)$. The Flory exponents are in the range between 0.87

(lower compression) and 0.60 (higher compression) for the two anchoring densities studied. This means that the chain extension is considerably reduced for decreasing separation D as expected. This result is consistent with the structure perpendicular to the grafting plane reflected by $S(q_z)$ in Figure 6.8 which exhibits strong features of a rigid-rod-like behavior at large separation D . For both the anchoring densities oscillations in $S(q_z)$ being related to ordering in z -direction get damped with decreasing separation.

As mentioned before, the in-plane behavior (see Figure 6.9) of the grafted polyelectrolyte chains is determined by the properties of the underlying neutral chains. At large separations D , the values of the exponent ν are consistent with the single brush studies: As expected for our model, which is supposed to mimic polyelectrolytes under good solvent conditions, at grafting density $\rho_a = 0.042\sigma^{-2}$, $S(q_{xy})$ exhibits an in-plane scaling $R_{xy} \sim N^{0.57}$ close to the good solvent value 0.6. For $\rho_a = 0.094\sigma^{-2}$, we find $R_{xy} \sim N^{0.52}$ which is in agreement with the shift towards melt behavior earlier obtained at high grafting densities for single brush studies. Due to the compression in z -direction, independently on the anchoring density chains tend to swell in lateral directions giving a growing exponent with decreasing wall separation D . Note that at high compressions there seems to be another scaling exponent in the high q -regime for both anchoring densities considered here. The differing behavior at lower D indicates a relatively decreasing brush behavior which is in agreement with the brush profiles discussed above.

6.3 Local net charge and ion distribution close to PEL chains

In Figure 6.10 the local net charge in layers parallel to the grafting planes is plotted as a function of distance z from one of the planes. At large separations $D > (4Nb)/3$, there is a dipole emerging at the rim of the brush, as seen previously in the case of single grafted brush. However, as the separation D is decreased, the dipoles at the rim of the brush overlap and finally vanishes for higher compressions. For all D except near to the anchoring planes the net charge is almost zero over the whole range of the box. At higher compressions, charge compensation near the anchoring planes is less pronounced which is probably due to the restricted freedom for the particles. To discuss the role of correlations and the degree of counterion condensation, the ion-polyelectrolyte distribution function $p(r)$ is calculated and shown in Figure 6.11, where r is the separation between the center of a positive ion and the closest polyelectrolyte bond. The distribution $p(r)$ is normalized according to $2\pi \int_0^\infty r p(r) dr = 1$. Figure 6.11 shows that at large separations the distribution for both grafting densities is comparable to the one obtained for single brush studies. However, the strength of correlations is monotonically growing with decreasing separation D . Again this seems to be a simple packing effect, although at very high compressions the amplitude is comparable to that found for PEL brushes in the collapsed regime at high Coulomb strength [104].

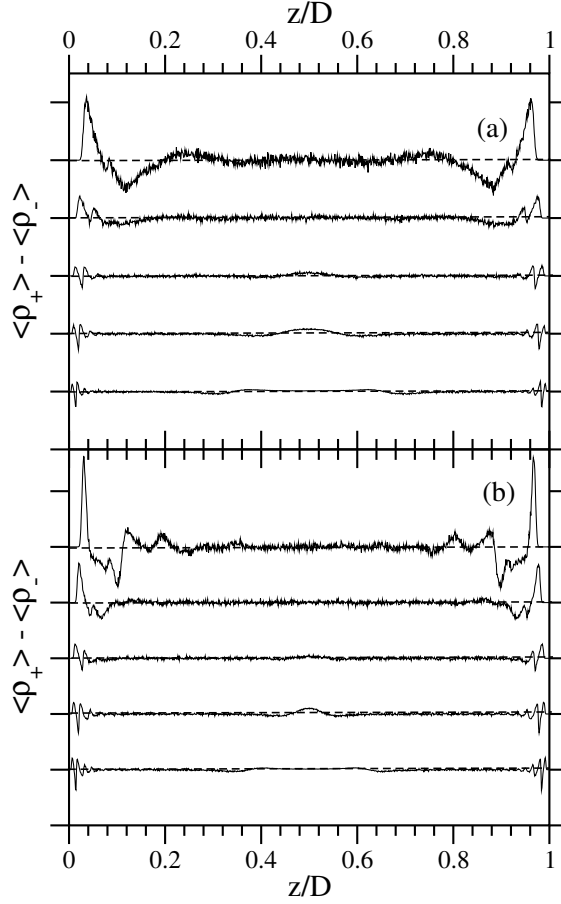


Figure 6.10: Local net charge $\langle \rho_+ \rangle - \langle \rho_- \rangle$ as a function of the distance z from one of the grafting surfaces (rescaled with the separation between anchoring planes D): (a) grafting density $\rho_a = 0.042\sigma^{-2}$; (b) $\rho_a = 0.094\sigma^{-2}$. Each curve corresponds to a certain separation distance D which is increasing from top to down with the values given in Figure 6.2. The zero line (dashed lines) is shifted by 0.2 units in y -direction for $\rho_a = 0.042\sigma^{-2}$ and 0.4 units for $\rho_a = 0.094\sigma^{-2}$.

6.4 Pressure of two interacting brush systems

To have a better understanding of the interactions between the two brushes which are compressed against each other, we estimated the pressure which can be directly obtained in simulations. At each separation D , the pressure is calculated as

$$\pi = \frac{N_{\text{tot}}}{V}(k_B T + \langle v_2 \rangle), \quad (6.1)$$

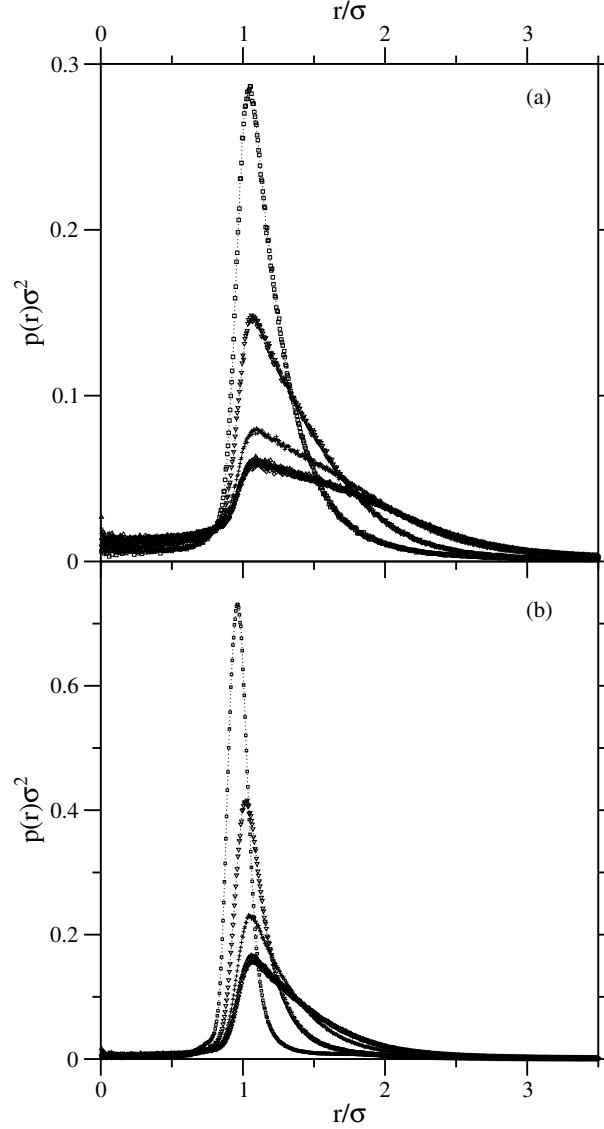


Figure 6.11: Ion-polyelectrolyte distribution function for two interacting PEL brushes completely charged at $\lambda_B = \sigma$: (a) grafting density $\rho_a = 0.042\sigma^{-2}$; (b) $\rho_a = 0.094\sigma^{-2}$. Symbols as in Figure 6.7.

with

$$\langle v_2 \rangle = -1/(3N_{\text{tot}}) \left(\sum_{i=1}^{N_{\text{tot}}-1} \sum_{j=i+1}^{N_{\text{tot}}} \langle \nabla U'_{ij} \cdot \mathbf{r}_{ij} \rangle - \langle U_{\text{Coul}} \rangle \right), \quad (6.2)$$

where the first term in eq. 6.1 is the ideal gas contribution and the second term is the pressure virial [156] per particle. The virial in eq. 6.2 is subdivided into contributions from the short-range part of the potential ($U' = U - U_{\text{Coul}}$) and the electrostatic part [164] to properly

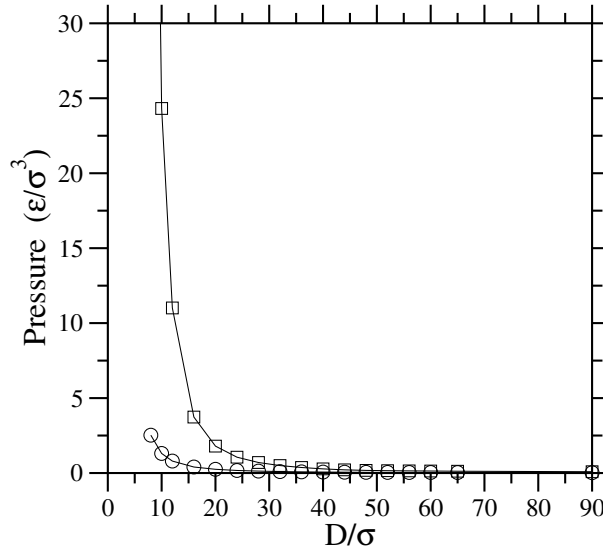


Figure 6.12: Pressure vs. separation distance D between the two anchoring planes for completely charged PEL brushes at $\lambda_B = \sigma$. Symbols as in Figure 6.6.

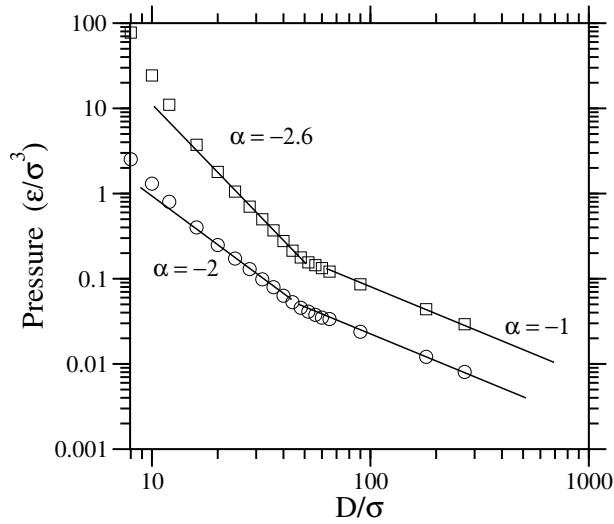


Figure 6.13: Log-log plot showing pressure vs. separation distance D between the two anchoring planes for completely charged PEL brushes at $\lambda_B = \sigma$. Symbols as in Figure 6.6.

account for the long-range nature of the Coulomb interaction [125]. N_{tot} is the total number of particles, $V = L_x \times L_y \times D$ is the volume of the simulation box and $-\nabla U'_{ij}$ is the short-range

force on particle i due to j , along $\mathbf{r}_{ij} = \mathbf{r}_i - \mathbf{r}_j$.

The evaluated pressure $\pi(D)$ is plotted against the separation between the two anchoring surfaces in Figure 6.12 (also listed in Table 6.1). As it is evident from the figure, increasing anchoring density increases the pressure. A very weak increase in pressure at large separations followed by a rapid increase at low D value is observed. To find whether there exist any scaling regimes, we plot the data in a log-log representation in Figure 6.13. There seems to be atleast two regimes for both anchoring densities studied. At large separation distances D the virial in eqn. 6.2 remains constant, consequently the pressure scales with D with exponent -1. However at separations $D \lesssim (4Nb)/3$ the behavior changes to an exponent ≈ -2 for anchoring density $\rho_a = 0.042\sigma^{-2}$, and ≈ -2.6 for $\rho_a = 0.042\sigma^{-2}$. This crossovers might be due to the repulsive interactions between chains, because the relative change in the slope occurs when the two brushes just start to overlap at $D \approx (4Nb)/3$ (see snapshot Figure 6.1, and density profiles Figures 6.2 and 6.3).

Note that the theoretical prediction for the scaling dependence of pressure on compressions D is $\pi \sim D^{-1}$ (see eqn. 2.111) [9]. This relation is purely based on the osmotic pressure of counterions (counterions assumed as an ideal gas) and completely neglects the role of polymer.

At very large compressions $D \lesssim Nb/2$ a third regime is seen. This could be an effect of a crossover from brush behavior to an layered structure which is visible in the monomer density profiles, Figures 6.2, and 6.3. The behavior seen in the simulation is in qualitative agreement with experimental data [119]. Doubtless the simulation data provide a basis for a better theoretical understanding of the interaction between PEL brushes. Nevertheless the simulation results have to be confirmed for a wider parameter range.

Chapter 7

Conclusions

Polyelectrolytes (PELs) or charged polymers anchored on surfaces are fascinating for their wide spectrum of applications, but they also form a challenging topic for pure science. Due to various interactions, tethered chains are enforced to take an elongated conformation giving rise to a brush-like structure. Modern scaling concepts introduced by de Gennes [2] can help the theoretical understanding of these systems. Computer simulations are a promising tool to check theoretical predictions and to study regimes that are not easily accessible in experiments.

We perform extensive molecular dynamics simulations of polyelectrolyte brushes using local compute servers as well as massively parallel supercomputers. The full Coulomb interaction of monomers, counterions, and salt ions is treated explicitly. Our model also includes excluded volume interaction between monomers, counterions, and salt ions.

It is well known that simulations on charged systems are computationally rather expensive [141, 156] due to the long range nature of Coulomb interaction which is to be handled by using special methods like the Ewald summation method [22]. Using $\mathcal{O}(N_{\text{tot}}^2)$ methods (N_{tot} is the total number of charged particles), e.g., Ewald summation or due to a summation technique proposed by Lekner [146] applied to the particular brush geometry, within the current computational capabilities one is able to simulate only up to about 2000 charged particles [104]. For considering larger systems, one has to pass over to improved methods which give a better time scaling in treating long-ranged interactions. Here, a new method called MMM2D [145] is employed to calculate the Coulomb sum in the particular brush geometry. This method has got an $\mathcal{O}(N_{\text{tot}}^{5/3} \log(N_{\text{tot}})^2)$ scaling (already for $N_{\text{tot}} > 100$ the factor becomes larger than unity when compared with the $\mathcal{O}(N_{\text{tot}}^2)$ method due to Lekner [146]) and now we are able to simulate up to about 10000 charged particles. This allows studying the effect of, e.g., additional salt ions in the PEL brush system.

The following conclusions are reached from the simulation studies on strong PEL brushes at constant temperature:

- (1) For PEL brushes in the nonlinear osmotic brush regime (see chapter 4) the brush height h slightly increase with increasing grafting density ρ_a which is in contrast to the well

known scaling prediction for the osmotic brush regime. Also, brushes extent up to about $2/3$ of their contour length which is certainly beyond the range where linear elasticity theory can be applied. A simple scaling approach is applied that incorporates the excluded volume effects in a free-volume formulation, similar to the classical derivation of the van der Waals equation of state. Within this theory one can understand the findings obtained in simulations and later also in experiment on a semi-quantitative level. The self-volume is expressed in terms of an effective monomer hard-core diameter σ_{eff} and the polymer contour length Nb as $v_{\text{self}} = Nb\sigma_{\text{eff}}^2$, where σ_{eff} takes into account both the monomer and counterion diameters. The volume available for counterions $V_0'' = h/\rho_a$ is reduced by v_{self} , thus the free-volume is given by $V'' = V_0''(1 - \eta)$, where η is the packing fraction of the polymer chain in the brush. Balancing the resulting nonlinear entropy of counterions (see eqn. 4.2) against the high-stretching elasticity (see eqn. 4.4: $h \approx Nb$ case) of the chain, the equilibrium brush height depends on ρ_a indeed. The nonlinear theory evaluated with $\sigma_{\text{eff}}^2 = 2\sigma^2$ agrees with the simulation results (see Figure 4.4) [10]. However, note that these findings meanwhile also obtained in experiments [10] could also be explained by considering lateral inhomogeneity of counterion distribution [94].

(2) For PEL brushes with added salt (see chapter 5), in the nonlinear osmotic brush regime the brush thickness is found to shrink with increasing electrolyte concentration. The scaling behavior of brush height (see Figure 5.4) is in almost perfect agreement with the prediction by Pincus for the salt dependence in the osmotic brush regime $h \sim c_s^{-1/3}$ [106]. The prediction is based on the assumption that screening from the added salt reduces the counterion osmotic pressure which stretches the chains. In the high salt limit $c_s \gg c_{\text{ci}}$, balancing the resulting osmotic pressure (see eqn. 2.98) against the Gaussian elasticity of the polymer chain yields a weak dependence of the brush height on salt concentration [9]. Note, however, that in the simulations we could not obtain many data points in the asymptotic limit of the so-called salted brush where $c_s \gg c_{\text{ci}}$. Therefore the contribution by the natural counterions cannot be neglected, but all mobile ions (counterions as well as salt ions) within the brush have to be taken into account. That is why we consider the brush stretching as a function of the concentration of mobile ions within the brush c_{si}'' and not as a function of the salt concentration c_s only. Thus, finally we observe an almost perfect agreement with the scaling prediction (see Figure 5.5).

The relation between buffer concentration c_{si}' and the effective ion strength inside the brush c_{si}'' at varying salt concentration c_s is of interest both from theoretical as well as experimental point of view. Due to the polymer layer close to the anchoring surface, a priori there is a nonhomogeneous particle distribution perpendicular to the interface. The first attempt to understand the relation between the concentrations of small ions in the brush and outside the polymer layer at varying salt concentration is by a Donnan equilibrium approach. But this fails because of the high concentration in the brush state (see Figure 5.12). At high

densities, as it is forced in polyelectrolyte brushes, the approximation of point-like ions in the Donnan approach is not justified, but excluded volume effects become relevant. However, the relation between the total ion concentration within the brush and the buffer concentration can be understood on the basis of an extended Donnan equilibrium approach. Within that approach the self-volume of PEL chains is taken into account as indicated above. Using the same parameter σ_{eff} as in the case of the dependence of brush height on grafting density we observe an almost perfect agreement with the simulation results [106]. The extended Donnan equilibrium relation represents an interesting theoretical prediction that should be checked by experimental data.

(3) For two interacting PEL brushes grafted to two parallel surfaces (see chapter 6) the monomer density profiles obtained in the simulation shows that the chains start to overlap only at $D \approx (4Nb)/3$, where D is the separation between the two grafting planes (see Figures 6.2 and 6.3). This result is the expected one considering the above simulation studies on single grafted brush which showed that chains are extended up to about $2/3$ of their contour length. Further decreasing D , the profiles look almost homogeneous over the whole range of the box for $D \lesssim Nb$, except at higher compressions, where layering close to the two planes appear more pronounced. Its amplitude as well as range are growing with decreasing D . This is expected to be due to the restricted motion of particles near the two anchored surfaces. Such a density distribution is also observed in liquids [82]. Comparing the monomer density profiles with the counterion density profiles or looking at the local net charge density in direction perpendicular to the anchoring planes, for all D the net charge is almost zero over the whole range of the box except near to the two anchoring planes.

The pressure curve shows mainly three different regimes as the separation between the two grafting planes is decreased (see Figure 6.12). At large separations where the chains do not overlap, the pressure virial remains almost constant. Therefore we obtain the behavior $\pi \sim 1/D$ for $D \gtrsim (4Nb)/3$ independent of anchoring density. As D is decreased a new regime appears which has different exponent for the pressure dependence on D depending on the anchoring density. However, here we do not observe the scaling prediction $\pi \sim 1/D$ [9] for interacting chains. This might be due to the fact that in the scaling analysis the excluded volume effects are neglected, but could be important for dense systems which are considered here. At very large compressions a third regime is seen. This could be an effect of a crossover from brush behavior to an layered structure. However, these findings have to be studied in more detail in future simulations.

Appendix A

The MMM2D method

This appendix gives a short overview on the MMM2D method [145]. The Coulomb summation for the particles in the central simulation box as well as in the image boxes is given as (in reduced units)

$$U_{\text{Coul}}(r) = \sum_{k=-\infty}^{\infty} \sum_{l=-\infty}^{\infty} \sum_{i=1}^{N_{\text{tot}}-1} \sum_{j=i+1}^{N_{\text{tot}}} \frac{q_i q_j}{|r_{ij} + kL + lL|}, \quad (1.1)$$

where $r_{ij} = (x_{ij}, y_{ij}, z_{ij}) = r_i - r_j$ (r_i and r_j are the position coordinates of particles i and j , respectively), and the indices k and l run over the periodic images of the simulation box. N_{tot} is the total number of charges, and L is the planar box length.

Similar to MMM [144], MMM2D uses an exponential convergence factor, i.e. eqn. 1.1 can be now written for the interaction energies of particle i with all other charges, defined as

$$\begin{aligned} U_i(r) &= \lim_{\beta \rightarrow 0} \sum_{k=-\infty}^{\infty} \sum_{l=-\infty}^{\infty} \sum_{j=1}^{N_{\text{tot}}}{}' \frac{q_i q_j e^{-\beta|r_{ij}+kL+lL|}}{|r_{ij} + kL + lL|} \\ &= \lim_{\beta \rightarrow 0} \sum_{j=1}^{N_{\text{tot}}} q_i q_j \phi_{\beta}(x_{ij}, y_{ij}, z_{ij}), \end{aligned} \quad (1.2)$$

(prime ' on the inner sum in the above equation indicates that the term $j = i$ for $k = l = 0$ is omitted) where

$$\phi_{\beta}(x_{ij}, y_{ij}, z_{ij}) = \tilde{\phi}_{\beta}(x_{ij}, y_{ij}, z_{ij}) + \begin{cases} \frac{e^{-\beta r}}{r} & (x_{ij}, y_{ij}, z_{ij}) \neq (0, 0, 0), \\ 0 & (x_{ij}, y_{ij}, z_{ij}) = (0, 0, 0) \end{cases} \quad (1.3)$$

and

$$\tilde{\phi}_{\beta}(x_{ij}, y_{ij}, z_{ij}) = \sum_{(k,l) \neq (0,0)} \frac{e^{-\beta r_{kl}}}{r_{kl}}, \quad (1.4)$$

where the distance

$$r_{kl} = \sqrt{(x_{ij} + kL)^2 + (y_{ij} + lL)^2 + (z_{ij})^2}, \quad r_k = r_{k0}, \quad r = r_0. \quad (1.5)$$

Transformation of ϕ_β for $z_{ij} \neq 0$ - the far formula

For $z_{ij} \neq 0$ and $\beta > 0$ the sum in ϕ_β is an absolutely convergent sum of Schwartz class functions. Therefore for $\delta > 0$, and $r \in \mathbb{R}$, where \mathbb{R} is the set of real numbers one could apply the *Poisson formula*

$$\sum_k f(r + \delta k) = \frac{1}{|\delta|} \sum_p \mathcal{F}(f) \left(\frac{p}{\delta} \right) e^{2\pi i \frac{p}{\delta} r} \quad (1.6)$$

(\mathcal{F} denotes the Fourier transformation) on eqn. 1.3 and the summation can now be done in the Fourier space

$$\phi_\beta(x_{ij}, y_{ij}, z_{ij}) = \sum_{k,l} \frac{e^{-\beta r_{kl}}}{r_{kl}} = \frac{2\pi}{L^2} \sum_{p=-\infty}^{\infty} \sum_{q=-\infty}^{\infty} \frac{e^{-\beta_{pq}|z_{ij}|}}{\beta_{pq}} e^{2\pi i p x_{ij}/L} e^{2\pi i q y_{ij}/L}, \quad (1.7)$$

where $\beta_{pq} = \sqrt{\beta^2 + (2\pi p/L)^2 + (2\pi q/L)^2}$, and p and q indices are the frequencies in the Fourier space along the transformed coordinates x and y , respectively. Finally after applying the limit $\beta \rightarrow 0$, the far formula reads

$$\begin{aligned} \phi(x_{ij}, y_{ij}, z_{ij}) &= \frac{4}{L^2} \sum_{p,q>0} \frac{e^{-2\pi f_{pq}|z_{ij}|}}{f_{pq}} \cos(\omega_p x_{ij}) \cos(\omega_q y_{ij}) \\ &+ \frac{2}{L^2} \left(\sum_{p>0} \frac{e^{-2\pi f_p|z_{ij}|}}{f_p} \cos(\omega_p x_{ij}) + \sum_{q>0} \frac{e^{-2\pi f_q|z_{ij}|}}{f_q} \cos(\omega_q y_{ij}) \right) \\ &- \frac{2\pi|z_{ij}|}{L^2}, \end{aligned} \quad (1.8)$$

where

$$\begin{aligned} f_{pq} &= \sqrt{(p/L)^2 + (q/L)^2}, \quad f_p = p/L, \quad f_q = q/L, \\ \omega_p &= 2\pi p/L, \quad \omega_q = 2\pi q/L. \end{aligned} \quad (1.9)$$

The forces are obtained as $f_i = -\nabla_{r_i} U_i$,

$$\begin{aligned} f_{x_{ij}}(x_{ij}, y_{ij}, z_{ij}) &= \frac{8\pi}{L^3} \sum_{p,q>0} p \frac{e^{-2\pi f_{pq}|z_{ij}|}}{f_{pq}} \sin(\omega_p x_{ij}) \cos(\omega_q y_{ij}) \\ &+ \frac{4\pi}{L^2} \sum_{p>0} e^{-2\pi f_p|z_{ij}|} \sin(\omega_p x_{ij}), \end{aligned}$$

$$\begin{aligned}
f_{y_{ij}}(x_{ij}, y_{ij}, z_{ij}) &= \frac{8\pi}{L^3} \sum_{p,q>0} q \frac{e^{-2\pi f_{pq}|z_{ij}|}}{f_{pq}} \sin(\omega_p x_{ij}) \cos(\omega_q y_{ij}) \\
&+ \frac{4\pi}{L^2} \sum_{q>0} e^{-2\pi f_q|z_{ij}|} \sin(\omega_q x_{ij}),
\end{aligned}$$

$$\begin{aligned}
f_{z_{ij}}(x_{ij}, y_{ij}, z_{ij}) &= \frac{8\pi \operatorname{sign}(z_{ij})}{L^2} \sum_{p,q>0} p \frac{e^{-2\pi f_{pq}|z_{ij}|}}{f_{pq}} \cos(\omega_p x_{ij}) \cos(\omega_q y_{ij}) \\
&+ \frac{4\pi \operatorname{sign}(z_{ij})}{L^2} \sum_{p>0} e^{-2\pi f_p|z_{ij}|} \cos(\omega_p x_{ij}) \\
&+ \frac{4\pi \operatorname{sign}(z_{ij})}{L^2} \sum_{q>0} e^{-2\pi f_q|z_{ij}|} \cos(\omega_q x_{ij}) \\
&+ \frac{2\pi \operatorname{sign}(z_{ij})}{L^2}.
\end{aligned}$$

The singularity in β in the far formula vanishes once the sum of ϕ_β is taken over all particles via the charge neutrality condition. Therefore such a formula is applicable only to charge neutral systems. The final sum converges well as the summands decay exponentially, but for small z_{ij} the convergence becomes poor and for $z_{ij} = 0$ the sum is not defined. Thus an alternative method is used for small z_{ij} (see below).

Transformation of $\tilde{\phi}_\beta$ for $z_{ij} \approx 0$ - the near formula

For small particle distances, the terms in eqn. 1.3 is split into two to efficiently sum over the area which has a hole due to the omission of the self energy term $k = l = 0$. Taking the limit $\beta \rightarrow 0$ for $|z_i - z_j| \leq L/2$ the near formula reads

$$\begin{aligned}
\tilde{\phi}(x_{ij}, y_{ij}, z_{ij}) &= \frac{4}{L} \sum_{p,l>0} (K_0(\omega_p \rho_l) + K_0(\omega_p \rho_{-l})) \cos(\omega_p x_{ij}) \\
&- \frac{2}{L} \sum_{n \geq 1} \frac{b_{2n}}{2n(2n)!} \operatorname{Re}((2\pi(z_{ij} + iy_{ij})/L)^{2n}) + \sum_{k=1}^{N_\psi-1} \left(\frac{1}{r_k} + \frac{1}{r_{-k}} \right) \\
&- \frac{1}{L} \sum_{n \geq 0} \binom{-1/2}{n} \frac{(\psi^{(2n)}(N_\psi + x_{ij}/L) + \psi^{(2n)}(N_\psi - x_{ij}/L))}{(2n)!} (\rho/L)^{2n} \\
&- \frac{2}{L} \log(4\pi), \tag{1.10}
\end{aligned}$$

where K_0 is called the modified Bessel function of order 0 [139], $\rho_l = \sqrt{(y_{ij} + (l/L))^2 + z_{ij}^2}$, $\rho = \rho_0$, b_n are the Bernoulli numbers, $\psi^{(n)}$ are polygamma functions and N_ψ such that $N_\psi >$

$(\rho/L) + 1$. The forces are obtained as $f_i = -\nabla_{r_i} U_i$,

$$f(x_{ij}, y_{ij}, z_{ij}) = \tilde{f}(x_{ij}, y_{ij}, z_{ij}) + \begin{cases} \frac{1}{(x_{ij}^2 + y_{ij}^2 + z_{ij}^2)^{3/2}} \begin{pmatrix} x_{ij} \\ y_{ij} \\ z_{ij} \end{pmatrix} & (x_{ij}, y_{ij}, z_{ij}) \neq (0, 0, 0), \\ 0 & (x_{ij}, y_{ij}, z_{ij}) = (0, 0, 0), \end{cases} \quad (1.11)$$

where

$$\begin{aligned} \tilde{f}_{x_{ij}}(x_{ij}, y_{ij}, z_{ij}) &= \frac{8\pi}{L^2} \sum_{p,l>0} p(K_0(\omega_p \rho_l) + K_0(\omega_p \rho_{-l})) \sin(\omega_p x_{ij}) \\ &+ \sum_{k=1}^{N_\psi-1} \left(\frac{x_{ij} + (k/L)}{r_k^3} + \frac{x_{ij} - (k/L)}{r_{-k}^3} \right) \\ &+ \frac{1}{L^2} \sum_{n \geq 0} \binom{-1/2}{n} \frac{(\psi^{(2n+1)}(N_\psi + (x_{ij}/L)) - \psi^{(2n+1)}(N_\psi - (x_{ij}/L)))}{(2n)!} (\rho/L)^{2n}, \end{aligned}$$

$$\begin{aligned} \tilde{f}_{y_{ij}}(x_{ij}, y_{ij}, z_{ij}) &= \frac{8\pi}{L^2} \sum_{p,l>0} p \left(\frac{(y_{ij} + (l/L))K_1(\omega_p \rho_l)}{\rho_l} + \frac{(y_{ij} - (l/L))K_1(\omega_p \rho_{-l})}{\rho_{-l}} \right) \cos(\omega_p x_{ij}) \\ &- \frac{4\pi}{L^2} \sum_{n \geq 1} \frac{b_{2n}}{(2n)!} \text{Im}((2\pi(z_{ij} + iy_{ij})/L)^{2n-1}) + \sum_{k=1}^{N_\psi-1} \left(\frac{y_{ij}}{r_k^3} + \frac{y_{ij}}{r_{-k}^3} \right) \\ &+ \frac{y_{ij}}{L^3} \sum_{n \geq 1} \binom{-1/2}{n} \frac{(\psi^{(2n)}(N_\psi + (x_{ij}/L)) + \psi^{(2n)}(N_\psi - (x_{ij}/L)))}{(2n-1)!} (\rho/L)^{2(n-1)}, \end{aligned}$$

$$\begin{aligned} \tilde{f}_{z_{ij}}(x_{ij}, y_{ij}, z_{ij}) &= \frac{8\pi}{L^2} \sum_{p,l>0} p \left(\frac{z_{ij}K_1(\omega_p \rho_l)}{\rho_l} + \frac{z_{ij}K_1(\omega_p \rho_{-l})}{\rho_{-l}} \right) \cos(\omega_p x_{ij}) \\ &+ \frac{4\pi}{L^2} \sum_{n \geq 1} \frac{b_{2n}}{(2n)!} \text{Re}((2\pi(z_{ij} + iy_{ij})/L)^{2n-1}) + \sum_{k=1}^{N_\psi-1} \left(\frac{z_{ij}}{r_k^3} + \frac{z_{ij}}{r_{-k}^3} \right) \\ &+ \frac{z_{ij}}{L^3} \sum_{n \geq 1} \binom{-1/2}{n} \frac{(\psi^{(2n)}(N_\psi + (x_{ij}/L)) + \psi^{(2n)}(N_\psi - (x_{ij}/L)))}{(2n-1)!} (\rho/L)^{2(n-1)}, \end{aligned}$$

where K_1 is the modified Bessel function of order one. However, this sum also leads to the same singularity in β as far formula and the charge neutrality argument also holds for any combination of the two formulas as long as the sum is performed over all particles.

Computation time

The far and near formulas can be efficiently implemented to achieve the time scaling of $\mathcal{O}(N^{5/3} \log(N)^2)$ [145]. The method is to split the simulation box into B equally sized slices along the z -axis. For all particles in slice S the interaction with the particles in the slices $S - 1$, S and $S + 1$ (if existent) is calculated using the near formula. For the other slices the far formula is used. However, for the near formula to be valid, $|z_i - z_j| \leq L/2$ for particles i and j located in adjacent slices. This gives the constraint

$$\frac{2L_z}{B} \leq \frac{L}{2}, \quad (1.12)$$

where L_z is the simulation box height. Therefore one could tune the parameter B (normally chosen large enough) to yield a minimal computation time. The above particle sorting procedure can be done in time $\mathcal{O}(N)$ [145]. The time for calculation of the near sum can be obtained as $\mathcal{O}(N(2N/B))$. The calculation of the far formula consists of summing terms in the Fourier space. An efficient implementation of this sum can lead to a computational time of the order $\mathcal{O}(R^2N) + \mathcal{O}(R^2B^2)$ for homogeneously distributed particles in the system [145], where R is the cutoff used in the far formula. Choosing the minimal distance of two particles that are treated by the far formula as L_z/B , finally the asymptotic scaling $\mathcal{O}(N^{5/3} \log(N)^2)$ is reached.

List of symbols

a	distance between charged subunits on a chain
a_i	activity coefficient of species i
b	bond length or monomer size
b_k	Kuhn segment length
c_{ci}	counterion concentration
c_m	monomer concentration
c_p	polymer concentration
c_s	salt concentration in solution
c'_s	salt concentration in solution outside the brush (buffer salt)
c'_{si}	concentration of small ions (chain counterions and salt ions) outside the brush
c''_{si}	concentration of small ions inside the brush
$C_X(t)$	autocorrelation function
D	distance between two planar parallel surfaces grafted with charged chains
e	electron charge
\mathbf{f}	force
f	fractional charge of the chain $0 \leq f \leq 1$
F	free energy
h	brush height
H	counterion layer thickness
k	spring constant
$k_B T$	thermal energy
L	simulation box height in x or y -direction
L_e	electrostatic persistence length of the chain
L_i	intrinsic persistence length of the chain
L_p	persistence length of the chain
L_z	simulation box height in z -direction
m	mass
M	number of polymer chains
N	number of monomers in a chain
N_{tot}	total number of (charged) particles

$P(r)$	ion-polyelectrolyte distribution function
q_i	charge on particle i in units of elementary charge e
\mathbf{q}	wave vector
$\{\mathbf{r}_i\}$	set of bond vectors
r_s	shape factor
$\{\mathbf{R}_i\}$	set of position vectors
\mathbf{R}	end-to-end vector
R	root mean square end-to-end distance
R_g	radius of gyration
\mathbf{R}_{CM}	center of mass of the chain
R_{max}	maximum length of the end-to-end vector (contour length)
s_{ineff}	statistical inefficiency
S	entropy
$S(q)$	spherically averaged structure factor of a single chain
$S(q_{xy})$	in-plane averaged structure factor of a single chain
$S(q_z)$	structure factor of a single chain perpendicular to the grafting plane
δt	time step
$u(r)$	interaction potential as a function of separation r
U	potential energy
v	excluded volume
v_e	electrostatic excluded volume
v_2	second virial coefficient
w	third virial coefficient
\mathbf{W}_i	Gaussian random force on particle i
$W(\mathbf{R})$	number of chain conformations with end-to-end vector \mathbf{R} for fixed N
Y	Young's modulus
$\langle z_{\text{ci}} \rangle$	average counterion height
$\langle z_e \rangle$	average brush end point height
$\langle z_m \rangle$	average brush mid-height
α	splitting parameter in the Ewald sum
ϵ	Lennard-Jones energy
ε	dielectric constant of solvent
ε_0	vacuum permittivity
Γ	friction constant
λ_B	Bjerrum length ($e^2/4\pi\varepsilon_0\varepsilon k_B T$)
$\lambda_D = \kappa^{-1}$	Debye length
λ_{GC}	Gouy-Chapman length
μ_i	chemical potential of species i

ν	exponent of N dependence of chain radius R ($R \sim N^\nu$)
Ω	partition function
π	pressure
$\phi(\mathbf{r})$	potential at point \mathbf{r}
φ	probability distribution
$\Psi(\{\mathbf{r}_i\})$	conformational distribution of chain
$\psi(\mathbf{r}_i, \dots, \mathbf{r}_{i+i_c})$	bond distribution
ρ_a	anchoring density of polymer chains
$\rho_e(z)$	endpoint distribution as a function of distance z from anchoring surface
$\rho_{ci}(z)$	counterion density profile as a function of distance z from anchoring surface
$\rho_m(z)$	monomer density profile as a function of distance z from anchoring surface
σ	Lennard-Jones length
σ_{eff}	effective monomer hard-core diameter
τ	linear charge density
τ_{LJ}	Lennard-Jones time
τ_m	relaxation time for average brush thickness
τ_{run}	number of measurements
ξ	blob size

Bibliography

- [1] Dautzenberg, H.; Jaeger, W.; Kötz, J.; Philipp, B.; Seidel, C.; Stscherbina, D. *Polyelectrolytes: Formation, Characterization and Application*; Hanser Publishers: Munich, Vienna, New York, 1994.
- [2] de Gennes, P. G. *Scaling concepts in Polymer Physics*; Cornell University Press, Ithaca, 1979.
- [3] Stevens, M. J.; Kremer, K. *J. Chem. Phys.* **1995**, *103*, 1669-1690.
- [4] Holm, C.; Joanny J. F.; Kremer, K.; Netz R. R.; Reineker P.; Seidel, C.; Vilgis T. A.; Winkler R.G. *Adv. Polym. Sci.* **2004**, *166*, 67-111.
- [5] Halperin, A.; Tirrell, M.; Lodge, T. P. *Adv. Polym. Sci.* **1991**, *100*, 31-71.
- [6] Israëls, R.; Leermakers, F. A. M.; Fleer, G. J. *Macromolecules* **1994**, *27*, 3087-3093.
- [7] Lyatskaya, Y. V.; Leermakers, F. A. M.; Fleer, G. J.; Zhulina, E. B.; Birshstein, T. M. *Macromolecules* **1995**, *28*, 3562.
- [8] Alexander, S. *J. Phys.* **1977**, *28*, 977.
- [9] Pincus, P. *Macromolecules* **1991**, *24*, 2912-2919.
- [10] Ahrens, H; Förster, S; Helm, C.A.; Kumar, N.A; Naji, A; Netz, R.R.; Seidel, C. *J. Phys. Chem. B* **2004**, *108*, 16870-16876.
- [11] Flory, P.J. *Principles of Polymer Chemistry*; Cornell University Press, Ithaca, 1953.
- [12] Flory, P.J. *Statistical Mechanics of Chain Molecules*; Interscience Publishers, New York, 1969.
- [13] Yamakawa, H. *Modern Theory of Polymer Solutions*; Harper & Row, New York, 1971.
- [14] Doi, M.; Edwards, S. F. *The Theory of Polymer Dynamics*; Clarendon Press, Oxford, 1986.

- [15] Freed, K. F. *Renormalization Group Theory of Macromolecules*; John Wiley & Sons, New York 1987.
- [16] Grosberg, A. Y.; Khokhlov, A. R. *Statistical Physics of Macromolecules*; AIP Press, New York 1994.
- [17] Berne, B. J.; Pecora R. *Dynamic Light Scattering*; Wiley, Newyork, 1976.
- [18] Marshall, W.; Lovesey, S. W. *Theory of Thermal Neutron Scattering*; Oxford Univ. Press, 1971.
- [19] Rhe, J.; Ballauff, M.; Biesalski, M.; Dziezok, P.; Grhn, F.; Johannsmann, D.; Houbenov, N.; Hugenberg, N.; Konradi, R.; Minko, S.; Motornov, M; Netz, R. R.; Schmidt, M.; Seidel, C.; Stamm, M.; Stephan, T.; Usov, D.; Zhang, H. *Adv. Polym. Sci.* **2004**, *165*, 79-150.
- [20] Kratky, O.; Porod, G. *Rec. Trav. Chim.* **1949**, *68*, 1106.
- [21] Raphael, E.; Joanny, J. F. *Europhys. Lett.* **1990**, *13*, 623.
- [22] Ewald, P. P. *Ann. Phy.* **1920**, *64*, 253.
- [23] Debye, P.; Hckel E. *Phys. Z.* **1923**, *24*, 185.
- [24] Valleau, J. P. *Chem. Phys.* **1989**, *129*, 163.
- [25] Bret, L. M.; Zimm, B. H. *Biopolymers* **1984**, *23*, 271.
- [26] Fuoss, R. M.; Katachalsky, A.; Lifson, S. *Proc. Natl. Acad. Sci. U.S.A.* **1951**, *37*, 579.
- [27] Odijk, T. *J. Polym. Sci., Polym. Phys. Ed.* **1977**, *15*, 477.
- [28] Skolnick, J.; Fixman, M. *Macromolecules* **1977**, *10*, 944.
- [29] Odijk, T.; Houwaart, A. *J. Polym. Sci.* **1978**, *16*, 627.
- [30] Barrat, J.-L.; Joanny, J.-F. *Europhys. Lett.* *3*, *343* (1993). **1993**, *3*, 343.
- [31] de Gennes, P. G.; Pincus, P.; Velasco, R. M.; Brochard, F. *J. Phys. Paris* **1976** *37*, 1461.
- [32] Manning, G. *J. Chem. Phys.* **1969**, *51*, 924.
- [33] Manning, G. *J. Chem. Phys.* **1969**, *51*, 934.
- [34] Manning, G. *Q. Rev. Biophys.* **1978**, *11*, 179.
- [35] Anderson, C. F.; Record, M. T. *Annu. Rev. Phys. Chem.* **1982**, *33*, 191.
- [36] Fixman, M. *J Chem Phys* **1982**, *76*, 6346.

- [37] Le Bret, M. *J Chem Phys* **1982**, *76*, 6243.
- [38] Manning, G. S.; Mohanty, U. *Physica A* **1997**, *247*, 196.
- [39] Manning, G. S. *J Chem Phys* **1988** *89*, 3772.
- [40] Wandrey, C.; Hunkeler, D.; Wendler, U.; Jaeger, W. *Macromolecules* **2000** *33*, 7136.
- [41] Blaul, J.; Wittemann, M.; Ballau, M.; Rehahn, M. *J Phys Chem B* **2000**, *104*, 7077.
- [42] Oosawa, F. *Polyelectrolytes*; Marcel Dekker, New York, 1971.
- [43] Schiessel, H. *Macromolecules* **1999**, *32*, 5673.
- [44] Khokhlov, A. R.; Khachaturian, K. A. *Polymer* **1982**, *13*, 1742.
- [45] Netz, R.R.; Orland, H. *Eur. Phys. J. B.* **1999**, *8*, 81.
- [46] Everaers, R.; Milchev, A.; Yamakov, V. *Eur. Phys. J. E.* **2002**, *8*, 3.
- [47] Khokhlov, A. *J. Phys. A* **1980**, *13*, 979.
- [48] Tirtaatmadja, V.; Tam, K. C.; Jenkins, R. D. *Macromolecules* **1997**, *30*, 3271.
- [49] Uyaver, S.; Seidel C. *Europhys. Lett.* **2003**, *64*, 536.
- [50] Overney, R. M.; Leta, D. P.; Pictroski, C. F.; Rafailovich, M.; Liu, Y.; Quinn, J.; Sokolov, J.; Eisenberg, A.; Overney, G. *Phys. Rev. Lett.* **1966**, *76*, 1272.
- [51] Netz, R. R.; Andelman, D. *Phys. Rep.* **2003**, *380*, 1-95.
- [52] Napper, D. H. *Polymeric Stabilization of Colloidal Dispersions*; Academic Press, New York, 1983.
- [53] Fleer, G. J.; Stuart M. A. C.; Scheutjens, J. M. H. M.; Cosgrove, T.; Vincent, B. *Polymers at Interfaces*; Chapman and Hall, London, 1993.
- [54] de Gennes, P. G. *J. Phys. (France)* **1976**, *37*, 1445.
- [55] de Gennes, P. G. *Macromolecules* **1980**, *13*, 1069.
- [56] Milner, S. T.; Witten, T. A.; Cates, M. E. *Macromolecules* **1988**, *21*, 2610.
- [57] Skvortsov, A. M.; Gorbunov, A. A.; Pavlushkov, V. A.; Zhulina, E. B.; Borisov, O. V.; Priamitsyn, V. A. *Polym. Sci. USSR* **1988**, *30*, 1706.
- [58] Milner, S. T. *Science* **1991**, *251*, 905.
- [59] Halperin, A. *Macromol Rep* **1992**, *A29*, 107.

- [60] Netz, R.R.; Schick, M. *Macromolecules* **1998**, *31*, 5105.
- [61] Lipowsky R.; Sackmann, E. (Editors) *The Structure and Dynamics of Membranes*, in *Handbook of Biological Physics*, Vol. 1, Elsevier, Amsterdam, 1995.
- [62] Lipowsky, R. *Europhys. Lett.*, **1995**, *30*, 197-202.
- [63] Semenov, A. N. *Sov. Phys. JETP*, **1985**, *61*, 733.
- [64] Cosgrove, T.; Heath, T.; van Lent, B.; Leermakers, F.; Scheutjens, J. *Macromolecules* **1987**, *20*, 1692.
- [65] Orland, H.; Schick, M. *Macromolecules* **1996**, *29*, 713.
- [66] Grest, G. S.; Murat, M. in Reference [141].
- [67] Seidel, C.; Netz, R. *Macromolecules* **2000**, *33*, 634-640.
- [68] Taunton, H. J.; Toprakcioglu, C.; Fetters L. J.; Klein, J. *Nature* **1988**, *332*, 712.
- [69] Auroy, P.; Auvray L.; Leger, L. *Phys. Rev. Lett.* **1991**, *66*, 719.
- [70] Field, J.B., P.; Toprakcioglu, C.; Dai, L.; Hadziioannou, G.; Smith, G.; Hamilton, W. *J. Phys. II France* **1992**, *2*, 2221.
- [71] Bijsterbosch, H.D.; de Haan, V. O.; de Graaf, A. W.; Mellema, M.; Leermakers, F. A. M.; Cohen Stuart, M. A.; van Well, A. A. *Langmuir* **1995**, *11*, 4467.
- [72] Factor, B. J.; Lee, L.-T.; Kent, M. S.; Rondelez, F. *Phys. Rev. E* **1993**, *48*, R2354.
- [73] Bianco-Peled, H.; Dori, Y.; Schneider, J.; Tirrell, M. *Langmuir*, **2001**, *17*, 6931.
- [74] Mayes, A. M.; Kumar, S. K. *MRS Bull.* **1997**, *22*, 43.
- [75] Ito, Y.; Nishi, S.; Park, Y. S.; Imanishi, Y. *Macromolecules* **1997**, *30*, 5856.
- [76] de Gennes, P. G. *C. R. Acad. Sci. Paris* **1985**, *300*, 839.
- [77] Murat, M.; Grest, G. S. *Phys. Rev. Lett.* **1989**, *63*, 1074-1077.
- [78] Hadziioannou, G.; Patel, S. Granick, S.; Tirrel, M. *J. Am. Chem. Soc.* **1986**, *108*, 2869.
- [79] Taunton, H. J.; Toprakcioglu, C.; Fetters L. J.; Klein, J. *Macromolecules* **1990**, *23*, 571.
- [80] Patel, S. S.; Tirrell, M.; *Annu. Rev. Phys. Chem.* **1989**, *40*, 597.
- [81] Muthukumar, M.; Ho, J. -S. *Macromolecules* **1989**, *22*, 965.
- [82] Israelachvili, J. *Intermolecular and Surface forces*; Academic Press, London, 1992.

- [83] Murat, M.; Grest, G. S. *Macromolecules* **1996**, *29*, 8282-8284.
- [84] Grest, G. S., *Adv. Polym. Sci.* **1999**, *138*, 149.
- [85] Miklavic, S. J.; Marčelja, S. *J. Phys. Chem.* **1988**, *92*, 6718-6722.
- [86] Misra, S.; Varanasi, S.; Varanasi, P. P. *Macromolecules* **1989**, *22*, 4173-4179.
- [87] Borisov, O. V.; Birshtein, T. M.; Zhulina, E. B. *J. Phys. II (Paris)* **1991**, *1*, 521-526.
- [88] Ross, R. S.; Pincus, P. *Macromolecules* **1992**, *25*, 2177-2183.
- [89] Wittmer, J.; Joanny, J. F. *Macromolecules* **1993**, *26*, 2691-2697.
- [90] Amoskov, V. M.; Pryamitsyn, V. A. *J. Chem. Soc. Faraday Trans.* **1994**, *90*, 889-893.
- [91] von Goeler, F.; Muthukumar, M. *Macromolecules* **1995**, *28*, 6608-6617.
- [92] Zhulina, E. B.; Borisov, O. V. *J. Chem. Phys.* **1997**, *107*, 5952-5967.
- [93] Csajka, F. S.; Netz, R. R.; Seidel, C.; Joanny, J.-F. *Eur. Phys. J. E* **2001**, *4*, 505-513.
- [94] Naji, A.; Netz, R. R.; Seidel, C. *Eur. Phys. J. E* **2003**, *12*, 223-237.
- [95] Zhulina, E. B.; Borisov, O. V.; Birshtein T. M. *J. Phys. II (Paris)* **1992**, *2*, 63-74.
- [96] Israëls, R.; Leermakers, F. A. M.; Fleer, G. J.; Zhulina, E. B. *Macromolecules* **1994**, *27*, 3249-3261.
- [97] Borisov, O. V.; Zhulina, E. B.; Birshtein, T. M. *Macromolecules* **1994**, *27*, 4795-4803.
- [98] Zhulina, E. B.; Wolterink, J. K.; Borisov, O. V. *Macromolecules* **2000**, *33*, 4945-4953.
- [99] Argillier, J. -F.; Tirrell, M. *Theor. Chim. Acta* **1992**, *82*, 343-350.
- [100] Granfeldt, M. K.; Miklavic, S. J.; Marčelja, S.; Woodward, C. E. *Macromolecules* **1990**, *23*, 4760-4768.
- [101] Sjöström, L.; Åkesson, T.; Jönsson, B. J. *J. Chem. Phys.* **1993**, *99*, 4739-4747.
- [102] Chen, H.; Zajac, R.; Chakrabarti, A. *J. Chem. Phys.* **1996**, *104*, 1579-1588.
- [103] Csajka, F. S.; van der Linden, C. C.; Seidel, C. *Macromol. Symp.* **1999**, *146*, 243-249.
- [104] Csajka, F. S.; Seidel, C. *Macromolecules* **2000**, *33*, 2728-2739.
- [105] Seidel, C. *Macromolecules* **2003**, *36*, 2536-2543.
- [106] Kumar, N.A.; Seidel, C. *Macromolecules* **2005**, *38*, 9341.

- [107] Watanabe, H.; Patel, S. S.; Argillier, J. F.; Parsonnage, E. E.; Mays, J. W.; Dan-Brandon, N.; Tirrell, M.; *Mater. Res. Soc. Symp. Proc.* **1992**, *249*, 255-265.
- [108] Amiel, C.; Sikka, M.; Schneider, J. W.; Tsao, Y. H.; Tirrell, M.; Mays, J. W. *Macromolecules* **1995**, *28*, 3125-3134.
- [109] Ahrens, H.; Förster, S.; Helm, C. A. *Macromolecules* **1997**, *30*, 8447-8452.
- [110] Biesalski, M.; Rühle, J.; Johannsmann, D. *J. Chem. Phys.* **1999**, *111*, 7029-7037.
- [111] Tran, Y.; Auroy, P. *Eur. Phys. J. E* **2001**, *5*, 65-79.
- [112] Muller, F.; Fontaine, P.; Delsanti, M.; Belloni, L.; Yang, J.; Chen, Y. J.; Mays, J. W.; Lesieur, P.; Tirrell, M.; Guenoun, P. *Eur. Phys. J. E* **2001**, *6*, 109-115.
- [113] Guenoun, P.; Schlachli, A.; Sentenac, D.; Mays, J. W.; Benattar, J. J. *Phys. Rev. Lett.* **1995**, *74*, 3628-3631.
- [114] Mir, Y.; Auroy, P.; Auvray, L. *Phys. Rev. Lett.* **1995**, *75*, 2863-2866.
- [115] Ahrens, H.; Förster, S.; Helm, C. A. *Phys. Rev. Lett.* **1998**, *81*, 4172-4175.
- [116] Hariharan, R.; Biver, C.; Mays, J.; Russel, W. B. *Macromolecules* **1998**, *31*, 7506-7513.
- [117] Hariharan, R.; Biver, C.; Russel, W. B. *Macromolecules* **1998**, *31*, 7514-7518.
- [118] Tran, Y.; Auroy, P.; Lee, L.-T. *Macromolecules* **1999**, *32*, 8952-8964.
- [119] Balastre, M.; Li, F.; Schorr, P.; Yang, J.; Mays, J.W.; Tirrell, M. V. *Macromolecules* **2002**, *35*, 9480-9486.
- [120] Kaewsaiha, P.; Matsumoto, K.; Matsuoka, H. *Langmuir* **2004**, *20*, 6754-6761.
- [121] Romet-Lemonne, G.; Daillant, J.; Guenoun, P.; Yang, J.; Mays, J. W. *Phys. Rev. Lett.* **2004**, *93*, 148301.
- [122] Hayashi, S.; Abe, T.; Higashi, N.; Niwa, M.; Kurihara, K. *Langmuir* **2002**, *18*, 3932.
- [123] Raviv, U.; Giasson, S.; Kampf, N.; Gohy, J. -F.; Jerome, R.; Klein, J. *Nature (London)* **2003** *425*, 163.
- [124] Pavor, P. V.; Gearing, B. P.; Bellare, A.; Cohen, R. E. *Wear* **2004**, *256*, 1196.
- [125] Hummer, G.; Grønbech-Jensen, N.; Neumann, M. *J. Chem. Phys.* **1998**, *109*, 2791.
- [126] Ito, Y.; Park Y. S.; Imanishi, Y. *Langmuir* **2000**, *16*, 5376-5381.

- [127] Husemann, M.; Morrison, M.; Benoit, D.; Frommer, J.; Mate, C. M.; Hinsberg, W. D.; Hedrick, J. L.; Hawker, C. J. *J Am. Chem. Soc.* **2000**, *122*, 1844.
- [128] Stevens, M. J.; Plimpton, S. J. *Eur. Phys. J. B* **1998**, *2*, 341-345.
- [129] Crozier, P.S.; Stevens, M. J. *J. Chem. Phys.* **2003** *118*, 3855.
- [130] Hehmeyer, O.J.; Stevens, M. J. *J. Chem. Phys.* **2005** *122*, 134909.
- [131] Kreer, T.; Müser, M. H.; Binder, K.; Klein, J. *Langmuir* **2001**, *17*, 7804-7813.
- [132] Pryamitsyn, V. A.; Leermakers, F. A. M.; Fleer, G. J.; Zhulina, E. B. *Macromolecules* **1995**, *29*, 8260.
- [133] Carnie, S. L.; Christos, G. A. *J. chem. Phys.* **1989**, *89*, 6484.
- [134] Christos, G. A.; Carnie, S. L. *J. chem. Phys.* **1989**, *91*, 439.
- [135] Christos, G. A.; Carnie, S. L. *J. chem. Phys.* **1990**, *92*, 7661.
- [136] Rouse, P. E. *J. chem. Phys.* **1953**, *21*, 1273.
- [137] Zimm, B. E. *J. chem. Phys.* **1956**, *24*, 265.
- [138] J. Kolafa, J.; Perram, J. W. *Molecular Simulation* **1992**, *5*, 351.
- [139] Abramowitz, M.; Stegun, I. *Handbook of Mathematical Functions*; Dover Publications, New York, 1972.
- [140] Allen, M. P.; Tildesley, D. J. (editors) *Computer Simulation in Chemical Physics*; Kluwer Academic Publishers, Dordrecht, 1993.
- [141] Binder, K. (editor) *Monte Carlo and Molecular Dynamics Simulations in Polymer Science*; Oxford University Press, New York, 1995.
- [142] Dünweg, B.; Stevens, M. J.; Kremer, K. in Reference [141], pages 125-193 (chapter 3).
- [143] Tildesley, D. J. in Reference [140], pages 23-47.
- [144] Strebel, R.; Sperb, R. *Mol. Simul.* **2001**, *27*, 61-74.
- [145] Arnold, A.; Holm, C. *Comput. Phys. Commun.* **2002**, *148*, 327-348.
- [146] Lekner, J. *Physica A* **1991**, *176*, 485-498.
- [147] Sperb, R. *Mol. Simul.* **1994**, *13*, 189-193.
- [148] Sperb, R. *Mol. Simul.* **1998**, *20*, 179-200.

- [149] Widmann A. H.; Adolf, D. B. *Comp. Phys. Commun.* **1997**, *107*, 167-186.
- [150] Joannis, J. de; Arnold, A.; Holm, C. *J. Chem. Phys.* **2002**, *117*, 2503.
- [151] Pollock, E. L.; Glosli, J. *Comput. Phys. Commun.* **1996**, *95*, 93.
- [152] Grest, G. S.; Kremer, K. *Phys. Rev. A* **1986**, *33*, 3628-3631.
- [153] Kremer, K.; Grest, G. S. *J. Chem. Phys.* **1990**, *92*, 5057.
- [154] Dünweg, B.; Paul, W. *Int. J. Mod. Phys.* **1991**, *2*, 817.
- [155] Kremer, K.; Grest, G. S. *J. Chem. Soc. Faraday trans.* **1992**, *88*, 1707.
- [156] Allen, M. P.; Tildesley, D. J. *Computer Simulation of Liquids*; Oxford University Press, Oxford, 1987.
- [157] Gropp, W.; Lusk, E.; Skjellum, A. *Using MPI*; The MIT Press, Cambridge Massachusetts, 1994.
- [158] Chandler, D. *Introduction to Modern Statistical Mechanics*; Oxford University Press, New York, 1987.
- [159] Humphrey, W.; Dalke, A.; Schulten, K. *J. Molec. Graphics* **1996**, *14.1*, 33-38.
- [160] Donnan, F. G. *Z. Elektrochem.* **1911**, *17*, 572.
- [161] Tanford, C. *Physical Chemistry of Macromolecules*; John Wiley & Sons, New York, 1961.
- [162] Deserno, M. *Ph. D. Thesis*; Johannes Gutenberg-Universität, Mainz, 2000.
- [163] Moreira, A.G.; Netz, R.R. *Eur. Phys. J. E.* **2002**, *8*, 33.
- [164] Landau, L. D.; Lifshitz, E. M. *A Course of Theoretical Physics*; Pergamon Press, Oxford, 1980; Vol. 5, p 94.

Acknowledgments

I am grateful to Prof. Reinhard Lipowsky for giving me the opportunity to do my Ph.D. here at the Max Planck Institute of Colloids and Interfaces, Golm. I thank Dr. Christian Seidel for the motivation and support he gave me along the way. His inspiring supervision meant a lot to me.

The environment in the institute is very friendly and fruitful. I mention my personal gratitude to all members of the theory department. In addition, I would like to recognize IMPRS (International Max Planck Research School on Biomimetic Systems) for the financial support during my stay here, and Axel Arnold for helpful comments on his MMM2D code.

Thanks are also due to my friends: Gireesh, Gopan, Gopakumar, Sreeraj, Jestin, Abey, Imroz, Rajkumar, Mishra, Lakshman, Raveendra, and Padmanabhan.

For the past three years I found myself immersed in another culture. My family always supported me during these years. I am thankful for their love and support.